The physics of compact objects and experimental improvements on detectors in the gravitational-wave era

by

Hang Yu

B.S., Physics, Johns Hopkins University (2014)

Submitted to the Department of Physics
in partial fulfillment of the requirements for the degree of

Doctor of Philosophy

at the

MASSACHUSETTS INSTITUTE OF TECHNOLOGY

June 2019

Author . . . .
Department of Physics
February 20, 2019

Certified by. . . . .
Nevin N. Weinberg
Associate Professor
Thesis Supervisor

Certified by. . . . .
Matthew J. Evans
Associate Professor
Thesis Supervisor

Accepted by . . . .
Nergis Mavalvala
Chairman, Associate Department Head

The physics of compact objects and experimental improvements on detectors in the gravitational-wave era

by

Hang Yu

Submitted to the Department of Physics
on February 20, 2019, in partial fulfillment of the
requirements for the degree of
Doctor of Philosophy

Abstract

In this thesis, I designed and implemented a compiler which performs optimizations that reduce the number of low-level floating point operations necessary for a specific task; this involves the optimization of chains of floating point operations as well as the implementation of a "fixed" point data type that allows some floating point operations to simulated with integer arithmetic. The source language of the compiler is a subset of C, and the destination language is assembly language for a micro-floating point CPU. An instruction-level simulator of the CPU was written to allow testing of the code. A series of test pieces of codes was compiled, both with and without optimization, to determine how effective these optimizations were.

Thesis Supervisor: Nevin N. Weinberg
Title: Associate Professor

Thesis Supervisor: Matthew J. Evans
Title: Associate Professor

Acknowledgments

This is the acknowledgements section. You should replace this with your own acknowledgements.

Contents

---

[1]This Chapter is based-on [1].

List of Figures

11

List of Tables

Chapter 1

Overview of the Advanced LIGO (aLIGO) Detectors

In this chapter we review the Advanced LIGO (aLIGO) interferometer's optical topology and provide analytical derivations of the optical fields. Here we focus on a one-dimensional interferometer where all the optical components are perfectly aligned and mode-matched. The effects of higher-order spatial modes will be examined in details in the following chapter which will build upon the results derived here.

Before going into details, it would be helpful to distinguish three different frequency scales. The first one is the laser oscillation frequency, $\nu_0 = \omega_0/2\pi = c/\lambda \simeq 3 \times 10^{14}$ Hz, where $\lambda = 1.064$ nm is the laser wavelength used by aLIGO. This frequency determines the energy carried per photon being $\hbar\omega_0$. The second scale corresponds to the radio frequency (RF) of a few to a few hundred MHz. For aLIGO, it utilizes multiple RF sidebands to keep the resonant condition of the interferometer via the Pound-Drever-Hall technique. Lastly, the frequency band we are mostly interested in lies in the audio band ranging from a few Hz to a few kHz. This is the frequency band where the GW signals from merging stellar-mass black-hole (BH) or NS binaries lies above aLIGO's noise background. As a result, this frequency range is also known as the signal sideband.

Through out this chapter and the following one, we adopt the following conventions. We denote an optical field as E whose dimension is set so that $[E^2] = $ Power.

To model the transmission and reflection at a dielectric boundary, we let the optical field pick up a phase shift of $\pi/2$ for every transmission through a surface, whereas it experiences no extra phase change upon reflection. Note that with convention any optical component considered will have two surfaces. As for field propagations, we assume that the free space is always an integer multiple of the laser wavelength λ, while the residual tuning is then assigned to mirrors as one of their parameters. Those are the same conventions used in numerical simulation tool `FINESSE` [2] which we will use frequently to numerically verify our analytical results.

1.1 Topology of aLIGO

We present the optical layout of the aLIGO interferometer in Figure 1-1. It is known as a "dual-recycled Fabry-Perot Michelson interferometer", which can be understood as the following. The central beamsplitter (BS) and the two end test masses (ETMs; we will further refer the ETM whose surface normal vector is parallel to the input beam as ETMX, and the one whose normal vector is orthogonal to the input beam as ETMY) form a Michelson interferometer which allows differential motions between the ETMs (e.g. the motion generated by a passing-by GW) to be detected at the output, or the anti-symmetric port. On the other hand, common-mode signals such as the frequency fluctuations of the laser, will be reflected to the input, or the symmetric port. To enhance the sensitivity to the displacement, two input test masses (ITMs) are placed in between the BS and the ETMs. The ITM and the ETM thus forms a Fabry-Perot cavity (also known as the arm cavity) which not only increased the number of photons sampling the test masses' displacement at a given instant, but also traps a given photon inside the cavity to bounce upon the test masses multiple times and repeatedly performing the displacement measurement. To further enhance the number of photons measuring the length and consequently reducing the statistical uncertainty, a power-recycling mirror (PRM) is placed at the input port, which sends the beam returning from the BS to the input port back to the arm cavities to further increase the power circulating in the arms. Lastly, a signal-recycling mirror (SRM)
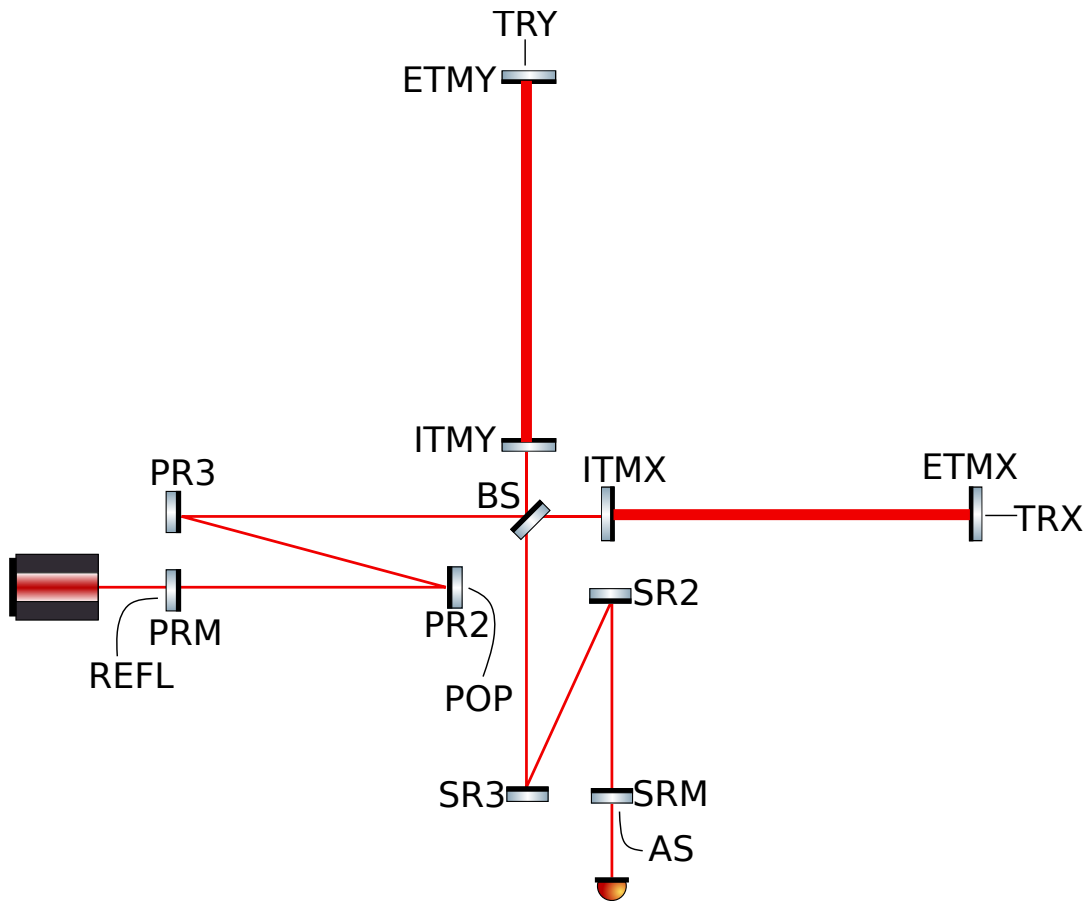
Figure 1-1: The optical layout of the aLIGO interferometer with the name of each optic labeled next to it. Although we will often treat the recycling cavities as linear cavities, in practice they are folded cavities each with three recycling mirrors. In the drawing we also labeled the locations of major readout ports which we will discuss in more details in Section 2.4.

Table 1.1: Parameters of the aLIGO optics in the third observing run.

Symbol	Definition	Value
T_i	ITM power transmissivity	1.4%
Γ_i	Round-trip losses of the arm cavity	~ 70 ppm
T_p	PRM power transmissivity	3.1%
T_s	SRM power transmissivity	32.5%

is placed at the output (anti-symmetric) port to form a signal recycling cavity with the ITMs. If a photon is trapped inside the arm cavity for a time longer than the oscillation period of a GW signal, the sensitivity to such a high-frequency signal will be reduced. The purpose of signal recycling is to modify the effective ITM reflectivity seen by the signal photons and alter its storage time in the arm cavity. This further allows the tradeoff between the instrument's peak sensitivity and its bandwidth.

In the following sections we will explore the above descriptions in more quantitative details. For the key parameters, they are defined in Table 1.1 with numerical value provided. Throughout this chapter, we will use T (R) to denote the power transmissivity (reflectivity) and $t = \sqrt{T}$ ($r = \sqrt{R}$) to denote the amplitude transmissivity (reflectivity). When denoting the properties of a physical mirror (i.e. the ITMs, PRM, and SRM), we keep t and r to be real and positive. However, when considering the effective transmissivity or reflectivity of a cavity, we allow t and r to be complex in general. To keep the analytical expressions trackable, we make the following simplifications. The main BS is assumed to be a perfect $50 - 50$ BS, and we assume the ETMs are perfectly reflecting with power reflectivity of 1. The arm cavity losses is then attribute to the ITMs. Power conservation thus leads to $T_\mathrm{i} + R_\mathrm{i} + \Gamma_\mathrm{i} = 1$. On the other hand, we ignore the losses in the recycling cavities and therefore $T_\mathrm{p\,(s)} + R_\mathrm{p\,(s)} = 1$. Note that in our phase convention, each mirror needs to be modeled with two surfaces to preserve energy. Therefore we attribute all the reflectivity to the highly reflective (HR) surface of each mirror, while treating all the anti-reflective (AR) surfaces with a transmissivity of 1.

1.2 Propagation of the DC fields

In this section we derive the propagation equations of the "DC" fields. Here by "DC" we mean that the systems is free from perturbations at audio frequencies. In other words, we will consider here how the carrier field and the RF sidebands propagate through the interferometer, with all the optics held perfectly static. To proceed, we will break the "dual-recycled Fabry-Perot Michelson interferometer" into individual components, and gradually compound them together to derive the full interferometer's response. In the process, we will label the fields that has significant meanings with Roman letters. On the other hand, for fields whose subscripts are numbers, they are only defined for the convenience of the derivation, and we will recycle their indices when study different components of the interferometer. Consequently, the E_1 field defined when we study the propagation in the arm cavity will in general differ from the E_1 field used to study the Michelson component. As a contrary, we will always use E_a to denote the field inside the arm cavity throughout this section.

1.2.1 The carrier field

To study the carrier field, we start by considering the arm cavity. In the steady state, we have the following input-output relation:

$$E_\mathrm{arm} = -t_\mathrm{i} E_1 + r_\mathrm{i} E'_\mathrm{arm}, \tag{1.1a}$$

$$E'_\mathrm{arm} = E_\mathrm{arm} e^{2\mathrm{i}\Delta\phi}, \tag{1.1b}$$

$$E'_1 = -r_\mathrm{i} E_1 - t_\mathrm{i} E'_\mathrm{arm}, \tag{1.1c}$$

where $\Delta\phi$ is the detuning of the ETM, and in writing the equation we have assumed the ETM is perfectly reflecting. The above set of equations can be solved in terms of the input field E_1, leading to

$$\frac{E_\mathrm{arm}}{E_1} = \frac{-t_\mathrm{i}}{1 - r_\mathrm{i} e^{2\mathrm{i}\Delta\phi}}, \tag{1.2a}$$

$$\frac{E'_1}{E_1} = \frac{-r_\mathrm{i} + (r_\mathrm{i}^2 + t_\mathrm{i}^2) e^{2\mathrm{i}\Delta\phi}}{1 - r_\mathrm{i} e^{2\mathrm{i}\Delta\phi}}. \tag{1.2b}$$

In the limit where detuning $\Delta\phi \ll 1$ and $\Gamma_i \ll T_i \ll 1$, we can expand $e^{2i\Delta\phi} \simeq 1+2i\Delta\phi$ and $1-r_i \simeq t_i^2$. Meanwhile, the detuning of each arm to enable DC readout of the GW signal [3] is generally small (a few pm), this further implies that $2\Delta\phi \ll 1-r_i$. We can further define

$$g_a = \frac{t_i}{1-r_i} \simeq \frac{2}{t_i} \simeq 17. \tag{1.3}$$

Note that $g_a^2 \simeq 280$ is the power build-up inside the arm cavity, and $1/(1-r_i) \simeq g_a^2/2$. Using these approximations, the input-output relation can be simplified as

$$\frac{E_{\mathrm{arm}}}{E_1} \simeq -g_a\left(1+ig_a^2\Delta\phi\right), \tag{1.4a}$$

$$\frac{E_1'}{E_1} \equiv \bar{r}_i \simeq 1 - \frac{1}{2}g_a^2\Gamma_i + 2ig_a^2\Delta\phi, \tag{1.4b}$$

where we have defined $\bar{r}_i$ as the effective amplitude reflectivity by combining the arm cavity into a single mirror. For future convenience, we will further define $\bar{r}_{x(y)}$ as the the effective reflectivity of the X (Y) arm cavity. For the detuning, we consider it happens only in the differential mode, $\Delta\phi_x = -\Delta\phi_y$, and we define the differential-arm (DARM) detuning[1] as $\Delta\phi_d = \Delta\phi_x - \Delta\phi_y$. For the losses, we will keep track of both the common and differential ones, defined as $\Gamma_c = (\Gamma_x + \Gamma_y)/2$ and $\Gamma_d = (\Gamma_x - \Gamma_y)/2$, respectively.

The next step is to consider the Michelson part of the interferometer. The input-output relation for a Michelson that is on the dark fringe can be written as

$$\begin{bmatrix} E_2 \\ E_3 \end{bmatrix} = \frac{\sqrt{2}}{2}\begin{bmatrix} 1 & -1 \\ -1 & -1 \end{bmatrix}\begin{bmatrix} E_1 \\ E_4 \end{bmatrix}, \quad \begin{bmatrix} E_2' \\ E_3' \end{bmatrix} = \begin{bmatrix} \bar{r}_y & 0 \\ 0 & \bar{r}_x \end{bmatrix}\begin{bmatrix} E_2 \\ E_3 \end{bmatrix},$$

$$\begin{bmatrix} E_1' \\ E_4 \end{bmatrix} = \frac{\sqrt{2}}{2}\begin{bmatrix} 1 & -1 \\ -1 & -1 \end{bmatrix}\begin{bmatrix} E_2' \\ E_3' \end{bmatrix}, \tag{1.5}$$

---

[1]In some literatures (e.g., Ref. [4]) the DARM detuning is defined as $(\Delta\phi_x - \Delta\phi_y)/2$. Throughout this thesis we define DARM as $\Delta\phi_d = \Delta\phi_x - \Delta\phi_y$ in phase and similarly in displacement, because such a definition simplifies the connection to GW astrophysics. For a piece of GW signal with strain h passing through an aLIGO detector with arm length L, it creates a DARM displacement $\Delta L_d = \Delta L_x - \Delta L_y = hL$ in the long-wavelength approximation.

which leads to

$$
\begin{bmatrix} E_1' \\ E_4 \end{bmatrix} = \frac{1}{2} \begin{bmatrix} \bar{r}_x + \bar{r}_y & \bar{r}_x - \bar{r}_y \\ \bar{r}_x - \bar{r}_y & \bar{r}_x + \bar{r}_y \end{bmatrix} \begin{bmatrix} E_1 \\ E_4' \end{bmatrix}. \tag{1.6}
$$

Using Equation 1.4b, we can thus write

$$
\bar{r}_m \equiv \frac{1}{2} (\bar{r}_x + \bar{r}_y) \simeq 1 - \frac{1}{2} g_a^2 \Gamma_c, \tag{1.7a}
$$

$$
\bar{t}_m \equiv \frac{1}{2} (\bar{r}_x + \bar{r}_y) \simeq -\frac{1}{2} g_a^2 \Gamma_d + i g_a^2 \Delta \phi_d, \tag{1.7b}
$$

as the effective Michelson amplitude reflectivity and transmissivity.

We are now ready to study the carrier's propagation inside the signal-recycling cavity formed by the the compound Michelson and the SRM. For aLIGO, it operates under the resonant-sideband-extraction configuration [5], which detunes the SRM by $\pi/2$. As a result, when a field reflects upon the SRM it will pick up a phase of π. Similar to the case for the arm cavity, we can solve the fields at each point in terms of an input field E_1, leading to

$$
\frac{E_s}{E_1} = \frac{\bar{t}_m}{1 + \bar{r}_m r_s}, \tag{1.8a}
$$

$$
\bar{r}_s \equiv \frac{E_s}{E_1} = \bar{r}_m + \frac{\bar{t}_m^2 r_s}{1 + \bar{r}_m r_s} \simeq \bar{r}_m, \tag{1.8b}
$$

$$
\bar{t}_s \equiv \frac{E_{\text{out}}}{E_1} = \frac{\bar{t}_m t_s}{1 + \bar{r}_m r_s} = g_s t_m, \tag{1.8c}
$$

where we have defined $\bar{r}_s$ and $\bar{t}_s$ as the effective reflectivity and transmissivity of the compound cavity. In deriving $\bar{r}_s$, we have used the fact that $|\bar{t}_m|$ is already a small quantity, and therefore we can safely neglect the term that is quadratic in this quantity. We have also introduced the amplitude signal-recycling gain g_s, defined as

$$
g_s = \frac{t_s}{1 + r_m r_s} \simeq \frac{t_s}{2} \simeq 0.3. \tag{1.9}
$$

Lastly, we can bring in the PRM to form the complete interferometer. The fields

can now be written as

$$\frac{E_{\mathrm{p}}}{E_{\mathrm{in}}} = \frac{t_{\mathrm{p}}}{1 - r_{\mathrm{p}}\bar{r}_{\mathrm{m}}} = g_{\mathrm{p}}, \tag{1.10a}$$

$$\frac{E'_{\mathrm{in}}}{E_{\mathrm{in}}} = \frac{\bar{r}_{\mathrm{m}} - r_{\mathrm{p}}}{1 - r_{\mathrm{p}}\bar{r}_{\mathrm{m}}}, \tag{1.10b}$$

$$\frac{E_{\mathrm{out}}}{E_{\mathrm{in}}} = -\frac{t_{\mathrm{p}}\bar{t}_{\mathrm{s}}}{1 - r_{\mathrm{p}}\bar{r}_{\mathrm{m}}} \simeq -\frac{1}{2}g_{\mathrm{p}}g_{\mathrm{s}}g_{\mathrm{a}}^2\Gamma_{\mathrm{d}} + ig_{\mathrm{p}}g_{\mathrm{s}}g_{\mathrm{a}}^2\Delta\phi_{\mathrm{d}}. \tag{1.10c}$$

In the process we have introduced the amplitude power-recycling gain $g_{\mathrm{p}} = t_{\mathrm{p}}/\left(1 - r_{\mathrm{p}}\bar{r}_{\mathrm{m}}\right)$. For the parameters given in Table 1.1, the numerical values of $g_{\mathrm{p}} \simeq 7$, leading to a power-recycling gain of $g_{\mathrm{p}}^2 = 49$ in power. On the other hand, as pointed out in, e.g., Ref. [6], once the losses in the arm Γ_{c} is fixed, the optimal choice of the PRM is such that $r_{\mathrm{p}} = \bar{r}_{\mathrm{m}}$. Under this condition the carrier field is critically coupled to the power-recycling cavity with a vanishing field in reflection, $E'_{\mathrm{in}} = 0$. This condition was approximately satisfied in the aLIGO's first and second observing runs when $\Gamma_{\mathrm{c}} \simeq 100$ ppm. However, before the third observing run, new ETMs with better coating qualities are installed, which reduces the round-trip loss in the arm cavity down to about $\Gamma_{\mathrm{c}} \simeq 70$ ppm. If we want to maintain the critical coupling condition with the new arm cavities, the optimal power transmissivity of the PRM should be set to $T_{\mathrm{p}} = 2.0\%$.

To summarize, we can write the fields at different ports in terms of the input field and the different cavities' gain as

$$E_{\mathrm{p}} = -g_{\mathrm{p}}E_{\mathrm{in}}, \tag{1.11}$$

$$E_{\mathrm{x}} = -\frac{\sqrt{2}}{2}g_{\mathrm{p}}g_{\mathrm{a}}\left(1 + ig_{\mathrm{a}}^2\Delta\phi_{\mathrm{x}}\right)E_{\mathrm{in}}, \tag{1.12}$$

$$E_{\mathrm{y}} = \frac{\sqrt{2}}{2}g_{\mathrm{p}}g_{\mathrm{a}}\left(1 + ig_{\mathrm{a}}^2\Delta\phi_{\mathrm{y}}\right)E_{\mathrm{in}}, \tag{1.13}$$

$$E_{\mathrm{s}} \simeq \left(\frac{1}{4}g_{\mathrm{p}}g_{\mathrm{a}}^2\Gamma_{\mathrm{d}} - \frac{1}{2}ig_{\mathrm{p}}g_{\mathrm{a}}^2\Delta\phi_{\mathrm{d}}\right)E_{\mathrm{in}}, \tag{1.14}$$

$$E_{\mathrm{out}} = \left(-\frac{1}{2}g_{\mathrm{p}}g_{\mathrm{s}}g_{\mathrm{a}}^2\Gamma_{\mathrm{d}} + ig_{\mathrm{p}}g_{\mathrm{s}}g_{\mathrm{a}}^2\Delta\phi_{\mathrm{d}}\right)E_{\mathrm{in}}. \tag{1.15}$$

In the above set of equations, E_{in} is the input field with $P_{\mathrm{in}} = |E_{\mathrm{in}}|^2$ being the input

power, and E_{out} is the output field at the anti-symmetric port of the interferometer. The quantities E_{p}, E_{x}, E_{y}, and E_{s} correspond to the field inside the power-recycling cavity, the X-arm, the Y-arm, and the signal-recycling cavity, respectively, and $g_{\text{p}} = t_{\text{p}}/(1-r_{\text{p}}\bar{r}_{\text{m}}) = 7$, $g_{\text{s}} = t_{\text{s}}/(1+r_{\text{s}}\bar{r}_{\text{m}}) = 0.3$, and $g_{\text{a}} = t_{\text{i}}/(1-r_{\text{i}}) = 17$ are the amplitude gains in the power-recycling cavity, the signal recycling cavity, and the arms. In the expressions of g_{p} and g_{s} the effective reflectivity $\bar{r}_{\text{m}}$ of the compound Michelson-arms cavity is given by $\bar{r}_{\text{m}} \simeq 1 - \frac{1}{2}g_{\text{a}}^2\Gamma_{\text{c}} \simeq 0.99$.

In terms of power, we have

$$P_{\text{p}} = g_{\text{p}}^2 P_{\text{in}} = ...,\tag{1.16}$$

$$P_{\text{x}} = P_{\text{y}} = P_{\text{a}} = \frac{1}{2}g_{\text{p}}^2 g_{\text{a}}^2 = ...,\tag{1.17}$$

$$P_{\text{out}} = ...\tag{1.18}$$

1.2.2   The RF sidebands

1.3   Propagation of the AC fields

In this section we consider how the "AC" fluctuations of the ETMs at audio frequencies are translated to optical fields, and how those fields propagate through the interferometer. Meanwhile, we will also consider the propagation of the quantum fluctuation entering through the anti-symmetric port of the interferometer, and further derive the instrument's limitation . The derivation follows closely Ref. [7]; for the AC optical response of other mirrors we refer the reader to Ref. [4] for more discussions.

1.3.1   From mirror motion to optical field

To see the connection between a mirror's motion and the optical field reflecting upon it[2], we can consider the following example. Suppose the incident field is $E_1 = E\exp(-2\pi\mathrm{i}f_0 t)$ where $f_0 \simeq 3 \times 10^{14}$ Hz is the laser oscillation frequency, and the mirror (with $r = 1$) has a sinusoidal motion $\Delta l\cos\left(2\pi f t\right)$ where $f \ll \omega_0/2\pi$

---

[2]We focus on the normal incidence case for simplicity here.

is an audio-frequency on the order of a few Hz to a few kHz. The mirror's motion modulates the phase of the field in reflection with an amplitude of $\Delta\phi = 2\pi f_0 \Delta L/c$ and frequency f, which can be written as

$$
\begin{aligned}
E_1' &= E\mathrm{e}^{\mathrm{i}[2\pi f_0 t + 2\Delta\phi\cos(2\pi ft)]}, \\
&= E\mathrm{e}^{\mathrm{i}2\pi f_0 t}\left[\sum_{m=-\infty}^{\infty} \mathrm{i}^m J_m\left(2\Delta\phi\right)\mathrm{e}^{2\pi\mathrm{i}mft}\right],
\end{aligned}
\tag{1.19}
$$

where J_m is the Bessel function of the first kind. For small displacements, this expression can be further simplified as

$$
E_1' \simeq E\mathrm{e}^{\mathrm{i}2\pi f_0 t}\left[1 + \mathrm{i}\Delta\phi\mathrm{e}^{2\pi\mathrm{i}ft} + \mathrm{i}\Delta\phi\mathrm{e}^{-2\pi\mathrm{i}ft}\right].
\tag{1.20}
$$

Thus the field in reflection upon an oscillatory mirror can be modeled as the sum of an unperturbed DC field and two sidebands that are phase-shifted by $\pi/2$ with respect to the DC field and vary respectively at $\pm f$.

1.3.2 DARM signal

In the previous section we have derived the DC fields at each point of the interferometer, which serve as the "seed" fields from which the AC fields are generated. We now consider the propagation of the AC fields due to motions of the ETMs. Similar to the DC field study, we start by considering a single Fabry-Perot cavity correspond to the arm cavity. Since the AC motion is already a small quantity, we can thus ignore other small DC effects such as the DC detuning to the leading order. The steady-state solution satisfies the following set of equations,

$$
E_1'(f) = E_1(f) + \mathrm{i}\Delta\phi(f)E_1(0),
\tag{1.21a}
$$

$$
E_1(f) = r_\mathrm{i}\mathrm{e}^{-4\pi\mathrm{i}fL/c}E_1'(f),
\tag{1.21b}
$$

$$
\tag{1.21c}
$$

where $L = 3995$ m is the one-way arm length, $\Delta\phi(f) = 2\pi f_0 \Delta L(f)/c$ with $\Delta L(f)$ being the AC motion of the ETM. Again we have assumed the ETM being perfectly reflecting for simplicity. In the above equations we have explicitly indicated the frequency at which each quantity is varying (f for the AC quantities and 0 for the DC ones). This time, instead of solving all the fields in terms of an input field, we solve them in terms of the DC field $E_1(0)$ which we have derived in the previous section. This leads to

$$E_1'(f) = \frac{\mathrm{i}\Delta\phi(f)}{1 - r_\mathrm{i}\mathrm{e}^{-\mathrm{i}4\pi fL/c}}E_1(0) \simeq \frac{\mathrm{i}\Delta\phi(f)}{(1 - r_\mathrm{i}) + \mathrm{i}r_\mathrm{i}4\pi f\frac{L}{c}}E_1(0). \tag{1.22}$$

Note that due to causality, a field, after propagating a round trip in the cavity, will experience a phase shift of $-4\pi fL/c$ relative to the original one. When the phase lag is sufficiently large, the returning field will no more in-phase with the original one, which is essential to have constructive interference. This naturally leads to the pole frequency of the arm cavity, f_a, obtained by equating the magnitudes of the denominators real and imaginary part

$$1 - r_\mathrm{i} \simeq 4\pi r_\mathrm{i} f_\mathrm{a}\frac{L}{c}, \text{ or}$$

$$f_\mathrm{a} \simeq \frac{(1 - r_\mathrm{i})}{r_\mathrm{i}}\frac{c}{4\pi L} \simeq \frac{1}{g_\mathrm{a}^2}\frac{c}{2\pi L} \simeq 43 \text{ Hz.} \tag{1.23}$$

For motions with $f > f_\mathrm{a}$, the cavity filed will experience an asymptomatic $1/f$ filtering.

Now we consider how the differential-arm motion, or the DARM motion in the LIGO literature, propagates. Defining $\Delta L_\mathrm{x(y)}(f)$ to be the AC motion of ETMX (ETMY), for DARM we have $\Delta L_\mathrm{d}(f) = \Delta L_\mathrm{x}(f) - \Delta L_\mathrm{y}(f)$ with $\Delta L_\mathrm{x}(f) = -\Delta L_\mathrm{y}$, and the corresponding phase $\Delta\phi_\mathrm{d}(f) = 2\pi f_0 \Delta L_\mathrm{d}(f)/c$. Using the Michelson's input-output relation [equation (1.6)] and the fact that the DC field inside the X and Y arm cavities satisfies $E_\mathrm{x}(0) = -E_\mathrm{y}(0)$ [equations (1.12) and (1.13); ignoring DC detunings], for DARM motion we can conveniently combine the two arm cavities and the Michelson into a single DARM cavity, with the DC field inside this cavity given by

$E_\mathrm{d}(0) = -\sqrt{2}/2 E_\mathrm{x}(0) \simeq g_\mathrm{p} g_\mathrm{a} E_\mathrm{in}/2$, and the corresponding detuning of the combined differential ETM given by $\Delta\phi_\mathrm{d}$. The problem now becomes the derivation of field propagations inside the signal-recycled DARM cavity.

To proceed, we first combine the signal-recycling cavity formed by the SRM and ITM into a single effective ITM. The phase delay due to field propagation is ignored in the signal-recycling cavity because it is much shorter than the arms. The input-output relation is given by the following set of equations

$$E_\mathrm{s} = -r_\mathrm{i} E_\mathrm{s}' - t_\mathrm{i} E_1, \quad E_\mathrm{s}' = -r_\mathrm{s} E_\mathrm{s}, \tag{1.24a}$$

$$E_1' = r_\mathrm{i} E_1 - t_\mathrm{i} E_\mathrm{s}', \tag{1.24b}$$

$$E_\mathrm{out} = -t_\mathrm{s} E_\mathrm{s}. \tag{1.24c}$$

All the fields in the above equations vary at f and thus we omit it in the notation. Also note that while the DC carrier field is anti-resonance in the signal-recycling cavity, the AC signal sidebands are actually resonant in it. The difference is that for the DC fields, its reflectivity off the the ITM is determined by the interference between the field resonant in the arm cavity leaking through the ITM, and the field directly reflecting off the ITM, whereas for the signal sidebands, there is no direct reflection fields.

The above set of equations can be solved to obtain the reflectivity and transmissivity of the effective ITM formed by the signal-recycling cavity, which leads to

$$\tilde{r}_\mathrm{i} \equiv \frac{E_1'}{E_1} = \frac{r_\mathrm{i} - r_\mathrm{s}}{1 - r_\mathrm{i} r_\mathrm{s}}, \tag{1.25a}$$

$$\tilde{t}_\mathrm{i} \equiv \frac{E_\mathrm{out}}{E_1} = \frac{t_\mathrm{i} t_\mathrm{s}}{1 - r_\mathrm{i} r_\mathrm{s}}. \tag{1.25b}$$

Once the effective ITM is computed, the AC field inside the DARM cavity as well as the one propagate to the anti-symmetric port can be easily obtained by replacing

the r_i with $\tilde{r}_\mathrm{i}$ in equation (1.21). This leads to

$$E_\mathrm{d}(f) \simeq \frac{\Delta\phi(f)}{(1 - \tilde{r}_\mathrm{i}) + \mathrm{i}\tilde{r}_\mathrm{i}4\pi f \frac{L}{c}} E_\mathrm{d}(0), \tag{1.26}$$

for the AC field inside the DARM cavity, and the corresponding signal-recycled DARM cavity pole f_d, given by

$$f_\mathrm{d} = (1 - \tilde{r}_\mathrm{i})\frac{c}{4\pi L} \simeq f_\mathrm{a}\frac{1 + r_\mathrm{s}}{1 - r_\mathrm{s}} \simeq 420\mathrm{Hz}. \tag{1.27}$$

Thus, the signal-recycling cavity increases the single-arm cavity pole by a factor of $(1 + r_\mathrm{s})/(1 - r_\mathrm{s}) \simeq 1/g_\mathrm{s}^2 \simeq 10$ for $T_\mathrm{s} = 0.325$. The AC at the output port is readily given by

$$\begin{aligned} E_\mathrm{out}(f) &= \tilde{t}_\mathrm{i}E_\mathrm{d}(f) \\ &\simeq \mathrm{i}g_\mathrm{p}g_\mathrm{s}g_\mathrm{a}^2 E_\mathrm{in}(0)\frac{1}{1 + \mathrm{i}f/f_\mathrm{d}}\frac{\Delta\phi(f)}{2}, \end{aligned} \tag{1.28}$$

where we have used $E_\mathrm{d}(0) = g_\mathrm{p}g_\mathrm{a}E_\mathrm{in}(0)/2$. An overall propagation phase in the numerator has been omitted which does not affect any physical measureables.

Note that while the signal-recycling cavity reduced the amplitude of the signal field by a factor of $g_\mathrm{s} \simeq 0.3$, it broadens the signal bandwidth by a factor of $1/g_\mathrm{s}^2$. Therefore for high-frequency signals with $f > f_\mathrm{d}$, the signal field is enhanced by a factor of $1/g_\mathrm{s} \simeq 3$. As the merging frequency f_m of coalescing NS or BH binaries is approximately given by the GW frequency at the innermost stable circular orbit, $f_\mathrm{m} \simeq 1.6 \times 10^3\,(2.8\,M_\odot/M_\mathrm{t})$ Hz $> f_\mathrm{d} > f_\mathrm{a}$, with M_t being the total mass of the binary, such broadening is significant for increasing the instrument's sensitivity to the signals close to the final merger.

So far we have been focused on the upper side band with frequency $+f$. Propagation of the lower side band with $-f$ can be derived similarly. Without cavity detuning, it is easy to show that

$$E_\mathrm{out}(-f) = -E_\mathrm{out}^*(f), \tag{1.29}$$

where we have used the $*$ symbol to denote complex conjugation.

The detection of the signal fields is accomplished by interfering the signal sidebands $E_{\mathrm{out}}(\pm f)$ with a local oscillator field, E_{lo}, which creates a power fluctuation varying at $f > 0$ that can be further sensed by a photodiode (PD). Without special quantum manipulations that are beyond the scope of this thesis, the natural choice of the local oscillator field's phase is such that it maximizes the response to the signal. Without loss of generality we can set the input field to the interferometer E_{in} to be real and positive. Then to maximize the response to signal fields given by equations (1.28) and (1.29), the local oscillator field should then satisfy $E_{\mathrm{lo}}/|E_{\mathrm{lo}}| = \pm\mathrm{i}$. We can see from equation (1.15) that a DC detuning of DARM creates such a local oscillator field as long as the differential detuning is greater than the differential arm loss, $\Delta\phi_{\mathrm{d}}(0) \gg \Gamma_{\mathrm{d}}/2$. This is the DC readout technique currently used in aLIGO in which a DC DARM detuning of ~ 10 pm is introduced to sense the DARM displacements. Alternatively, one can pick off a small portion of the laser beam upstream as the local oscillation field and deliver it to the signal filed with proper phase control to enable the balanced-homodyne readout scheme [8].

In either case, the interference between the local oscillator and the signal fields can be written as

$$U(f) = E_{\mathrm{lo}}^*(0)E_{\mathrm{out}}(f) + E_{\mathrm{out}}^*(-f)E_{\mathrm{lo}}(0), \qquad (1.30)$$

for the term varying as $\exp(2\pi\mathrm{i}ft)$, and similarly $U(-f) = U^*(f)$ for the term varying as $\exp(-2\pi\mathrm{i}ft)$. At the PD, the sum $[U(f) + U(-f)]$ is then demodulated to DC by $\cos(2\pi ft)$ for the in-phase signal and by $\sin(2\pi ft)$ for the in-quadrature signal (also respectively known as the I- and Q-phase signals in the LIGO literatures). We can combine the real I- and Q-phase signals into a complex vector as $\mathrm{I} + \mathrm{i}\mathrm{Q}$ to write the final response in power at the readout PD, as

$$P(f) = 2U(f) = 2g_{\mathrm{p}}g_{\mathrm{s}}g_{\mathrm{a}}^2 \frac{1}{1 + \mathrm{i}f/f_{\mathrm{d}}} \sqrt{P_{\mathrm{in}}P_{\mathrm{lo}}}\Delta\phi_{\mathrm{d}}(f), \qquad (1.31)$$

where $P_{\mathrm{in}} = |E_{\mathrm{in}}|^2$ is the input power and $P_{\mathrm{lo}} = |E_{\mathrm{lo}}|^2$ the power in the local oscillator field. By writing $\Delta\phi_{\mathrm{d}}(f) = 2\pi f_0 \Delta L_{\mathrm{d}}(f)/c$, we obtain the optical transfer function

Z_d from DARM displacement to the readout PD as

$$
\begin{aligned}
Z_\mathrm{d} &\equiv \frac{\mathrm{d}P_\mathrm{d}}{\mathrm{d}\Delta L_\mathrm{d}} = 4\pi g_\mathrm{p} g_\mathrm{s} g_\mathrm{a}^2 \frac{1}{1 + \mathrm{i}f/f_\mathrm{d}} \frac{\sqrt{P_\mathrm{in} P_\mathrm{lo}}}{\lambda}, \\
&= \frac{2.3 \times 10^{10}}{1 + \mathrm{i}f/f_\mathrm{d}} \left(\frac{P_\mathrm{in}}{100\ \mathrm{W}} \right)^{1/2} \left(\frac{P_\mathrm{lo}}{0.1\ \mathrm{W}} \right)^{1/2} \frac{\mathrm{W}}{\mathrm{m}}.
\end{aligned}
\tag{1.32}
$$

Note that Z_d scales as g_a^2. This is because both the DC field building-up inside the arm cavity and the AC field generated from the DC field will experience the arm cavity's amplification. In contrast, the power-recycling cavity affects only the DC seed field and the signal recycling cavity affects only the AC signal field. As a result Z_d scales with g_p and g_s only to the linear order.

In the case of DC readout, the power in the local oscillator can be written as

$$
\begin{aligned}
P_\mathrm{lo} &= 4\pi^2 g_\mathrm{p}^2 g_\mathrm{s}^2 g_\mathrm{a}^4 P_\mathrm{in} \left(\frac{\Delta L_\mathrm{d}(0)}{\lambda} \right)^2, \\
&= 0.13 \left(\frac{P_\mathrm{in}}{100\ \mathrm{W}} \right) \left[\frac{\Delta L_\mathrm{d}(0)}{10\ \mathrm{pm}} \right]\ \mathrm{W}.
\end{aligned}
\tag{1.33}
$$

1.3.3   Quantum fluctuations

The quantum noise of the interferometer can be modeled as a quantum field $A_\mathrm{in}(f)$ entering from the antisymmetric port. This field both reflects off the interferometer and beats with the local oscillator field at the detection PD to create perturbations in the readout signal, and enters the arm cavities and interfere with the DC fields to create power fluctuations there that can displace the test masses via radiation pressure. The former corresponds to the shot noise and the later is known as the quantum radiation pressure noise (QRPN). In this section we provide a semi-classical derivation of those quantum limits. We will treat $A_\mathrm{in}(f)$ as a classical field instead of a quantum operator, and we simply enforce the amplitude spectra density of the beatnote between A_in and a classical DC field E (after summing over the signals at $\pm f$) to be $\sqrt{2\hbar\omega_0 P}$ with $P = |E|^2$. Without quantum squeezing, A_in has an equal amount of fluctuations in the amplitude and phase quadratures. The input-output relation we derive here, nonetheless, holds for both classical fields and quantum

operators.

The derivation of the propagation of A_{in} is very much similar to the ones presented in the previous sections. Thus we drop the details but just outline the procedures. Again consider the case of the signal-recycled DARM cavity, we can first map the ITM and ETM into a single effective ITM, and then combine to SRM and the effective ITM to compute the reflectivity of A_{in} by the interferometer. This gives us the shot noise. We can also solve for A_{in}'s propagation into the signal recycling cavity and then the DARM cavity. The important quantities in terms of A_{in} are

$$A'_{\text{in}} = \frac{1 - \mathrm{i}f/f_{\text{d}}}{1 + \mathrm{i}f/f_{\text{d}}} A_{\text{in}}, \tag{1.34}$$

$$A_{\text{a}} = g_{\text{s}}g_{\text{a}}\frac{1}{1 + \mathrm{i}f/f_{\text{d}}} A_{\text{in}}. \tag{1.35}$$

The shot noise of the system is given by beating A'_{in} with the local oscillator field E_{lo} at the readout port. The amplitude spectra density of it is given by

$$n_{\text{shot}}(\text{in W}/\sqrt{\text{Hz}}) = \sqrt{2\hbar\omega_0 P_{\text{lo}}}. \tag{1.36}$$

Dividing it by the optical response to the DARM motion leads to the shot-noise-limited sensitivity to DARM motion

$$n_{\text{shot}} = \frac{\lambda}{4\pi}\frac{\sqrt{2\hbar\omega_0/(1+\eta)}}{g_{\text{p}}g_{\text{s}}g_{\text{a}}^2 P_{\text{in}}^{1/2}}|1 + \mathrm{i}(\frac{f}{f_{\text{d}}})|. \tag{1.37}$$

The power fluctuation inside the arm cavity due to quantum fluctuation is obtained by beating A_{a} with the DC field inside the DARM cavities. In our mapping, to keep the power fluctuation inside the DARM cavity matches the real differential power fluctuation $\Delta P_{\text{d}} = \Delta P_{\text{x}} - \Delta P_{\text{y}}$, the DC field should be $-\sqrt{2}E_{\text{x}}(0) = g_{\text{p}}g_{\text{a}}E_{\text{in}}$. Then amplitude spectra density of the differential power fluctuation is given by

$$n_{\Delta P_{\text{d}}} = \frac{g_{\text{p}}g_{\text{s}}g_{\text{a}}^2}{|1 + \mathrm{i}f/f_{\text{d}}|}\sqrt{2\hbar\omega_0 P_{\text{in}}}. \tag{1.38}$$

Note that the DC field inside the arm and the local field at the antisymmetric port are

$\pi/2$ out of phase. Therefore, while the shot noise is due to the fluctuations of A_{in} in the "phase" quadrature, the power fluctuation inside the arm is due to the fluctuations in the "amplitude" quadrature of A_{in}. The power perturbation can directly cause displacement noise of the test masses which we will model as free masses with mass M. For a single mirror the displacement is related to the power fluctuation as

$$\Delta x(f) = \frac{\Delta P(f)}{2\pi^2 cM} \frac{1}{f^2}.\tag{1.39}$$

For the arm cavity another factor of two needs to be included to account for pushing both the ITM and ETM. Thus the amplitude spectra density of the QRPN is given by

$$n_{\text{QRPN}} = \frac{\sqrt{2} g_{\text{p}} g_{\text{s}} g_{\text{a}}^2 P_{\text{in}} \hbar \omega_0}{\pi^2 cM} \left| \frac{1}{1 + \mathrm{i} f/f_{\text{d}}} \right| \frac{1}{f^2}.\tag{1.40}$$

Chapter 2

Overview of alignment sensing and control in aLIGO

2.1 Optical Cavity and Gaussian Beams

?? In this section we review the basic concepts of Gaussian beams that are essential in our discussions of the alignment of optical cavities. The paraxial approximation is assumed throughout the chapter and it is generally well satisfied in aLIGO's case. For a more detailed and complete analysis, we refer the reader to Ref. [9].

An optical cavity can be formed with an input mirror and an end mirror, separated by a distance L. The cavity is stable if

$$0 < (1 - \frac{L}{\text{RoC}_i})(1 - \frac{L}{\text{RoC}_e}) < 1, \tag{2.1}$$

where $\text{RoC}_{i(e)}$ is the radius of curvature of the input (end) mirror. The quantities $\text{g}_{i,e} \equiv (1 - L/\text{RoC}_{i,e})$ are known as the cavity g-factors[1]. The eigenmodes of a (spherical) cavity define a complete orthonormal basis that allow us to expand an electric field as

$$E(f, x, y, z) = \sum_{mn} a_{mn}(f) u_{mn}(x, y, z), \tag{2.2}$$

---

[1]We will use the Roman g for the g-factors to distinguish them from an optical's amplitude gain inside a cavity, which is denoted with an Italic g.

where the $u_{mn} \in \mathbb{C}$ are the Hermite-Gauss functions, and the $a_{mn} \in \mathbb{C}$ are the amplitudes of the modes. The spatial coordinate (x, y, z) is chosen to be right-handed with the z-axis pointing along the direction of beam propagation and the y-axis vertically up. In this coordinate system, the mode order m (n) corresponds to nodes in the x (y) direction. We have omitted the temporal dependence as all the modes vary at the same frequency as E. For future convenience we further write $E_{mn} = a_{mn}u_{mn}$ and drop the (x, y, z) part as the indices m, n carry the spatial information already. Furthermore, to be consistent with FINESSE [2], we let the amplitude coefficient a_{mn} to absorb the Gouy phase of the Hermite-Guass modes, while leave the rest of the spatial dependence in the function u_{mn} normalized such that $\int \int u_{m'n'}^* u_{mn} \mathrm{d}x\mathrm{d}y = \delta_{mm'}\delta_{nn'}$. In the following, when we refer to a mode E_{mn} alone, unless specified, we will generally refer to its complex amplitude a_{mn} that includes the Gouy phase , whereas when we consider the interference between two fields $\propto E_{m'n'}^* E_{mn}$, we will let them follow the orthogonality dictated by u_{mn} with the integration range specified by the PD type (e.g., the whole-plane for a regular PD, and the upper/lower half-plane for a quadrant PD).

When the input beam is perfectly aligned and mode-matched to a cavity, the mode resonating inside the cavity corresponds to the spherical Gaussian mode with $m = n = 0$. We will also refer such a mode as the 00 mode for conciseness. The Gaussian mode is fully specified given the size and the location of its waist, which are further given in terms of the g-factors. If we choose the location of the waist to be at $z = 0$, then the input and end mirror's locations are respectively given by

$$z_{\mathrm{i}} = -L\frac{\mathrm{g_e}(1 - \mathrm{g_i})}{\mathrm{g_i}(1 - \mathrm{g_e}) + \mathrm{g_e}(1 - \mathrm{g_i})}, \tag{2.3a}$$

$$z_{\mathrm{e}} = L\frac{\mathrm{g_i}(1 - \mathrm{g_e})}{\mathrm{g_i}(1 - \mathrm{g_e}) + \mathrm{g_e}(1 - \mathrm{g_i})}, \tag{2.3b}$$

and the waist size w_0

$$w_0^2 = \frac{L\lambda}{\pi}\sqrt{\frac{\mathrm{g_i g_e}(1 - \mathrm{g_i g_e})}{(\mathrm{g_i} + \mathrm{g_e} - 2\mathrm{g_i g_e})^2}}. \tag{2.4}$$

Once the waist is specified, we can write the spot size at any location inside the

cavity as

$$w(z) = w_0 \sqrt{1 + \left(\frac{z}{z_0}\right)^2},$$ (2.5)

where $z_0 = \pi w_0^2/\lambda$ is the Rayleigh range. For $|z| < z_0$ it is known as the near field of the beam with the spot size $w(z) \simeq w_0$ stays approximately a constant, and for $|z| > z_0$ it corresponds to the far field where the spot size diverges as $w(z) \simeq w_0 z/z_0 = \theta_0 z$, with $\theta_0 = w_0/z_0$ the diffraction angle. The distinction between the near and far fields can also be characterized in terms of the Gouy phase $\eta(z) = \arctan(z/z_0)$, with $|\eta(z)| < \pi/4$ for the near field and $\pi/4 < |\eta(z)| < \pi/4$ for the far field.

Similarly the radius of curvature of the wavefront is given by

$$\text{RoC}(z) = \frac{z^2 + z_0^2}{z}.$$ (2.6)

Note that $\text{RoC}\left[z_{\text{i(e)}}\right] = \text{RoC}_{\text{i(e)}}$. For a Gaussian beam, the spot size and radius of curvature characterize the real and imaginary parts of the wavefront, respectively.

Now consider the case where a mirror is misaligned in pitch[2] with respect to the beam incident onto it. Upon reflection, the beam's wavefront will experience a differential phase delay at different locations in the xy-plane as it no more matches exactly to the curvature of the mirror. As a result, modes with different spatial orders will be generated. To the leading order in misalignment angle $\Delta\theta$, this can be written as [10][3]

$$\begin{bmatrix} E'_{00} \\ E'_{01} \end{bmatrix} = r \begin{bmatrix} 1 & \text{i}\frac{2\pi w}{\lambda}\Delta\theta \\ \text{i}\frac{2\pi w}{\lambda}\Delta\theta & 1 \end{bmatrix} \begin{bmatrix} E_{00} \\ E_{01} \end{bmatrix},$$ (2.7)

where the unprimed fields are the incident fields and the primed ones are the ones on reflection, and w is the spot size at the mirror's locations.

On the other hand, if a beam is shifted laterally along the y-axis by Δy, the leading

---

[2]Pitch corresponds to a rotation about the x-axis in the yz-plane in our coordinate system. Yaw, or rotation about the x-axis, will be similar and hence our discussion will be focused on the pitch case.

[3]Note that our sign convention follows the one used in FINESSE which has an overall sign flip relative to the one used in Ref. [10]. Also here we consider only the case of normal incidence. For the non-normal incident case, e.g., the alignment of a beamsplitter, we will discuss it in Appendix

order scattering matrix connecting the original basis to the shifted beam reads

$$
\begin{bmatrix} E'_{00} \\ E'_{01} \end{bmatrix} = r \begin{bmatrix} 1 & \frac{\Delta y}{w} \\ -\frac{\Delta y}{w} & 1 \end{bmatrix} \begin{bmatrix} E_{00} \\ E_{01} \end{bmatrix}. \tag{2.8}
$$

We can thus see that $\mathrm{Re}\,[E'_{01}/E'_{00}] \propto \Delta y/w$ while $\mathrm{Im}\,[E'_{01}/E'_{00}] \propto w\Delta\theta$. In other word, if we choose the 00 mode to be real, then a real 01 mode indicates a lateral shift and an imaginary 01 mode corresponds to a tilt with respect to the basis.

Also note that the relative the 00 mode, the 01 mode will experience an extra propagation phase shift η due to the Gouy phase [generically, for mode mn the Gouy phase shift relative to the 00 mode will be $(m+n)\eta$].

Knowing how a field reflects upon a mirror and how it propagates through through free space allows us to solve for the steady-state solution of a optical system with misalignments. The principles of this calculation [10] are similar to the ones we have used in, e.g., Section 1.2. As an illustration, we consider the case of a single Fabry-Perot cavity consisting of an ITM and an ETM, and focus on fields that vary temporally as $\exp\left(2\pi\mathrm{i}f_{\mathrm{RF}}t\right)$. Now instead of a single field E, we will consider a vector $\boldsymbol{E} = [E_{00}, E_{01}]^{\mathrm{T}}$. Here we focus on pitch and thus include only E_{01}; including E_{10} as well as modes with higher spatial order to the system is nonetheless straightforward. For the reflection upon the ETM, we can define a matrix

$$
\boldsymbol{M}_{\mathrm{e}} = r_{\mathrm{e}}\mathrm{e}^{2\pi\mathrm{i}\Delta\phi_{\mathrm{e}}} \begin{bmatrix} 1 & \mathrm{i}\frac{2\pi w_{\mathrm{e}}}{\lambda}\Delta\theta_{\mathrm{e}} \\ \mathrm{i}\frac{2\pi w_{\mathrm{e}}}{\lambda}\Delta\theta_{\mathrm{e}} & 1 \end{bmatrix}, \tag{2.9}
$$

where r_{e}, w_{e}, $\Delta\phi_{\mathrm{e}}$, and $\Delta\theta_{\mathrm{e}}$ are the amplitude reflectivity, spot size, microscopic detuning, and misalignment of the ETM, respectively. And similarly we define $\boldsymbol{M}_{\mathrm{i}}$ for the ITM. The propagation through free space is given by a propagation matrix

$$
\boldsymbol{P} = \mathrm{e}^{-2\pi\mathrm{i}f_{\mathrm{RF}}L/c} \begin{bmatrix} 1 & 0 \\ 0 & \mathrm{e}^{(0+1)\mathrm{i}\eta} \end{bmatrix}, \tag{2.10}
$$

where L and η are the one-way length and Gouy phase shift of the cavity. We are

42

Table 2.1: Spot sizes on the aLIGO mirrors in [mm].

PRM	PR2	PR3	ITM	ETM	SR3	SR2	SRM
2.3	6.2	54	53	62	54	8.2	2.1

now ready to obtain the cavity fields as

$$\boldsymbol{E}_{\mathrm{c}} = -t_{\mathrm{i}}\boldsymbol{E}_{\mathrm{in}} + \boldsymbol{M}_{\mathbf{i}}\boldsymbol{P}\boldsymbol{M}_{\mathbf{e}}\boldsymbol{P}\boldsymbol{E}_{\mathrm{c}}, \tag{2.11}$$

where $\boldsymbol{E}_{\mathrm{c}}$ is the cavity field evaluated right after the HR surface of the ITM, and $\boldsymbol{E}_{\mathrm{in}}$ is the input field entering the cavity. The above equation can be solved easily to obtain the higher-order mode content inside a cavity. Using the techniques of mapping a cavity into a single mirror as we have done in Section 1.2 then allows us to extend the analysis to complex optical system such as aLIGO.

In Table 2.1 we summarize the spot size on each aLIGO mirror and in Table 2.2 the one-way Gouy phase of each cavity. These are the parameters needed when solving equation 2.11.

Note that in the propagation matrix $\boldsymbol{P}$ the Gouy phase shift is frequency-independent. The significance of this property is as following. Suppose the carrier field is either propagating in the free space or is exactly on-resonance or anti-resonance inside a cavity, the 00 modes of the upper and lower RF sideband will then satisfy the relation that $E_{00}(+f_{\mathrm{RF}}) = -E_{00}^*(-f_{\mathrm{RF}})$, as their propagation phases satisfy $\phi_{00}(+f_{\mathrm{RF}}) = -2\pi f L_{\mathrm{prop}}/c = -\phi_{00}(-f_{\mathrm{RF}})$ where L_{prop} is the propagation distance. Therefore when consider the propagation of the 00 modes we can focus only on the upper sideband. This is no more the case when the higher-order modes are present because $\phi_{mn}(+f_{\mathrm{RF}}) = -2\pi f L_{\mathrm{prop}}/c + (m+n)\eta \neq -\phi_{mn}(-f_{\mathrm{RF}})$! Consequently, the higher-order modes at $+f_{\mathrm{RF}}$ will experience propagation effects and/or cavity filtering in an asymmetric manner with respect to the higher-order sidebands at $-f_{\mathrm{RF}}$. Consequently, no special symmetry property exists in general between $E_{01}(+f_{\mathrm{RF}})$ and $E_{01}(-f_{\mathrm{RF}})$.

Due to the orthogonality of the Hermite-Gauss function, the interference between a 01 mode and a 00 mode will vanish on a traditional whole-plane-integrated PD.

Table 2.2: One-way Gouy phases of aLIGO cavities

Power-recycling	Signal-recycling	Arm
25°	21°	146°

Nevertheless, if the integration is performed over the upper half-plane, the 00 and 01 mode will have a non-zero overlap, $\int_{-\infty}^{\infty} dx \int_0^{\infty} dy \, u_{00}u_{01} = 1/\sqrt{2\pi}$. As a result, to have a signal that is linearly dependent on the amplitude of the 01 mode (which encodes the alignment information to the linear order), we can interfere the signal 01 modes with a reference 00 mode, and detect the signal using a PD split into two halves[4]. Subtracting the upper and lower signals thus lead to the alignment information of interest. We will discuss the detection schemes in more details in Section 2.3.

Similar to that tilt and shift of a beam will generate 01/10 modes, if an incident beam has a spot size greater or smaller than that of the eigenmode of a cavity, real 02/20 modes will be generated from the 00 mode. On the other hand, if there exists a mismatch in the radius of curvatures between the input beam and the cavity eighenmode, it generates imaginary 02/20 modes. Those effects are closely related to the thermal state of the interferometer as the thermal lenses created by the high-input power will create radius of curvature mismatches between different cavities [11]. We will explore some of the consequences due to this effect in the next Chapter.

2.2   Degrees of Freedom

In this Section we consider the alignment degrees of freedom present in complex interferometers, which serves as a crucial first step in understanding the full alignment control scheme of aLIGO.

To start, we consider the case of aligning a Fabry-Perot cavity (for example, the arm cavity) to an input beam, as shown in Figure 2-1 Panel 1. We use the red-solid line to represent the input axis and the orange-dash line for the cavity axis. To achieve the maximum power buildup inside the cavity, the two axes need to be fully

---

[4]In reality we want the PD to be able to detect yaw signals simultaneously, and therefor a PD is divided into 4 quadrants.
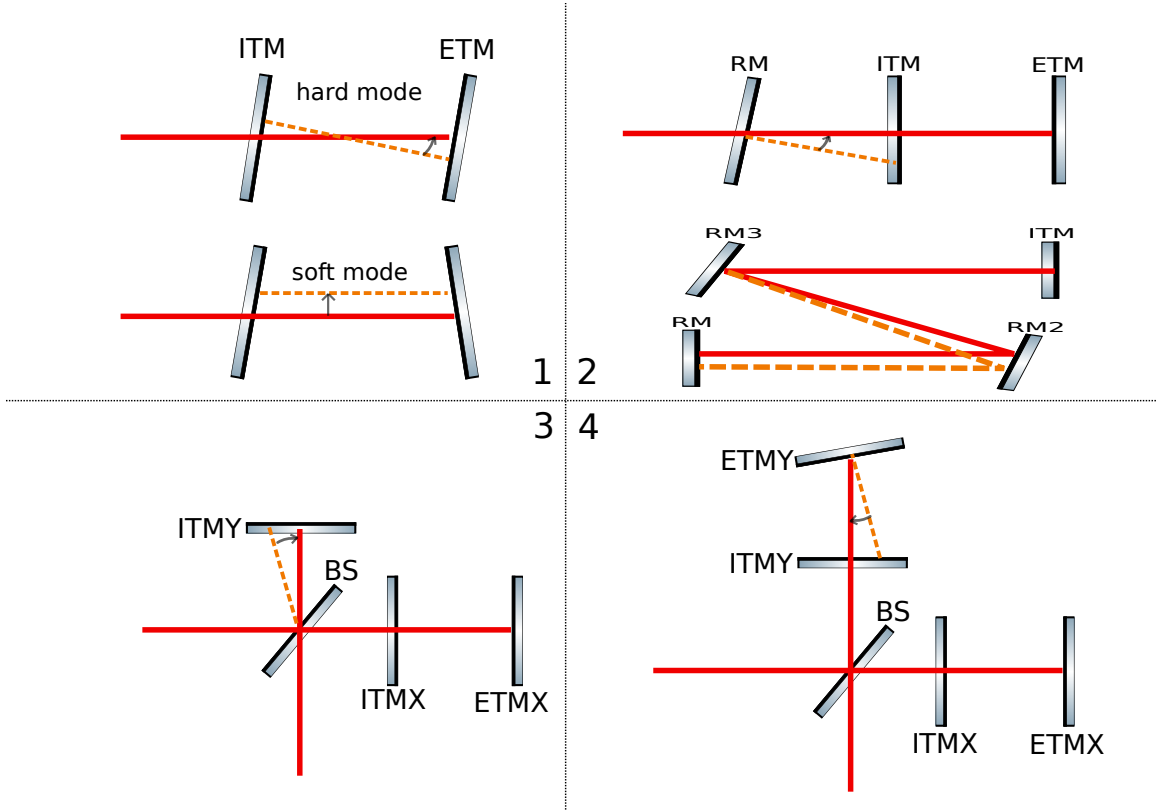
Figure 2-1: Carton illustrating the alignment degrees of freedom need to be controlled. In Panel 1 we consider the simple case of aligning a cavity's axis to the input axis. It has two interferometric degrees of freedom and one pointing degree of freedom. In Panel 2 we add a recycling mirror (RM) to the system. The upper part consider the case that the recycling cavity is a linear cavity in which a new interferometric degree of freedom is added. If the recycling cavity is a folded cavity, it also creates a pointing freedom. Panel 3 illustrate that adding a beamsplitter (BS) to the aligned input-Xarm system creates a new interferometric freedom, and lastly we consider the case of adding ETMY in Panel 4, which adds both an interferometric and a point degrees of freedom.

overlapped. This includes two degrees of freedom, corresponding to the tilt and shift of the cavity axis with respect to the input axis at the cavity waist, respectively. We will refer to the combined motion of the ITM and the ETM that generates a tilt at the cavity's waist as the hard mode, and the one that generates a shift as the soft mode. The reason for these names will become transparent when we discuss the effect of radiation pressure torque in Section 3.3. Note that besides aligning the cavity to the input beam, it is also possible to steer the input beam with two mirrors separated by some Gouy phase (ideally $\pi/2$) to align the input axis to the cavity, or to use one steering mirror at the input and one combinations of the test masses.

The two degrees of freedom discussed above involve the overlap between axes of two optical components. We will refer to such a degree of freedom as an "interferometric" degree of freedom. In contrast, another type of freedom exists in the system. Note that we can move the input axis and cavity axis together, which will change the spot position on the ETM. The power buildup inside the cavity, however, will not be affected as long as the motions keeps the two optical axes overlapped. We will refer to it as a "pointing" degree of freedom. Despite that a pointing degree of freedom does not directly affect the circulating power inside a cavity, we still need to control it as the scattering loss at different points of a mirror is different in general, and thus we use this freedom to point the beam to the location that minimizes the loss.

Now suppose we have the arm cavity and the input beam aligned both interferometrically and in pointing, and we want to add a recycling mirror (RM) into the system. Consider first the case that the recycling cavity is a linear cavity. Adding the RM will create a new interferometric degree of freedom as shown in the upper part of Panel 2 in Figure 2-1. Consider the beam returning from the arm cavity to the input port, when hitting the RM, it needs to be reflected back to be along the cavity axis to maximize the recycling gain. This condition thus determines the alignment of the RM. In reality, the recycling cavity is a folded cavity formed with three recycling mirrors (RM, RM2, and RM3). Thus, in addition to the interferometric freedom discussed above, there will also be a new pointing degree of freedom as illustrated in the lower part of Panel 2. For instance, it is possible to change the alignment of RM2

46

and RM3 to modify the spot position on the RM2, while keeping all the axes aligned as well as the pointing to the arm cavity. Note that we illustrated this new pointing freedom as the spot position on the RM2 only for conceptual simplicity. In reality it can be the spot on a different mirror depending on how we choose the interferometric degrees of freedom to be controlled first. The only critical thing is that the control scheme needs to include the right number of degrees of freedom (both the interferometric and the pointing ones), whereas the detailed implementation is non-unique and depends on other constrains such as the signal-to-noise ration of sensors.

We then consider the scenario that the input axis and the X-arm cavity axis have been aligned, and we want to add a beamsplitter and an ITMY to the system. This is illustrated in Panel 3. We can let the ITMY's location to be arbitrary and then the beamsplitter needs to be aligned such that it bisects the angle formed by the norms to the two ITMs. This corresponds to a new interferometric degree of freedom due to the Michelson interferometer.

Lastly, we can add the ETMY into the system. As can be seen from Panel 4, this corresponds to a new interferometric degree of freedom, because we need to align the ETMY so that the cavity axis of the Y-arm overlaps with the axis formed by the input beam and the beamsplitter in order to maximize the Y-arm's circulating power. Adding the ETMY also leads to a new pointing degree of freedom, as we can shift the Y-arm cavity perpendicular to its input (in the carton this corresponds to shift the ITMY and ETMY together along the x-direction) while keeping its cavity axis overlapped with the input one.

While in the carton above we separately consider the X-arm and the Y-arm, in practice it is often convenient to combine them into the common (X+Y) and differential (X−Y) basis. Such a change of basis is fine as long as the total number of degrees of freedom is preserved. Also note that in the carton we have only illustrated the motion in the plane of the page (i.e. the YAW motions). Similar motion can happen in pitch as well and therefore the total degrees of freedom should be doubled.

2.3   Detection Schemes

Before combining the components above together to form the full aLIGO system, we will discuss here first how we can extract an alignment signal. As we have separated the degrees of freedoms into two types, the interferometric ones and the pointing ones, we will consider their detection schemes individually.

2.3.1   Interferometric degrees of freedom

The most commonly used detection scheme for an interferometric degree of freedom is to interfere a carrier field with a pair of RF sidebands at a PD. When the PD is a regular full-plane integrated PD, the carrier-sidebands pair is used to lock the cavity in length using the Pound-Drever-Hall (PDH) technique [12]. To detect the misalignment, we further divide the PD into 4 quadrants. A pitch signal can be obtained by subtracting the upper and lower quadrants while a yaw signal by subtracting the right and left quadrants. Such a device is also known as a wave-front sensor (WFS) in LIGO literatures[5].

The generic working principle of this scheme is illustrated in Figure 2-2. For simplicity we assume the RF sidebands are off-resonance in the cavity. They directly reflects off the ITM and propagate to the WFS. The carrier field is assumed to be resonant in the cavity and thus probes its alignment. If the cavity is misaligned (modeled as a misalignment of the ETM), then it creates 01/10 mode from the carrier field. The carrier 01/10 mode also propagates to the WFS and interferes with the RF 00 modes, which can be further detected by the WFSs. In other words, we use the RF sidebands that encode the input beam's alignment as a spatial reference and compare the carrier field that samples the cavity's alignment to this reference. By zeroing the difference in power in the WFS's upper and lower, or right and left quadrants, we ensure the cavity is aligned with respect to the input beam.

Note that since the WFS operates at RF frequencies, to demodulate the signal

---

[5]Note that a WFS operates at an RF frequency. This is in contrast with a DC quadrant PD, or a DC QPD, which, as indicated by its name, detects signals at DC.
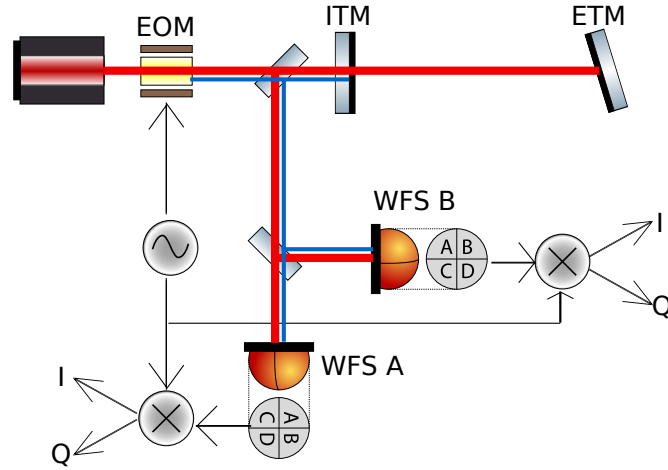
Figure 2-2: The generic principle of detecting an alignment signal with WFSs. The carrier field (represented by the red line) is resonant in the cavity and probes the cavity mode. The RF sidebands (the blue trace; they are generated by the electro-optic modulator, or the EOM), on the other hand, are off-resonance in the cavity and hence encodes only the information about the input beam. The two wave-fronts are compared at the WFSs, which are RF PDs with four quadrants. Subtracting the upper and lower halves leads signals for pitch misalignment and subtracting the right and left leads to signals for yaw. To account for the Gouy phase shift, two WFSs (A and B) separated by $\pi/2$ in Gouy phase are used. The carrier-sidebands pair is also used for the longitudinal locking via the PDH technique, which ensures the WFS signal to be free from contaminations due to DC spot drifts on the sensor.

down to DC a demodulation phase needs to be specified. Often this phase is chosen to be the same as the demodulation phase for the longitudinal PDH signal, and we will use I and Q to refer to the in-phase and in-quadrature signals, respectively. Moreover, since the 01/10 modes experience an extra Gouy phase shift η with respect to the 00 mode when propagation, to fully reconstruct the signal we need to put at least two WFSs separated by $\pi/2$ in Gouy phase per detection port. We will call them WFS A and B in the future.

A nice property of a WFS is that its signal is not contaminated by the spot's motion on the PD. If we again choose the carrier 00 field $E_{00}(0)$ to be real with the spatial coordinate defined by the cavity's eigenmode, then the RF 00 modes will satisfy $E_{00}(+f_{\mathrm{RF}}) = -E_{00}^*(-f_{\mathrm{RF}})$ for the upper and lower sidebands when the cavity is PDH locked. Therefore, the power due to the interference between carrier and RF 00 modes vanishes as $P_{\mathrm{spot}}(f_{\mathrm{RF}}) \propto E_{00}^*(0)E_{00}(+f_{\mathrm{RF}}) + E_{00}^*(-f_{\mathrm{RF}})E_{00}(0) = [E_{00}(+f_{\mathrm{RF}}) + E_{00}^*(-f_{\mathrm{RF}})] E_{00}(0) = 0$! In other words, even if the spot position on a WFS shifts with respect to the cavity basis, this motion will not be picked up by the WFS as the total power vanishes at f_{RF} without cavity misalignment[6]. Consequently, a WFS senses only the true wavefront distortion signal of the form $P_{\mathrm{WFS}}(f_{\mathrm{RF}}) \propto E_{01}^*(0)E_{00}(+f_{\mathrm{RF}}) + E_{00}^*(-f_{\mathrm{RF}})E_{01}(0)$, as $E_{01}(0) \in \mathbb{C}$ when we set $E_{00}(0)$ to be real. Also note that when detecting a pitch signal at the WFS, the spatial integration is performed only over half planes and the difference between the upper and lower halves is used (and similarly for yaw).

Besides using a WFS, an interferometric degrees of freedom can also be detected by dithering an optic and and then demodulate the fluctuations in the cavity's circulating power at the dithering frequency. This is because the fluctuations in the cavity's circulating power ΔP depends on the alignment quadratically, as

$$\frac{\Delta P}{P_0} \simeq \frac{1}{2}\left(\frac{\Delta\theta}{\theta_0}\right)^2 + \frac{1}{2}\left(\frac{\Delta y}{w_0}\right)^2, \tag{2.12}$$

where P_0 is the cavity's nominal circulating power (which is also the maximum power),

---

[6]This is the same reason why a PDH signal is insensitive to amplitude fluctuations.

$\Delta\theta$ and Δy are the tilt and shift at the cavity's waist, and θ_0 and w_0 are the cavity's divergence angle and spot size at the waist. Now suppose our dithering excitation creates a tilt signal $\Delta\theta_{\mathrm{exc}}(f_{\mathrm{exc}})$.[7] Then the power fluctuation at the dithering frequency f_{exc} can be written as

$$\frac{\Delta P(f_{\mathrm{exc}})}{P_0} \propto \left[\frac{\Delta\theta_{\mathrm{exc}}(f_{\mathrm{exc}})}{\theta_0}\right]\left[\frac{\Delta\theta(0)}{\theta_0}\right]. \tag{2.13}$$

Therefore, by introducing the dithering, the power fluctuation $\Delta P(f_{\mathrm{exc}})$ becomes a signal linearly proportional to the cavity's misalignment $\Delta\theta(0)$. This technique can be used to probe the cavity's alignment at DC or at frequencies much smaller than the dithering frequency f_{exc}.

In general, the dithering scheme is a much simpler setup than the detection using WFS, as it only requires a whole-plane PD operating at "DC" (that is, capable to detect signals in the audio-frequency band), whereas a WFS requires RF electronics capable to detect signals up to tens of MHz. Similar to the WFS technique, the dithering scheme is also insensitive to small spot motions on the diode as long as the incident beam is not clipping. The draw back, however, is that due to realistic constraints such as noise performance, the dithering excitation is in general a small number. As a result the dithering technique's sensitivity is usually orders of magnitude worse than that of using the WFS.

2.3.2   Pointing degrees of freedom

To detect a pointing degree of freedom, for example the spot position on the ETM, one can read out the signal at DC quadrant PDs (DC QPDs) in transmission of the ETMs. The signal takes the form of $P_{\mathrm{spot}}(0) \propto \mathrm{Re}\left[E_{01}^*(0)E_{00}(0)\right]$. Note that $E_{01}^*(0) \in \mathbb{C}$ due to the Gouy phase. Therefore two DC QPDs separated by $\pi/2$ are used at each detection port. Similar to the case of a WFS, the pitch motion is detected

---

[7]We will ignore the Δy_{exc} term as the analysis is similar. To fully sample the cavity's alignment we need two excitations respectively for the $\Delta\theta_{\mathrm{exc}}$ and Δy_{exc} terms, or for two different linear combinations of them. This is conceptually equivalent to using two WFSs separated by $\pi/2$ in Gouy phase.

by subtracting the upper and lower halves, and the yaw motion by subtracting the right and left halves. However, one major drawback of the DC QPD is that it cannot distinguish a true signal originated from the cavity from that due to the spot drift on the sensor. This is a serious issue in aLIGO as the table where the QPDs are mounted does drift with respect to the arm cavity in the timescale of a few hours because of the seismic motion.

Another approach for sensing a pointing degree of freedom is again using the dithering technique, but this time instead of reading the output signal from power fluctuations, the pointing information is encoded in the length perturbations. The "angle-to-length" coupling process can be easily understood geometrically, as shown in Figure . If the spot position on a mirror does not correspond to the mirror's rotational pivot, a length signal is created as

$$\Delta L(f_{\text{exc}}) \simeq \Delta y(0) \Delta \theta_{\text{exc}}(f_{\text{exc}}), \qquad (2.14)$$

where $\Delta y(0)$ is the distance between the spot position and the pivot. If we want to lock the spot instead to the pivot but another position, we can feedforward the angular signal to length as $\Delta L_{\text{ff}}(f) = -\Delta y_{\text{ff}} \Delta \theta(f)$, then the demodulated length signal will give us spot position measured in $[\Delta y(0) - \Delta y_{\text{ff}}]$.

The difference between the angle-to-length coupling (for sensing a pointing freedom) and the angle-to-power coupling (for sensing an interferometric degree) can also be understood in the modal picture. For convenience, we consider the case that the 00 mode is resonant inside the cavity and set its amplitude to be real positive. Suppose the DC spot position is off-centered on a mirror. In the modal picture this corresponds to a real 01 mode at DC incident onto the mirror. As we dither the mirror at AC, we scatter the real 01 mode into an imaginary AC 00 mode. This is exactly the same signal created by a longitudinal AC motion of the mirror. This thus corresponds to the angle-to-length coupling due to spot mis-centering (i.e., the existence of a real 01 mode at DC). Note that the scattered AC 00 mode is out-of-phase with the DC cavity field, and therefore it will not modify power circulating inside

the cavity. In contrast, if a beam is misaligned with respect to the mirror at DC, it means there is an imaginary 01 mode incident onto the mirror. The AC angular motion of the mirror will then scatter this imaginary 01 mode into a real 00 mode, which will further interfere with the DC cavity field and cause power fluctuations at AC, leading to angle-to-power coupling. However, due to the finite mass of the mirrors, the power fluctuation will also create a length signal via the radiation pressure force. This angle-to-power-to-length coupling may confuse the angle-to-length coupling due to spot mis-centering, and consequently contaminate the error signal used for sensing a pointing degree. This effect can be significant when aLIGO reaches 125 W of input power, and would thus deserve more detailed study in the future.

2.4 Alignment sensing and control in aLIGO

We are now ready to consider the alignment sensing and control in aLIGO. Based on our discussion in Section 2.2, for the pitch alignment there are in total 6 interferometric degrees of freedom and 4 pointing degrees of freedom, and for yaw the numbers are the same. To further assist our discussion, we can geometrically divide the interferometer into three parts (the symmetric/input part, the Michelson, and the anti-symmetric/output part), and study the degrees of freedom at each part individually.

Consider first the interferometric degrees of freedom. On the symmetric (or the input) side of the interferometer, which consists of the input beam, the power-recycling cavity, and the common-arm cavity, there are three interferometric degrees of freedom (cf. Panels 1 and 2 in Figure 2-1; note that we have replaced the single X-arm cavity by the common-arm cavity).

The first freedom is the common-hard mode of the arm cavities measured with respect to input axis coming from the power-recycling cavity. It can be sensed with a combination of WFSs located at the REFL port (which picks up the beam reflected-off the interferometer; see Figure 1-1) and the error signal is fed-back to the combination of test masses that corresponds to the common-hard motion with a bandwidth of 3
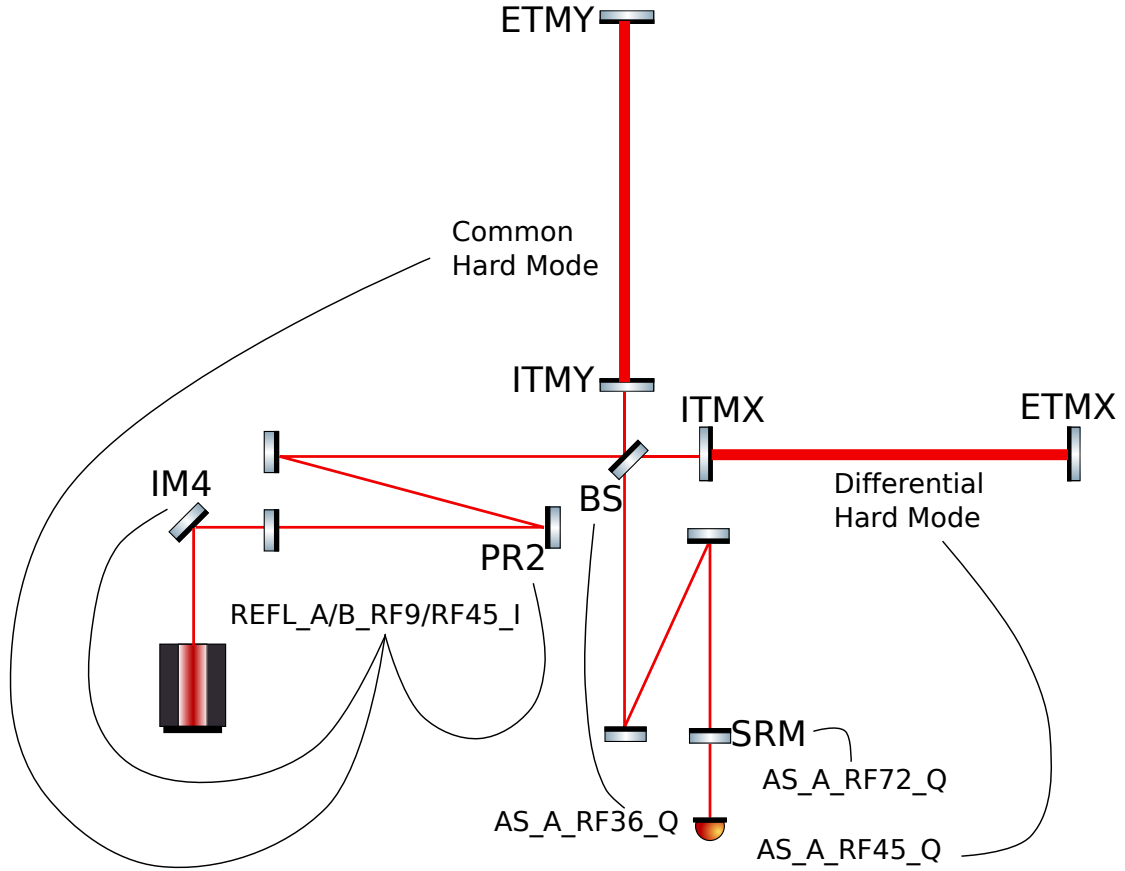
Figure 2-3: Alignment sensing and control of the interferometric degrees of freedom in aLIGO. On the symmetric side, we use three different linear combinations of REFL WFSs to overlap the axes of the input beam, the power-recycling cavity, and the common arm cavity. The Michelson and the differential arm axis are sensed with AS_A_RF36_Q and AS_A_RF45_Q, respectively. Lastly, the signal-recycling cavity's axis is aligned to the differential-arm cavity's axis by using AS_A_RF72_Q as the error signal.

Hz.[8].

The second degree of freedom aligns the power-recycling cavity's axis to the common-soft mode of the arm cavity (i.e., to minimize the lateral shift between the recycling cavity's axis and the arm cavity's axis at the waist of the arm cavity). Instead of controlling it with the test masses, this freedom is controlled with the PR2 mirror with a bandwidth of 0.5 Hz. Lastly, the input axis is aligned to the power-recycling cavity's axis by actuating on a steering mirror prior PRM with approximately 0.1 Hz bandwidth.

All the three degrees of freedom are sensed with the REFL WFSs. Specifically, we use four error signals which we will refer to as REFL_A/B_RF9/RF45_I. Here "REFL" stands for the detection port from which the signal is derived and the ports are defined in Figure 1-1. The "A" and "B" account for the two Gouy phases separated by $\pi/2$. The "RF9" and "RF45" are the RF frequencies at which a WFS is demodulated. Specifically, the "RF9" signal corresponds to the beat note between the carrier field and the ± 9.1 MHz sidebands, and similarly the "RF45" signal corresponds to the interference between the carrier field and ± 45.5 MHz sidebands. Lastly, the "I" stands for one of the RF demodulation phase that maximizes the whole-plane integrated signal's response to the common-arm motion in length; the other demodulation phase correspond to the "Q" signal which we do not use here. The right combination of sensors can be determined by exciting each degree of freedom individually and measuring the response in the individual sensor. Then such a sensing matrix can be inverted to give the proper linear combinations of sensors to be used as the error signal for each degree of freedom. Note that here we use four sensors (which are treated as linearly-independent) for three degrees of freedom. Such a system can be inverted with the Moore-Penrose pseudo-inverse algorithm.

The Michelson degree of freedom (cf. Panel 3 in Figure 2-1) is sensed with the AS_A_RF36_Q. Note here the "RF36" is from the beat note between the 9.1 MHz and 45.5 MHz sidebands. Unlike the beat note between the carrier and sidebands, the

---

[8]The actual alignment sensing and control of the arm cavity is an involved topic and we will dedicate the next Chapter to present a more detailed discussion

beat note between two sidebands will have a non-vanishing (whole-plane-integrated) power at the beat note frequency [13]. Therefore, we define the demodulation phase such that after demodulating the signal at 36.4 MHz, for each quadrant the DC power shows up all in the I phase. The orthogonal Q-phase signal is used here for sensing the the Michelson degree of freedom. We feedback this error signal to the beamsplitter with a bandwidth of 0.8 Hz.

On the anti-symmetric side, there are two more interferometric degrees of freedom. One corresponds to the differential-hard mode of the arm cavities. This degree of freedom is sensed with AS_A_RF45_Q, where the Q phase is defined to maximize the signal's response to the longitudinal differential-arm motion. The control is accomplished by feeding back the error signal to the four test masses in the linear combination that leads to the differential-hard motion with a bandwidth of 3 Hz.

The last interferometric degree of freedom is to align the signal-recycling cavity's axis to axis of the differential arm cavity by actuating on the SRM. Originally this signal signal was sensed using AS_A_RF36_I. However, it turned out that this signal was subject to thermal distortion of the system and could not be used for an input power exceeding 25 W. To overcome this issue, a new RF sideband has been added at 118.3 MHz, and we instead sense the SRM error signal using AS_A_RF72_Q, which is the beat note between the 118.3 MHz and 45.5 MHz sidebands at 72.8 MHz. The control bandwidth of this loop is set to around 0.1 Hz. We will discuss this sensing scheme in more detail in Section 4.1.

To summarize the discussions above, we show in Figure 2-3 a carton illustrating the sensing and control of all the interferometric degrees of freedoms in aLIGO.

As for the four pointing degrees of freedom, two of them corresponds the spot positions on the two ETMs. They are sensed by dithering the ETMs in angle and then demodulate the differential arm length signal at excitation frequencies. In other words, they are sensed utilizing the angle-to-length coupling effect [cf., equation (2.14)]. The error signal is then fed back to the combination of test masses corresponding to the soft-mode of each arm with a bandwidth of a few mHz. Similarly, we control the pointing degree of freedom in the power-recycling cavity by locking the PRM align-

ment to a fixed spot on the ITMY using the same angle-to-length coupling effect used for the arm cavity. Lastly, we point the SR2 alignment to a fixed spot on a DC QPD on the transmission of SRM to fix the pointing freedom of the signal-recycling cavity.

2.5 Tolerance on the corner degrees of freedom's residual angular motion

To complete our discussion on aLIGO's alignment sensing and control, we consider here the requirements set on each control loops. We will focus first on the corner degrees of freedom (i.e., the alignment of the recycling cavities and the Michelson), and defer the discussion of the arm cavities' requirements to the next Chapter.

In general, the major consideration on the alignment is that the control loop needs to suppress the residual angular motion to a sufficiently small value such that the interferometer can stay at its proper working point. Therefore, the question to ask naturally becomes the following. What is the definition of "sufficiently small" for each degrees of freedom?
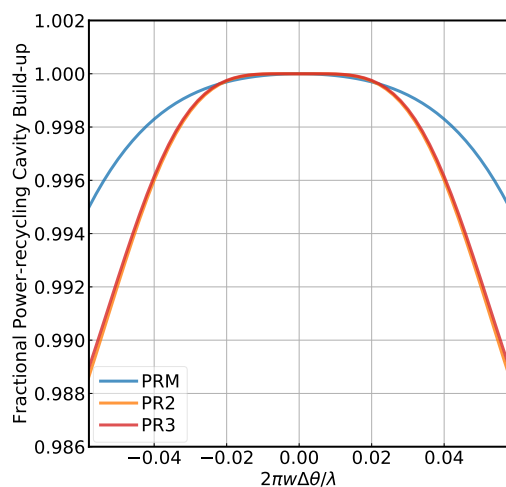
Figure 2-4: Fractional power build-up inside the power-recycling cavity as a function of the recycling mirrors' misalignment.

First consider the power-recycling cavity. Its purpose is to enhance the DC power

input to the arm, so that the shot-noise-limited sensitivity to DARM decreases by a factor of g_p [cf. equation (1.37)], with g_p being the carrier field's amplitude gain inside the power-recycling cavity. If the power-recycling cavity is misaligned, however, the value of g_p decreases as the carrier 00 mode loses its power to the higher-order modes. In Figure 2-4 we plot the fractional power build-up inside the power-recycling cavity ($\propto g_\mathrm{p}^2$) as a function of the misalignment of recycling mirrors (PRM, PR2, and PR3). The misalignments are plotted in units of the normalized angle $2\pi w \Delta\theta/\lambda$ where w is the spot size on the mirror. For a normalized angle of 0.01, it corresponds to misaligning the PRM, PR2, and PR3 by 0.74, 0.27, and 0.03 μrad, respectively. To reduce the power by 1% (corresponding to 0.5% increase in the shot noise), it requires a misalignment of at least 0.05 normalized angle, or at least 0.15 μrad misalignment of PR3. On the other hand, the input angular perturbation due to the seismic motion has a root-mean-square (rms) on the order of 0.1 μrad for each recycling mirror, already smaller than the value we could tolerant. Consequently, we only need a low-bandwidth ($\sim$ 0.1 Hz) control loop to overcome the long-term drift of power-recycling cavity's axis with respect to the input beam.
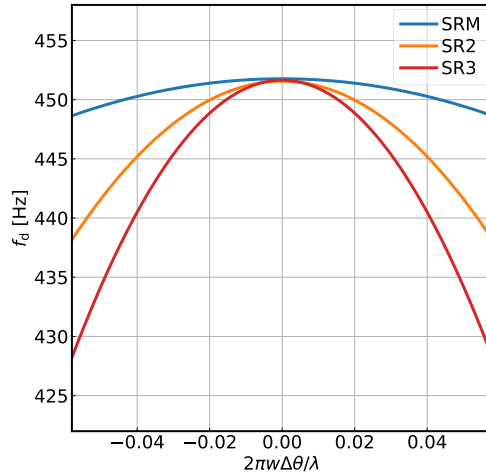
Figure 2-5: The DARM cavity frequency f_d as a function of the misalignment of the signal recycling mirrors (SRM, SR2, and SR3).

As for the signal-recycling cavity, the requirement is based on the DARM cavity

pole frequency f_d [cf. equation (1.27)]. As misalignment increases the loss inside the signal-recycling cavity, the DARM pole f_d decreases to lower frequency, reducing the instrument's sensitivity to GW signals with $f > f_d$. In Figure 2-5 we plot f_d as a function of the signal recycling mirrors' misalignment. The x-axis is again the normalized angle. The conversion is that a 0.01 normalized angle corresponds to a misalignment of SRM, SR2, and SR3 by 0.81, 0.21, and 0.03 μrad, respectively. To control the fluctuation in f_d to be less than 10 Hz, the rms in normalized angle needs to be $\lesssim 0.03$ (or at least 0.1 μrad SR3 misalignment). This is once again satisfied already by the raw input motion without needing extra loop suppression. Therefore, we also control SRM's alignment with a low-bandwidth feedback loop compensating only for the long-term drift.
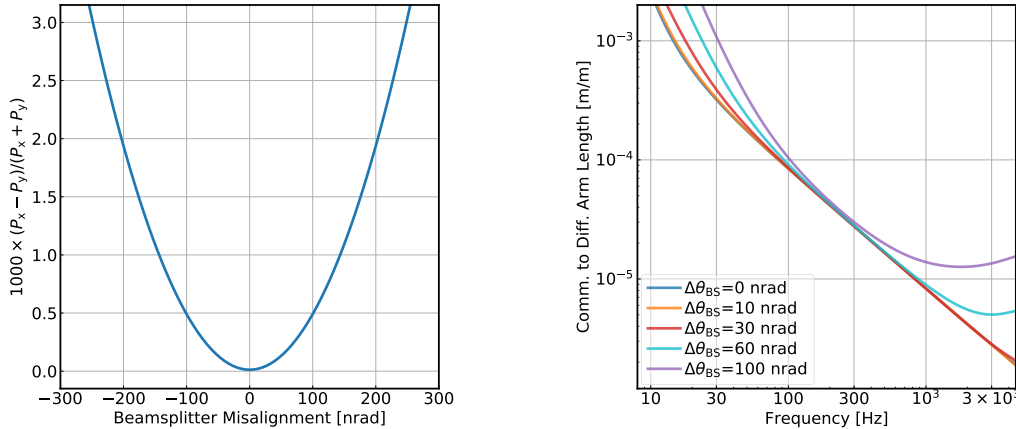
(a) The difference in the circulating power in the two arm cavities as a function of the beamsplitter's misalignment.

(b) Cross-coupling from CARM to DARM due at different level's of the beamsplitter's misalignment.

Figure 2-6: Requirements on the alignment of the Michelson degree of freedom.

Lastly, we consider the tolerance on the beamsplitter's alignment. One apparent consideration is that we need to keep the DC power level in both arms as high as possible. This is considered in Figure 2-6a where we plot the difference in the DC power buildup in the two arm cavities as a function of the beamsplitter's misalignment. At a misalignment of 100 nrad, the beamsplitter only induces a difference in the DC power level of 0.05%. As a comparison, the typical difference in the arm

losses ($|\Gamma_\mathrm{x} - \Gamma_\mathrm{y}|/2 \sim 10$ ppm) and the imbalance in ITMs' power transmissivity ($|T_\mathrm{ix} - T_\mathrm{iy}|/2 \sim 100$ ppm) will lead to a difference in the two arms' DC power on the order of 1%.

However, a more contingent requirement exists. If the Michelson does not stay on a perfect dark fringe, the common-mode motion such as the input laser's intensity and frequency noise will not be reflected back to the symmetric port but will instead leak to the anti-symmetric port, contaminating the DARM signal. In Figure 2-6b we consider the cross-coupling from the common-arm (CARM) motion (which is equivalent to the input laser's frequency noise) to the DARM signal. When the beamsplitter is perfectly aligned, the cross-coupling is due to the mismatch in the two arm's cavity pole frequencies caused by the difference it the ITM transmissivity (see, e.g., Ref [14]; we assume it to be $(T_\mathrm{ix} - T_\mathrm{iy})/2 = 100$ ppm here). When the beamsplitter is misaligned, the DC 01 modes it generated will enter the arm cavity and be modulated by the AC CARM motion. As the AC 01 mode propagates back to the misaligned beamsplitter, it will be scattered back to an AC 00 mode that is equivalent to a length fluctuation of the Michelson degree of freedom. This noise further couples to DARM with a coefficient $\frac{|1+\mathrm{i}f/f_\mathrm{d}|}{g_\mathrm{a}^2}$. Meanwhile, part of the AC 00 mode will also enter the arm cavities again and interfere with the DC cavity fields. This leads to an excess radiation pressure noise dominating the low-frequency cross coupling with a characteristic $1/f^3$ slope (note that in addition to the $1/f^2$ filtering due to the pendulum, there is another $1/f$ due to the filtering in the power-recycled CARM cavity). Based on the CARM-to-DARM cross-coupling, the residual beamsplitter motion should be controlled to $\lesssim 10$ nrad. Nevertheless, this requirement can still be satisfied by the raw input motion, as the beamsplitter is hosted in a BSC chamber, which provides 10 times more seismic isolation at the suspension point compared to the HAM chambers hosting the recycling mirrors [15, 16, 17]. To further increase the safety margin, we also have a relatively high-control bandwidth of 0.8 Hz on the Michelson's alignment control compared the loops used for the recycling cavities' alignment.

Chapter 3

Alignment control of the arm cavities

3.1 Control loop design considerations

In Section 2.5 we studied the requirements on the alignment degrees of freedom in the corner. We found that the rms of the raw input motion already satisfied the requirements, and hence low-bandwidth control loops handling the long-term drifts would be sufficient. However, this is no more the case when we consider the alignment of the arm cavity. This section is thus dedicated to discuss various requirements we should consider for designing the control feedback of the arm cavity.

Consider a feedback loop model as illustrated in Figure **??**. Here S is the suspension transfer function with in units of $[\mathrm{rad/N \cdot m}]$, and K is the control feedback gain in $[\mathrm{N \cdot m/rad}]$. We consider two kinds of noise input here. One is the displacement perturbation input to the system $\tau_{\mathrm{in}}^{(\mathrm{disp})}$, and the other is the sensing noise $\theta_{\mathrm{out}}^{(\mathrm{sens})}$. The closed-loop response to the noises can be respectively written as

$$\theta_{\mathrm{out}}^{(\mathrm{disp})} = \frac{S}{1 + KS}\tau_{\mathrm{in}}^{(\mathrm{disp})}, \tag{3.1}$$

$$\theta_{\mathrm{out}}^{(\mathrm{sens})} = \frac{KS}{1 + KS}\theta_{\mathrm{in}}^{(\mathrm{sens})}. \tag{3.2}$$

In Figure 3-1 we show the typical pitch noise input to the aLIGO's arm cavities. For the displacement noise, the dominant contribution is from the ground's longitudinal motion coupling to the test mass' pitch angle due to the suspension length-to-pitch

coupling [18] (labeled with "Seismic"). This is a unique coupling to pitch and the seismic noise input to yaw is much smaller. Another significant contribution is the local damping noise. This is the noise coming from the shadow sensors [19] that are used for reducing the quality factors of the suspension resonances. The total rms of the input displacement is ~ 10 nrad. On the other hand, the hard modes of the arm cavities generally has a sensing noise of $\theta_{\text{in}}^{(\text{sens})} \simeq 10^{14}$ rad/$\sqrt{\text{Hz}}$ [20].
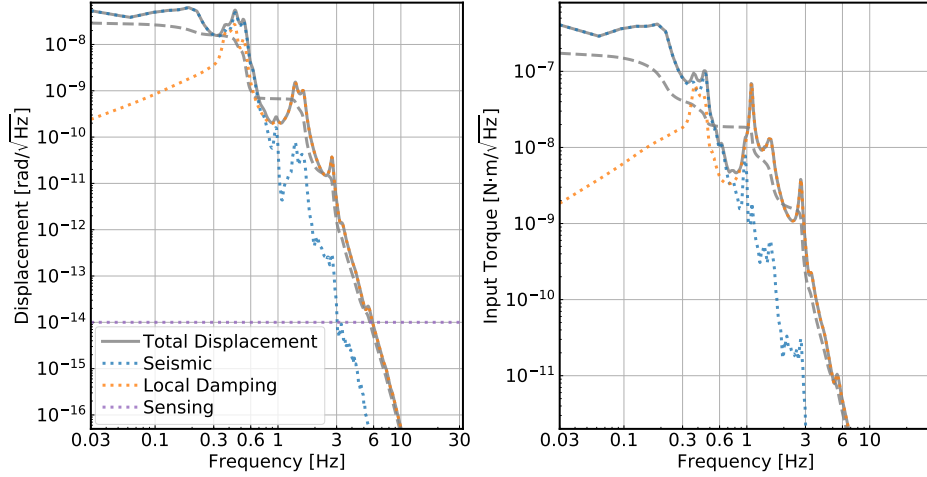
Figure 3-1: Typical pitch noise input to the aLIGO arm cavities. In the left we show noise in [rad/$\sqrt{\text{Hz}}$] and in the right we calibrate the displacement noise into the torque exerting on the test masses in [N · m/$\sqrt{\text{Hz}}$]. The total displacement (the grey-solid trace) is the quadratic sum of the seismic (blue-dotted) and local damping (orange-dotted) noises. The cumulative rms of the displacement perturbation is shown in the dashed-grey trace. Also shown in the purple-dotted line is the typical sensing noise level.

After knowing the input noise level, we need to consider next the requirements should be set on the closed-loop noises $\theta^{(\text{disp})}$ and $\theta^{(\text{sens})}$. Specifically, there are two requirements related respectively to the low-frequency ($\lesssim 1$ Hz; dominated by the displacement noise) and the high-frequency ($\gtrsim 10$ Hz; dominated by the sensing noise) portions of the spectrum.

At low frequencies, we need to suppress the residual rms motion to a sufficiently small value. This is similar to our consideration in Section 2.5. In Figure 3-2 we present the fractional power build-up inside the arm cavity as a function of arm

misalignment (in the hard/soft basis). Note that the shot-noise-limited DARM sensitivity scales as $1/g_{\mathrm{a}}^2$ [cf. equation 1.37], and thus a reduction of the power build-up inside the arms by 1% will lead to an increase in the shot noise level by 1%. This is in contrast to the case of the build-up inside the power-recycling cavity where the DARM sensitivity scales only as $1/g_{\mathrm{p}}$. From Figure 3-2 we can see that to keep the build-up above 99% of its nominal value, we should control the hard modes to within 5 nrad rms. The requirements on the soft modes[1] is less strict and it can tolerate up to 20 nrad of rms fluctuation.
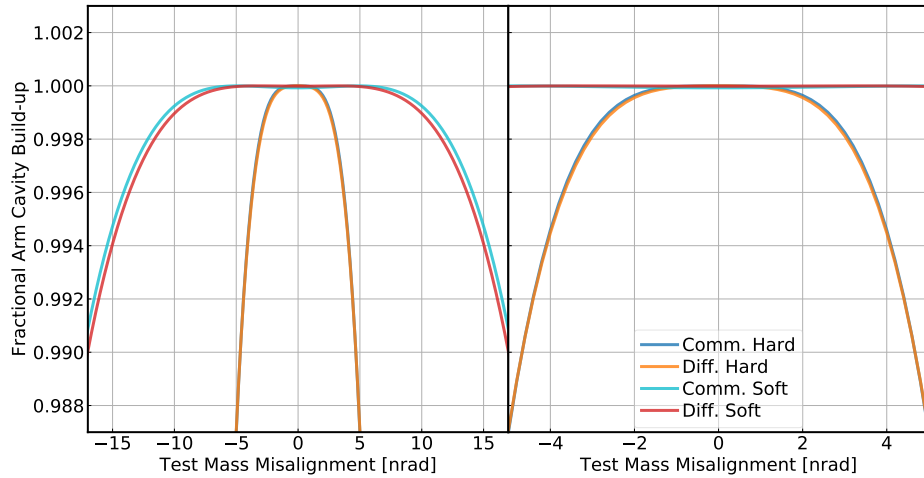
Figure 3-2: Fractional power build-up in the arm cavities as a function of the misalignment in the hard and soft modes. For a 1% reduction in the arm build-up (corresponding to 1% degradation in the shot-noise-limited sensitivity) it corresponds to 5 nrad misalignment in the hard modes and 20 nrad in the soft modes.

Another consideration is the degradation of the common-mode rejection because of misalignment, which we study in Figure 3-3. Here we can see that misalignments in the differential hard mode (and similarly in the common hard mode) enhances the CARM-to-DARM coupling at $\lesssim 30$ Hz via the radiation pressure effect. While the CARM/input frequency noise is usually well-suppressed below 100 Hz, other common-

---

[1]Here we mean specifically the "interferometric" soft mode, which is measured with respect to the power-recycling cavity's axis. It is actually controlled by actuating on PR2. See Section 2.4. This should be distinguished with the "pointing" soft mode which measures the mirrors motion with respect to the ground. See also Section 3.4.

mode noise such as the input jitter will couple in a similar manner [21]. Consequently, we would like to control the hard-mode motion to a rms of around 1 nrad, which is a more stringent constraint than the one set on power-build up.
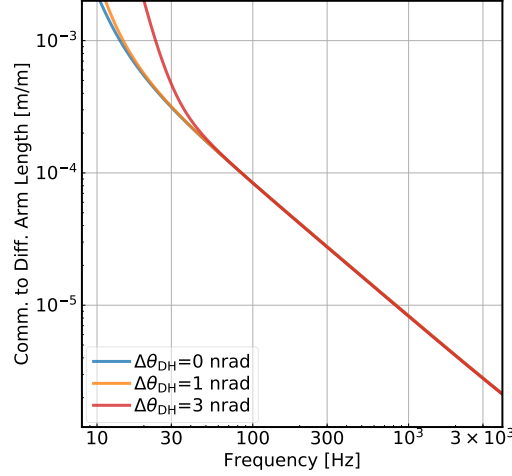
Figure 3-3: CARM to DARM cross-coupling at different levels of misalignment in the differential hard mode $\Delta\theta_{\mathrm{dh}}$.

At high frequencies ($\gtrsim 10$ Hz), the control loop feeds back the sensing noise and perturbs the test masses in angle. It can further couple to the DARM readout via the angle-to-length cross-coupling (Section 2.3.2; also Ref. [22]). The typically coupling coefficient is [21]

$$Z_{\mathrm{a2l}} \simeq 1 \ \left[\frac{\mathrm{mm}}{\mathrm{rad}}\right]. \tag{3.3}$$

This is greater than the residual spot motion created by the rms fluctuations of the alignment loops (which should be $\lesssim 0.1$ mm), and is likely to be due to the DC offsets in the pointing loops. If we want the angular noise to be below the designed DARM sensitivity at 10 Hz, or 6×10^{-19} m/$\sqrt{\mathrm{Hz}}$, we need to reduce the closed-loop sensing noise $\theta^{(\mathrm{sens})}(10 \ \mathrm{Hz}) < 6 \times 10^{-16}$ rad/$\sqrt{\mathrm{Hz}}$. In other words, the open-loop transfer function needs to be reduced to $KS < 0.06$ at 10 Hz.

To summarize, the alignment control of the arm cavity should have a sufficiently large bandwidth to suppress the sub-1 Hz input motion from a rms of about 10 nrad down to 1 nrad. At the same time, it needs to be rolled-off fast enough to be smaller

than 0.06 at 10 Hz. These two regions need to be connected in the $1 - 10$ Hz band such that it satisfies the stability requirement, $1 + KS \neq 0$. Yet another constraint is that the control loops need to stabilize the radiation torques and we will discuss it soon in the coming Section.
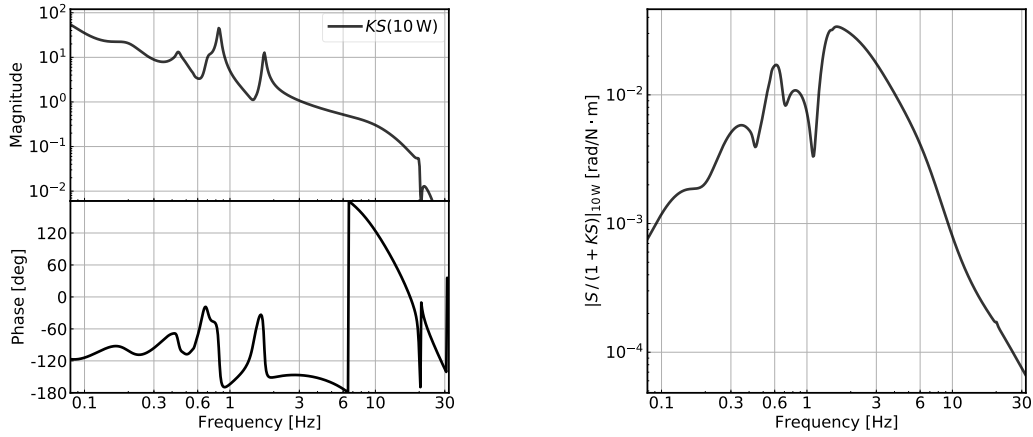
(a) The open loop transfer function $KS(10 \text{ W})$.

(b) The closed loop torque-to-angle transfer function $|S/(1 + KS)|_{(10 \text{ W})}$.

Figure 3-4: Control filters currently used for stabilizing aLIGO's differential-hard mode alignment in pitch. It is evaluated at an input power level of 10 W (or 57 kW of circulating power in each arm).

Currently, the filter used for controlling the pitch motion of the differential-hard mode at the Hanford site is shown in Figure 3-4. Combine it with the input motion shown in Figure 3-1 leads to the closed-loop residual angular motion[2] shown in Figure 3-5 .

From Figure 3-5 we can see that our current controller satisfies the low-frequency requirement on the residual rms; it suppresses the input motion to an rms of 0.4 nrad $<$ 1 nrad. However, in the $10 - 20$ Hz band our current control loop fails to meet the aLIGO's requirement on the roll-off of the sensing noise (shown in the red curve). One reason we do not use a lower-bandwidth and more-aggressively-rolled-off loop

---

[2]Note that multiplying the input noise in $[\text{rad}/\sqrt{\text{Hz}}]$ as shown in the left panel of Figure 3-1 by $[1/(1 + KS)]_{(10 \text{ W})}$ does not lead the appropriate closed-loop displacement noise as it does not account for the effect of radiation pressure correctly. See Section 3.3. The correct way is to take the torque noise input (the right panel of Figure 3-1) and then multiply it by $[S/(1 + KS)]_{(10 \text{ W})}$
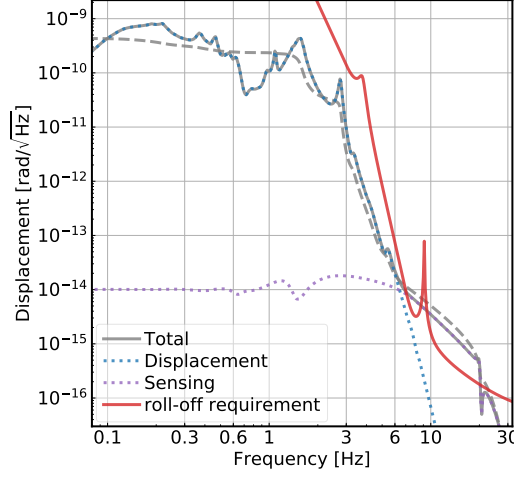
Figure 3-5: The closed-loop residual pitch motion of the differential-hard mode. The grey-solid trace is the total motion by summing the displacement (blue-dotted) and the sensing (purple-dotted) noises in quadrature. The cumulative rms motion is shown in the dashed-grey trace.

is that the effect of radiation pressure will modify the suspension transfer function S as a function of arm circulating power. It means that a controller designed at one power-level may become unstable at another power. Consequently a conservative design is chosen. We will use the next Section to discuss how the effect of radiation pressure modifies the control loop, and more importantly, how we can compensate for such an effect so that in the future we do not need to worry about variations in the plant. This will further open up the possibility of reducing the alignment control to a level below the aLIGO's fundamental quantum and thermal limits.

3.2 Effects of radiation pressure: an introduction

In this section we study the interactions between the radiation torques and the suspended test masses, which are the key component of designing the controller of the arm cavities' alignment in aLIGO.

To start, consider first the radiation torque exerted on a test mass in the time

66

domain. The torque exerting on the upper half plane can be written as

$$\tau^{(\text{up})}(t) = \frac{2}{c} \int_{-\infty}^{\infty} \mathrm{d}x \int_{0}^{\infty} \mathrm{d}y \left[y E_{00}(t, x, y) E_{01}(t, x, y) \right], \tag{3.4}$$

where we have omitted terms such as $E_{00}E_{00}$ as terms with even parity will be canceled out as we subtract the upper and lower halves and thus not contribute to the total torque. To proceed, we can further write the fields as

$$E_{mn}(t, x, y) = a_{mn}(t)u_{mn}(x, y), \tag{3.5}$$

where $u_{mn} = u_m u_n$ is the normalized Hermite-Gauss function [cf. equation (2.2)]. The spatial integration thus leads to

$$\int_{0}^{\infty} y u_0(y) u_1(y) \mathrm{d}y = \frac{w}{4}, \tag{3.6}$$

where w is the spot size on the mirror. By subtracting the upper and lower halves and utilizing the spatial symmetry $\tau^{(\text{low})} = -\tau^{(\text{up})}$, we have

$$\tau(t) = 2\tau^{(\text{up})}(t) = \frac{w}{c} a_{00}(t) a_{01}(t). \tag{3.7}$$

Now we can transfer to the Fourier domain[3] and use the bi-linear approximation to compute the fluctuations in the torque $\delta\tau(f)$ at frequency f, which leads to [without losing generality, we set $a_{00}(0)$ to be real in the equations below],

$$
\begin{aligned}
\delta\tau(f) &\simeq \frac{w}{c} \left[a_{01}(f) + a_{01}^*(-f) \right] a_{00}(0) + \frac{w}{c} a_{01}(0) \left[a_{00}(f) + a_{00}^*(-f) \right] \\
&\simeq \frac{2a_{00}^2(0)}{c} \left(w\mathrm{Re}\left[\frac{a_{01}(f)}{a_{00}(0)} \right] \right) \\
&\quad + \frac{2a_{00}^2(0)}{c} \left(w\mathrm{Re}\left[\frac{a_{01}(0)}{a_{00}(0)} \right] \right) \mathrm{Re}\left[\frac{a_{00}(f) + a_{00}^*(-f)}{2a_{00}(0)} \right].
\end{aligned} \tag{3.8}
$$

---

[3]Instead of denoting the Fourier transform of a quantity $q(t)$ as $\hat{q}$, we will omit the "hat" symbol and denote it as $q(f)$.

Or

$$\delta\tau(f) \simeq \frac{2P_{\mathrm{DC}}}{c}\delta y(f) + \frac{2P_{\mathrm{DC}}}{c}y(0)\left[\frac{\delta P(f)}{P_{\mathrm{DC}}}\right], \tag{3.9}$$

where we have used

$$P_{DC} = a_{00}^2(0), \tag{3.10}$$

$$y(f) = \mathrm{Re}\left[\frac{a_{01}(f)}{a_{00}(0)}\right] \text{ with } a_{01}(f) + a_{01}^*(-f) \simeq 2\mathrm{Re}\left[a_{01}(f)\right], \tag{3.11}$$

$$\frac{\delta P(f)}{P_{\mathrm{DC}}} = \mathrm{Re}\left[\frac{a_{00}(f) + a_{00}^*(-f)}{2a_{00}(0)}\right]. \tag{3.12}$$

Clearly, there are two effects that may cause a radiation torque perturbation on the test mass. One is associated with the fluctuation in the spot position $\delta y(f)$ [i.e., the first term in equation 3.9]. As we shall see soon, this term directly leads to the Sidles-Sigg effect [23] that has been a critical concern in LIGO's commissioning [24, 25]. We will discuss this effect in detail in Section 3.3 and provide there a technique that can compensate for this effect. The second term illustrates another type of radiation pressure effect, a torque that is due to power fluctuation $\delta P(f)$. Although in the ideal case, if a cavity is perfectly aligned in DC, any small AC misalignment will not generate fluctuations in power in the linear order. Nevertheless, in reality offsets in the alignment loops exist inevitably, which creates linear coupling to power fluctuations. Instabilities due to this effect were observed during aLIGO's second observing run [26, 27]. We will talk about this effect in Section 3.4.

3.3   The Sidles-Sigg effect

3.3.1   Interactions between the radiation torque and the suspention pendulum.

In the original work by Sidles and Sigg [23], the authors described the radiation torque in terms of the effect potential of the optical cavity. Specifically, the authors showed

that the potential energy W depends quadratically on the alignments of the two test masses $\boldsymbol{\theta}$, as $W = \boldsymbol{\theta}^{\mathrm{T}} \boldsymbol{R} \boldsymbol{\theta}/2$. In other words, the radiation torque couples the two test masses together to form an "optical spring", with the two eigenvectors of the stiffness matrix[4] $\boldsymbol{R}$ corresponding to the hard and soft modes. The geometrical representation of the hard and soft modes has been shown in Panel 1 of Figure 2-1. As illustrated in the carton, if the two test masses are misaligned in the hard mode, the radiation torque will then tend to push them back to the original location. Hence the hard mode "hardens" the optical spring. In contrast, a soft mode misalignment creates an optical torque that pushes the mirrors to be even more misaligned, and consequently "softens" the optical spring.

In this Section, we present an alternative way to study the same effect. Suppose that some initial torque perturbation causes the test masses to be misaligned by $\delta\boldsymbol{\theta}$. The misaligned mirrors alter the cavity axis and modify the spot positions on the test masses $\delta\boldsymbol{y}$. Then, as we have shown in equation 3.9, the perturbation in the spot positions in turn creates an optical torque on the test masses. The whole process can be modeled as a feedback loop as shown in Figure 3-6. In the plot, S_0 is the free pendulum transfer function, and the torsional stiffness can be further written as $\boldsymbol{R} = (2P_{\mathrm{a}}/c)\,\mathrm{d}\boldsymbol{Y}/\mathrm{d}\boldsymbol{\Theta}$, where P_{a} is the power circulating in the arm cavity [cf. equation (1.17)], and the matrix $\mathrm{d}\boldsymbol{Y}/\mathrm{d}\boldsymbol{\Theta}$ connects mirrors' misalignment $\delta\boldsymbol{\theta}$ to the spot position variations on the test masses $\delta\boldsymbol{y}$.

If we first consider the case of a single Fabry-Perot cavity. We let $\delta\boldsymbol{\theta} = [\delta\theta_{\mathrm{e}},\ \delta\theta_{\mathrm{i}}]$ with $\delta\theta_{\mathrm{e(i)}}$ being the misalignment of the ETM (ITM), and similarly for $\delta\boldsymbol{y}$. Then in terms of the cavity g-factors we can write $\mathrm{d}\boldsymbol{Y}/\mathrm{d}\boldsymbol{\Theta}$ as

$$\frac{\mathrm{d}\boldsymbol{Y}}{\mathrm{d}\boldsymbol{\Theta}} = \frac{L}{1 - \mathrm{g_i g_e}} \begin{bmatrix} -\mathrm{g_i} & 1 \\ 1 & -\mathrm{g_e} \end{bmatrix}. \tag{3.13}$$

Note that it has the same set eigenvectors as $\boldsymbol{R}$. The hard and soft modes can be

---

[4]Note that we have changed the notation of the stiffness matrix to be $\boldsymbol{R}$ instead of $\boldsymbol{\kappa}$ in Ref. [23].
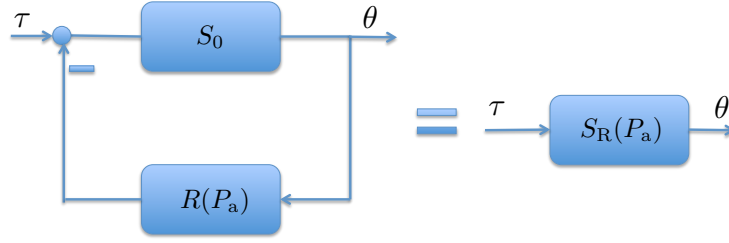
Figure 3-6: The signal flow diagram illustrating the Sidles-Sigg effect. Suppose some initial torque τ perturbs the mirror in angle θ. It changes the cavity beam's pointing on the mirror, which in turn couples with the DC circulating power to create a radiation torque. It thus creates a feedback loop and modifies the free pendulum transfer function S_0 to be a power-dependent quantity $S_R(P_a)$.

respectively written as

$$\delta\boldsymbol{\theta}_h = \begin{bmatrix} 1 & \bar{g} \end{bmatrix}^T, \tag{3.14a}$$

$$\delta\boldsymbol{\theta}_s = \begin{bmatrix} -\bar{g} & 1 \end{bmatrix}^T, \tag{3.14b}$$

where

$$\bar{g} = \frac{(g_e - g_i) + \sqrt{(g_e - g_i)^2 + 4}}{2} \simeq 0.87. \tag{3.15}$$

When evaluating $\bar{g}$, we have plugged in the g-factors for aLIGO, which are $g_e = -0.78$ and $g_i = -1.06$. The corresponding eigenvectors are

$$\left.\frac{dy}{d\theta}\right|_h = \frac{L}{2}\frac{(g_e + g_i) - \sqrt{(g_e - g_i)^2 + 4}}{(g_e g_i - 1)} \simeq 4.5 \times 10^4 \ \frac{\text{m}}{\text{rad}}, \tag{3.16a}$$

$$\left.\frac{dy}{d\theta}\right|_s = \frac{L}{2}\frac{(g_e + g_i) + \sqrt{(g_e - g_i)^2 + 4}}{(g_e g_i - 1)} \simeq -2.1 \times 10^3 \ \frac{\text{m}}{\text{rad}}. \tag{3.16b}$$

The numerical values are again evaluated with aLIGO g-factors. As pointed out in Ref. [23], for cavities with spot sizes $w_e \simeq w_i \gg \sqrt{L\lambda/\pi}$, the eigenvalues can be further simplified as

$$\left.\frac{dy}{d\theta}\right|_h \simeq \left(\frac{2\pi w_e w_i}{\lambda L}\right)^2 \frac{L}{2}, \tag{3.17a}$$

$$\left.\frac{dy}{d\theta}\right|_s \simeq -\frac{L}{2}. \tag{3.17b}$$

70

When we consider the full aLIGO interferometer, in addition to the hard/soft modes for each arm cavity, there are also the common/differential modes due to the Michelson nature. As a result, for the full interferometer there are four eigenmodes in total, corresponding respectively to the common/differential hard/soft modes. For the common hard mode, the eigenvalue is the same as that of the single arm's hard mode, while the eigenvector is $\boldsymbol{\theta}_{\mathrm{ch}}^{\mathrm{T}} = \left[\boldsymbol{\theta}_{\mathrm{xh}}^{\mathrm{T}}, \boldsymbol{\theta}_{\mathrm{yh}}^{\mathrm{T}}\right]$, where $\boldsymbol{\theta}_{\mathrm{x(y)h}}$ is the eigenvector of the X(Y)-arm's hard mode in the single arm basis. Similarly, for differential hard the eigenvector is $\boldsymbol{\theta}_{\mathrm{dh}}^{\mathrm{T}} = \left[\boldsymbol{\theta}_{\mathrm{xh}}^{\mathrm{T}}, -\boldsymbol{\theta}_{\mathrm{yh}}^{\mathrm{T}}\right]$. The common/differential soft eigenmodes can be obtained in similar manner.

Based on the diagram shown in Figure 3-6, we can define a radiation-pressure-modified suspension transfer function as

$$S_R = \frac{S_0}{1 + RS_0},\tag{3.18}$$

where S_0 is the free-pendulum transfer function, and R can be either $R_{\mathrm{h}} = (2P_{\mathrm{a}}/c)(\mathrm{d}y/\mathrm{d}\theta)_{\mathrm{h}} > 0$ for the hard mode, or $R_{\mathrm{s}} = (2P_{\mathrm{a}}/c)(\mathrm{d}y/\mathrm{d}\theta)_{\mathrm{s}} < 0$ for the soft mode. Note that for the hard mode, it is a negative feedback loop and therefore the radiation torque tends to stabilize the system. On the other hand, for the soft mode it is a positive feedback that tends to amplify the perturbations.

To proceed, we can consider a simple model of S_0 and see how it interacts with the radiation pressure effect. We can write

$$S_0(\omega) = \frac{1/(I\omega_0^2)}{1 - \omega^2/\omega_0^2},\tag{3.19}$$

where ω_0 is the natural frequency of the pendulum, and I is the moment of inertial. For aLIGO's test mass, the pitch torque to angle transfer function has $I = 0.61$ kg m^2 and $\omega_0/2\pi = 0.56$ Hz. The radiation-pressure-modified pendulum [equation (3.18)]

can thus be written as

$$
\begin{aligned}
S_R(\omega) &= \frac{S_0}{1 + RS_0} \\
&= \frac{1/\left[I(\omega_0^2 + R/I)\right]}{1 - \omega^2/\left(\omega_0^2 + R/I\right)} \\
&= \frac{1/(I\omega_R^2)}{1 - \omega^2/\omega_R^2},
\end{aligned}
\tag{3.20}
$$

where we have defined $\omega_R^2 = \omega_0^2 + R/I$ as the effective natural frequency of the pendulum. For future convenience we further define

$$
\omega_h^2 = \omega_0^2 + R_h/I, \text{ and}
\tag{3.21a}
$$

$$
\omega_s^2 = \omega_0^2 + R_s/I,
\tag{3.21b}
$$

for the hard and soft modes, respectively.

Thus the effect of radiation pressure is that it modifies the effective resonant frequency of the pendulum. Note that $R \propto P_a \propto P_{in}$ [cf. equation (1.17)]. We can thus plot ω_h and ω_s as a function of the input power as shown in Figure 3-7. To get the circulating power in the arms, we have assumed $g_p^2 = 42$ and $g_a^2 = 265$, and thus $P_a = 56 \times (P_{in}/10 \text{ W})$ kW.

First consider the soft mode, a significant feature is that ω_s^2 decreases as $P_a \propto P_{in}$ increases. When P_a reaches a critical value of $P_a = 0.55$ MW (or $P_{in} \simeq 98$ W at the current level of recycling gain), the resonant frequency $\omega_s^2 < 0$, or ω_s becomes imaginary. This means in the time-domain the motion will grow exponentially as $\exp(|\omega_s|t)$. As the targeted power circulating in the arms is $\simeq 0.7$ mW, this instability will eventually happen and will have to be stabilized by external control.

The instability can also be viewed as the following. Note that the radiation pressure forms a feedback loop, and consequently it is subject to the regular loop stability requirement $1 + RS_0 \neq 0$. However, at DC we have $S_0(0) = 1/(I\omega_0^2) > 0$ and $R_s < 0$. Consequently, for sufficiently large $|R_s|$ the instability threshold
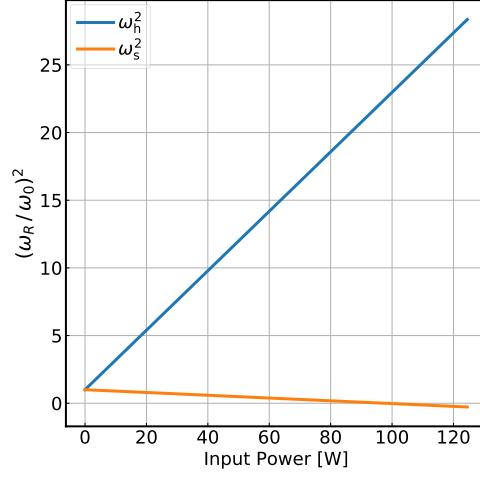
Figure 3-7: The square of the radiation-pressure-modified pendulum's resonant frequency as a function of input power.

$1 + R_\mathrm{s} S_0(0) = 0$ will eventually be satisfied. The critical $R_\mathrm{s,crit}$ is thus given by

$$R_\mathrm{s,crit} = -I\omega_0^2, \tag{3.22}$$

which is exactly the same as the R_s we would obtain by $\omega_\mathrm{s} = 0$ in equation (3.21b).

As for the hard mode, the radiation pressure shifts the pendulum resonance to a higher frequency than ω_0. Therefore it is always stable at DC. Nonetheless, *dynamically* even the hard mode will become nearly unstable. We can see this effect again by considering the loop instability criterion $1 + RS_0 = 0$. Note that at $\omega \gg \omega_0$, $S_0(\omega) \simeq -1/(I\omega^2) < 0$ while $R_\mathrm{h} > 0$. For sufficiently high radiation pressure feedback, the open-loop gain $R_\mathrm{h} S_0(\omega)$ will cross the unity gain with a phase of asymptotically $-\pi$. The critical frequency at which $1 + RS_0(\omega) \simeq 0$ happens is given by

$$\omega_\mathrm{h,crit}^2 \simeq R/I. \tag{3.23}$$

This is actually the same as the the shifted hard mode frequency in equation 3.21a (note that we have assumed $\omega_\mathrm{h} \gg \omega_0^2$). Thus external control will also be required to damped the hard mode motion at its shifted resonance.

The real aLIGO suspension is more complicated than the simple pendulum we have considered above. Nevertheless, the radiation-pressure-modified suspension transfer function can be straightforwardly obtained from equation (3.18), and the result is shown in Figure 3-8. We can see that the dynamics of the pendulum can be significantly modified due to the radiation pressure effect. Therefore it is critical to take it into account when we design the relevant control loops. In fact, the complicated shape of the current control filters for the hard modes (cf. Figure 3-4) is partially due to that it needs to maintain the system's stability over a range of $\sim 20-30$ W of different input powers. The price has to be paid for such a design is that it does not roll-off fast enough to meet the aLIGO noise requirement in the $10-30$ Hz band.

(a) Hard mode. (b) Soft mode.
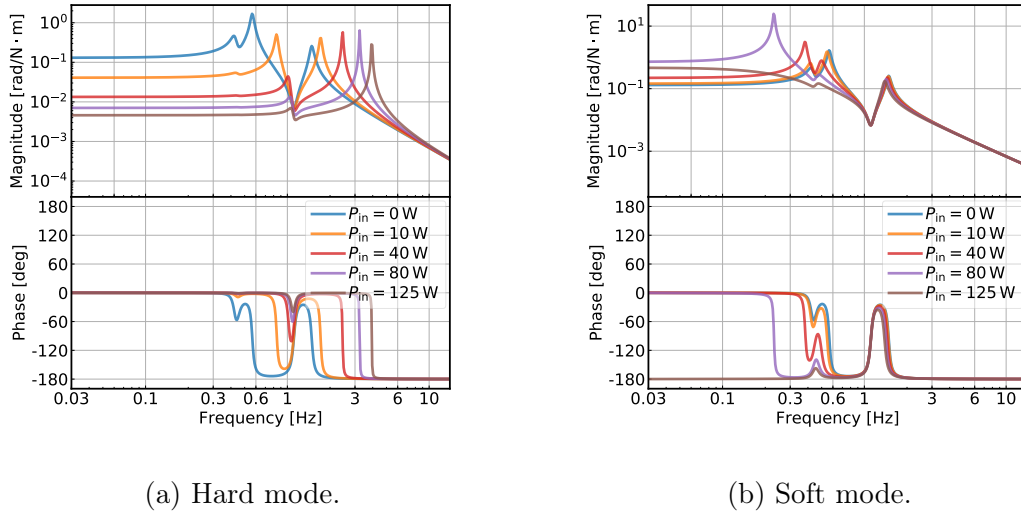
Figure 3-8: The radiation-torque-modified pendulum transfer functions for the pitch degree of freedom at different levels of input power.

As an aside, we point out that while our discussion above focuses on the test mass (which is the bottom stage of the quadruple suspension chain [28]), the radiation pressure will modify the other stages in a similar manner. For example, consider the transfer function from a torque drive at the penultimate stage to an angular response at the test-mass stage. If we define the free-pendulum transfer function to be $S_0^{(\mathrm{pum})}$, then the radiation pressure will modify it as $S_R^{(\mathrm{pum})} = S_0^{(\mathrm{pum})}/(1 + R S_0)$. Note that in the denominator the S_0 is still the torque-to-angle transfer function at the test-mass

74

stage (instead of the penultimate stage) as the radiation pressure feedback happens there. In general, the transfer function of torque drive at any point of the suspension to the angular response of the test mass will be modified by the factor of $1/(1+RS_0)$ due to the radiation pressure effect.

3.3.2 Loop dynamics

In this Section, we consider how we can modify the dynamics by adding an external control K to the system[5].
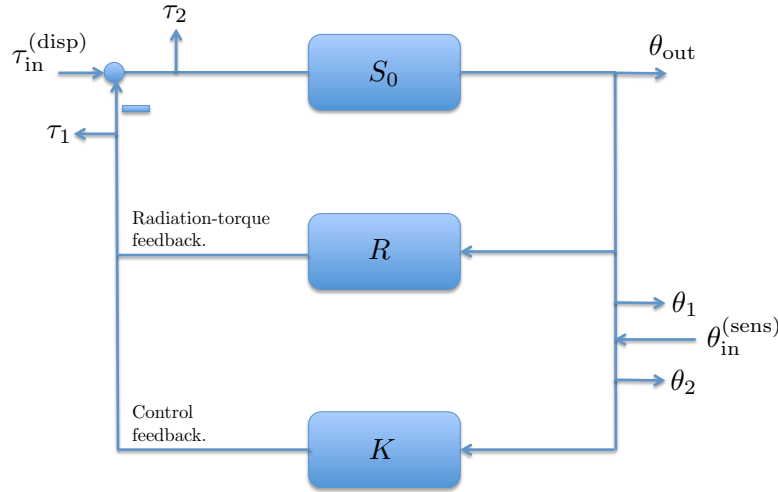
Figure 3-9: The signal flow diagram in the presence of both radiation-torque and digital control.

Now the signal flow can be modeled as the loop diagram as shown in Figure 3-9. First we can consider how the sensing noise $\theta_{in}^{(sens)}$ propagates in the loop[6]. It is

---

[5]Note that the spot-position motion causing the radiation torque is measured with respect to the mirror. Therefore they should be sensed as "pointing" degrees of freedom with, e.g., DC QPDs. Nevertheless, up to order unity corrections due to the Guoy phase propagation, the fluctuation in the arm cavity's axis will cause a spot-position motion on the test masses $\sim 1/(1 - r_i) \simeq g_a^2/2$, or more than 100 times greater than that caused by perturbations in the recycling-cavity's axis. Therefore in practice we can treat the recycling-cavity's axis as being static and use a WFS signal to control the radiation-pressure effects. For example, we use a single control loop for the differential-hard mode sensed with the AS_A_RF45_Q WFS signal to simultaneously maximize the interferometric buildup and damp the radiation pressure effects.

[6]The sensing noise happens at the detection PD. It thus enters after the radiation-torque feedback that is inside the cavity. There will be quantum 01/10 entering the arm cavity and create "quantum-radiation-torque noise", similar to the QRPN. This is nonetheless a small effect because, unlike the

straightforward to show that the closed-loop output can be written as

$$\theta_{\text{out}}^{(\text{sens})} = \frac{-S_0 K}{1 + S_0\,(R + K)}\theta_{\text{in}}^{(\text{sens})}, \tag{3.24}$$

which, by substituting in $S_R = S_0/(1 + S_0 K)$, can be further written as

$$\theta_{\text{out}}^{(\text{sens})} = \frac{-S_R K}{1 + K S_R}\theta_{\text{in}}^{(\text{sens})}. \tag{3.25}$$

Meanwhile, the open-loop transfer function G_{ol} is given by

$$G_{\text{ol}} \equiv \frac{-\theta_1}{\theta_2} = K S_R. \tag{3.26}$$

Note that this is same open-loop transfer function we would measure (e.g., the one shown in Figure 3-4a) by exciting the error point of the control loop and then measure the ratio between the points right before and right after the excitation.

Specifically, equations (3.25) and (3.26) suggest that for the sensing noise we can first combine the free pendulum S_0 and radiation pressure feedback R into single system S_R, and then directly consider the interaction between the controller K and S_R.

How about the displacement noise then? Similarly, we can show that the closed loop torque to angle transfer function can be written as

$$\begin{aligned}
\theta_{\text{out}}^{(\text{disp})} &= \frac{S_0}{1 + S_0\,(R + K)}\tau_{\text{in}}^{(\text{disp})} \\
&= \frac{S_R}{1 + K S_R}\tau_{\text{in}}^{(\text{disp})} = \frac{S_R}{1 + G_{\text{ol}}}\tau_{\text{in}}^{(\text{disp})}.
\end{aligned} \tag{3.27}$$

Once again, we can see that by using the modified suspension transfer function we obtain the correct closed-loop torque-to-angle response.

However, subtlety comes in when we consider the open-loop gain as seen by the

---

quantum 00 mode that is resonant in the arm cavity, the quantum 01/10 modes are off resonance and do not get the amplification due to cavity buildup. We thus ignore this effect in our discussion.

torque disturbance,

$$G'_{\rm ol} \equiv \frac{\tau_1}{\tau_2} = S_0(R + K) \neq S_R K. \tag{3.28}$$

Therefore, when consider the residual closed-loop displacement noise in angle (cf. Figure 3-5), we should use the input torque noise (cf. the right panel of Figure 3-1) multiplied by equation (3.25), with the free-pendulum transfer function replaced by the radiation-torque-modified one. If instead we want to treat the input displacement noise in angle as a constant as $S_0 \tau_{\rm in}^{\rm (disp)}$, we have implicitly treated the pendulum as unchanged. As a result we need to separately consider the radiation pressure feedback, and in this picture the proper closed-loop noise is given by $S_0 \tau_{\rm in}^{\rm (disp)} / [1 + S_0(R + K)] = S_0 \tau_{\rm in}^{\rm (disp)} / (1 + G'_{\rm ol})$.

3.3.3 Compensating for the Sidles-Sigg effect

From the discussion above we can see that to stabilize the system in the presence of Sidles-Sigg radiation torque, one can design different control filters such that at each input power level, the transfer function $S_R/(1 + K S_R)$ is stable. This, however, can be both challenging and time-consuming, as S_R depends sensitively on power (Figure 3-8) and will thus require many different filters to be tuned individually. If one instead make a filter that is stable over a relatively large span of input power, then it is hard to keep to filter to be optimal at the same time. For example, the current control filter used at the LIGO Hanford site (cf. Figure 3-4) is stable for an input power ranging from 0 to ~ 20 W. However, this controller is not optimal as it suppresses the input displacement more than required yet does not have a fast enough high-frequency roll-off.

Nevertheless, a simple solution to tackle the Sidles-Sigg effect exists. Note that $R = (2P_{\rm a}/c)\,(\mathrm{d}y/\mathrm{d}\theta)$ is a frequency-independent quantity that depends only on the cavity geometry (i.e., the g-factors) and the power circulating in the arms. The former was carefully measured with high accuracy prior the installation of aLIGO, and the latter can be measured in real time via, e.g., the PDs on the transmission of the ETMs. Moreover, we also know the suspension transfer function S_0 and can infer the

angular motion θ_{out} from the alignment sensing systems. In other words, we know every single component of the radiation pressure torque. Consequently, we can create a new path in the digital control system with a loop gain of $-RS_0$ that cancels out the Sidles-Sigg torque RS_0. With this scheme, when changing the power circulating in the arms, we only need to change the DC gain of this radiation compensation path accordingly, and the suspension will stay as a power-independent free pendulum. As a result, we only need to design a single control filter K that optimally stabilizes the system, and this filter will stay valid over at least a large range of, if not any, input power levels.
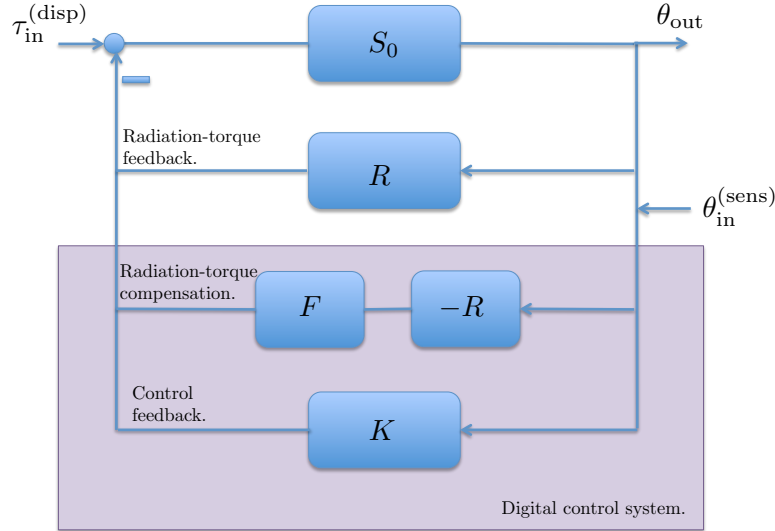
Figure 3-10: The diagram illustrating the compensation scheme for the Sidles-Sigg radiation torque.

The scheme is illustrated in the diagram shown in Figure 3-10. While ideally we would just put a $-R$ in the compensation path, in reality we want to add some gain-adjustment factor F in the path. This is because when we compensate for the hard mode, we need to send in to the suspension a digital torque corresponding to the soft mode. If over-compensation accidentally happens, we will destabilize the system with the digital soft mode we create. To avoid such a situation, we deliberately

under-compensate for the hard mode by making $F < 1$. Specifically, we can define

$$S'_R = \frac{S_0}{1 + (1 - F)RS_0}.$$ (3.29)

When $F = 1$, we have $S'_(R) = S_0$ the free pendulum transfer function, which is what we do for the soft modes. On the other hand, we set $F = (P_{\text{in}} - 10\text{ W})/P_{\text{in}}$, which makes $S'_h = S_h(10\text{ W})$. In other words, the suspension transfer function will always look like a hard-mode pendulum at an input power of 10 W, and small errors in the compensation path will not turn it into a destabilizing soft mode. Another usage of F is to provide extra cut-off at high frequency. Since we feedforward the same error signal used in the regular control path to the compensation path, we will inject the same sensing noise as well. Therefore, when $|RS_0| \ll 1$, we will low-pass the digital torque signal to reduce the excess sensing noise.

In aLIGO, the conceptual design in Figure 3-10 can be implemented in the diagram shown in Figure 3-11. In aLIGO, the angular control is actuated with the penultimate stage (PUM) instead of the test-mass stage (TST), as the it has a larger actuation range. Therefore we need to digitally invert the suspension transfer function to make it looks like the test-mass stage. This is accomplished by the filter $S_0^{(\text{tst})}/S_0^{(\text{pum})}$. Note that this is the only frequency-dependent part in the compensation scheme (except for the high-frequency cut-off filter), and it requires only the free-pendulum transfer functions that can be measured accurately at the observatories [29]. The other quantities are all DC calibration factors. The mirror's angular motion in radiants is converted to the digital counts by G_{opt}, and the digital counts are further converted into actuation torque by G_{act}. As a result, once $S_0^{(\text{tst})}/S_0^{(\text{pum})}$ is measured, we only need to adjust the DC gain of the compensation path which is $\propto P_{\text{a}}$. This is a much easier way of tackling the Sidles-Sigg effect than designing different frequency-dependent control filters at different power levels.

This compensation scheme has been tested out at both the Hanford the Livingston observatories [30, 31], and we summarize the results in Figure 3-12. In the plot we show with red pluses the measured open-loop transfer functions KS'_R at an input
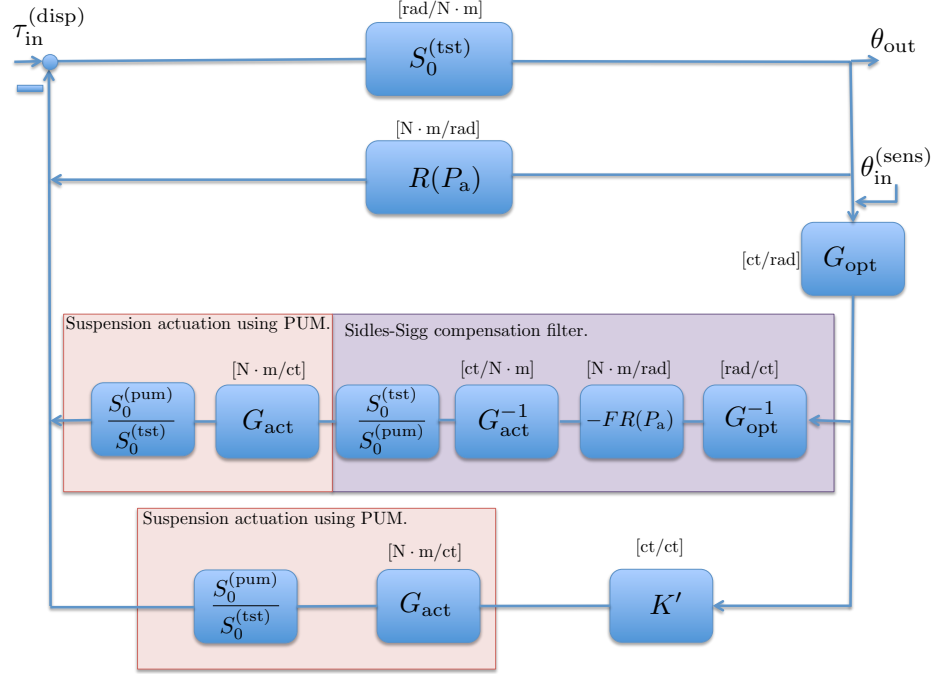
Figure 3-11: The implementation of the compensation scheme for the Sidles-Sigg effect in aLIGO. We have kept the representation of the radiation torque feedback the same as in Figure **??** for easy comparison. We label $S_0 = S_0^{(\mathrm{tst})}$ the free-pendulum transfer function at the test-mass stage explicitly label with a "tst" to distinguish it from the penultimate-stage transfer function $S_0^{(\mathrm{pum})}$. The quantities G_{opt} and G_{act} are respectively the DC optical response and the actuation gain. The K' is the dimensionless digital control filter that is related to the total control filter $K = G_{\mathrm{opt}} G_{\mathrm{act}} K' S_0^{(\mathrm{pum})} / S_0^{(\mathrm{tst})}$.

(a) Differential-hard mode in pitch.　　　　(b) Common-hard mode in yaw.
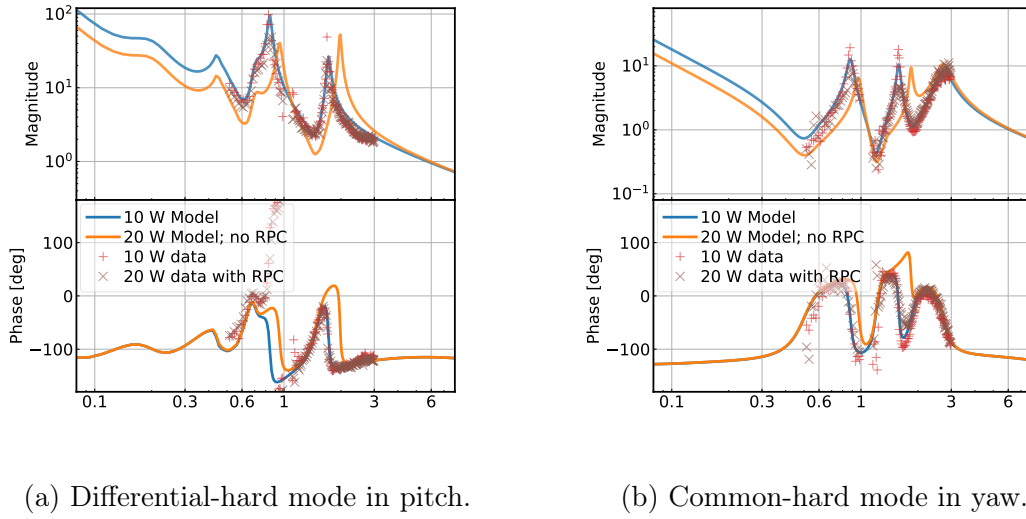
Figure 3-12: The modeled and measured open-loop transfer functions of the hard loops. Using the radiation pressure compensation (RPC) technique, the transfer functions measured at an input power of 20 W (brown-crosses) are essentially identical to the ones measured at 10 W (red-pluses), and match well to the model (blue trace). As a comparison, we also show in the orange trace how the transfer function would look like if we do not compensate for the radiation pressure torque.

power of 10 W, and with brown crosses the transfer functions measured at 20 W and with the radiation-pressure compensation on to keep the suspension plant the same as the 10 W one. We can see that the two measurements match well to each other, and they both show good agreement with the modeled open-loop transfer function at 10 W that is shown in the blue traces[7].As a comparison, in the orange traces we also present the open-loop transfer function at 20 W without radiation-pressure compensation in the orange trace. As indicated by the plots, our compensation technique works well and it successfully removes the radiation-induced power dependence in the suspension transfer function. This further implies that in the future we only need to optimize for a single control K. The variations in the arm power P_a will be taken care of by the compensation path $-FR$ that requires only requires only DC gain adjustments.

---

[7]In the open-loop transfer function of the pitch degree of freedom there exists some phase mismatch between the measurement and the model. This is likely due to sensing and actuation cross-couplings in the real system as suggested by Ref. [32]. Also note that the open-loop transfer functions shown in Figure 3-12 are measured in the "high-bandwidth" configuration, which has about factor of 2 higher DC gain than the one shown Figure 3-4. The high-bandwidth filters also does not have the extra high-frequency cut-offs.

This will greatly simplify the commissioning of the alignment control at high-power operations.

3.3.4 Sensing noise from the compensation path.

As mentioned above, the compensation path will be subject to the same sensing noise as the regular control loop. The total closed-loop sensing noise is

$$\theta_{\text{out}}^{\text{(sens)}} = \frac{-KS_R' + FRS_R'}{1 + KS_R'}\theta_{\text{in}}^{\text{(sens)}}. \tag{3.30}$$

In the numerator, the KS_R' term is the coupling due to the regular feedback control, and the FRS_R' term is the contribution from the radiation compensation path. To avoid this noise contaminating the GW readout, we introduce extra high-frequency cut-off filters in F. We choose the filter to maximize the roll-off above 10 Hz while keep its phase delay at 3 Hz less than $10°$. In Figure 3-13 we show the quantity FRS_R' at different input power levels (the different dotted lines) and compare it with KS_R' (the black trace). We can see that the sensing noise contribution from the radiation-pressure compensation path is always much less than that from the regular control feedback in the $10 - 20$ Hz band. Moreover, with the current low-path filters, the compensation path also meets aLIGO's requirement on the noise roll-off (assuming $\theta_{\text{in}}^{\text{(sens)}} = 10^{-14}$ rad$/\sqrt{\text{Hz}}$ and 1 mm/rad of angular noise coupling) up to $\simeq 70$ W of input power.

3.3.5 Error tolerance

While we have demonstrated that the radiation-torque compensation technique works in aLIGO with real data in Section 3.3.3, it is also critical to know how much error can be tolerate in this scheme. Thus we investigate its robustness in this Section using the small-gain theorem [?].

Consider a simple model shown in the left panel of Figure 3-14. Here H is the system whose stability robustness is under investigation and Δ_H represents an uncertainty of the dynamics of the system. Such a system is also known as the basic
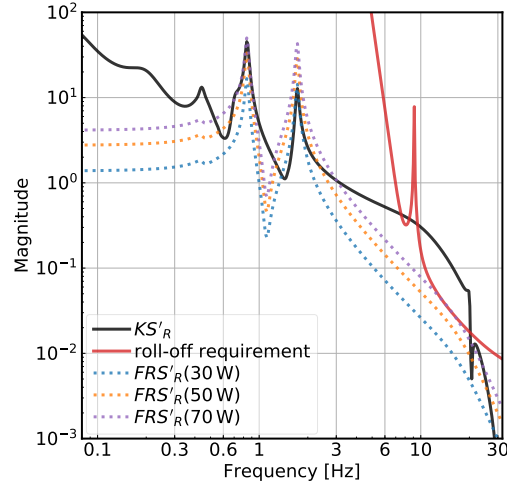
Figure 3-13: Comparison between FRS'_R (the dotted lines) and KS'_R (the black-solid line). At above 3 Hz, these curves represents the roll-off of the sensing noise. The sensing noise contribution from the radiation-pressure-compensation path ($\propto FRS'_R$) is always much less than that from the regular control feedback ($\propto KS'_R$), and it meets aLIGO's requirement on the cut-off of the sensing noise up to an input power of 70 W.
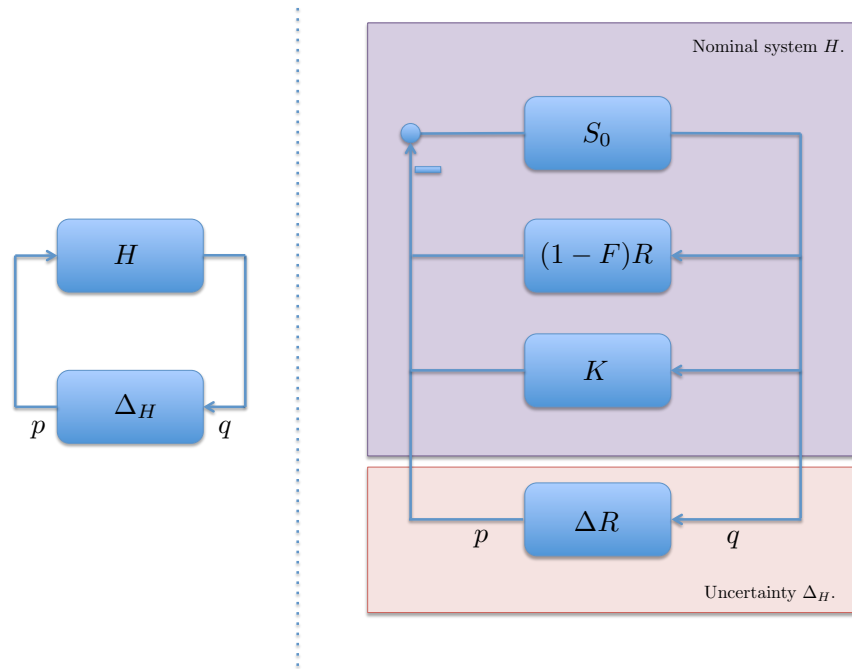
Figure 3-14: Left: the basic perturbation model. Right: Applying the basic perturbation model to the radiation pressure compensation system.

83

perturbation model. The small-gain theorem states that if both H and Δ_H are stable, then a *sufficient* condition for internal stability of the basic perturbation model is

$$||\Delta_H||_\infty < \frac{1}{||H||_\infty}, \tag{3.31}$$

where ∞-norm of H is given by

$$||H||_\infty = \sup_{\omega \in \mathbb{R}} \overline{\sigma}\left[H(\mathrm{i}\omega)\right]. \tag{3.32}$$

Here $\overline{\sigma}$ denotes the largest singular value. For a (proper and stable) single-input-single-output system, the infinity norm is simply the largest value of the frequency response magnitude.

The small-gain theorem can be applied to our case as illustrated in the right panel of Figure 3-14. We can combine our nominal system as the function H, which leads to

$$H \equiv \frac{q}{p} = -\frac{S_R'}{1 + K S_R'}. \tag{3.33}$$

The the sufficient condition for the loop to be stable in the presence of perturbation ΔR can be written as

$$\left|\frac{\Delta R}{R}\right| < \left|\frac{1 + K S_R'}{R S_R'}\right| \propto \frac{1}{P_\mathrm{a}}. \tag{3.34}$$

The bound in equation (3.34) is valid for any perturbation ΔR as long as ΔR is stable by itself. Here we consider two types that are most likely to occur in the system[8]. To proceed, we first write $F = F_0 F_\mathrm{lp}$, where $F_0 \lesssim 1$ is the overall DC gain and F_lp carries the low-pass filter whose DC gain is set to unity. For simplicity we can set our nominal compensation gain such that $F = F_0 = (P_\mathrm{in} - 10\ \mathrm{W})/P_\mathrm{in}$. The first type is then the error in the DC gain of the compensation path, which may be caused by fluctuations in the arm power. We can model it as $\Delta R / R = \Delta F$, where

---

[8]The small-gain theorem is actually more suited to study *unstructured* uncertainties than the structured ones we will consider here, as for a structured uncertainty it provides only the *sufficient* stability condition, which is in general more contingent than the real stability requirement. Nonetheless, as we will see, even such strict conditions can be satisfied with the uncertainty levels typical for aLIGO.

ΔF is a DC constant accounting for the gain mismatch. The second type is due to that we have ignored the extra low-pass F_{lp} in the "nominal" compensation path (this is actually an error that will always happen by our construction and should thus be added with other perturbations). Due to causality constraints the cut-off filter will introduce phase delay in the subtraction band which makes our compensation imperfect. This effect can be modeled by noting $FR = F_0 R - (1 - F_{\text{lp}})F_0 R$, which leads to $\Delta R/R = (1 - F_{\text{lp}})F_0 \lesssim (1 - F_{\text{lp}})$.

The tolerance to each type of uncertainties is shown in Figure 3-15. Here we evaluate it at an input power of 40 W, or about 0.23 MW of power circulating in each arm. This is the typical power level aLIGO will operate at for the third observing run. Note that while our compensation scheme keeps the suspension independent of power, the error tolerance decreases linearly with power [cf. equation (3.34)]. Nevertheless, the stability margin is sufficiently large. At 40 W of input power, the tolerance on the DC-gain mismatch can be as large as 40%. Even if the power increased by a factor of 3 to reach aLIGO's designed operation level, the tolerance is still more than 10%. This is still much greater than the typical power fluctuations in the arm cavity due to alignment fluctuations (cf. Figure 3-2). Moreover, the long-term (on timescale of a few hours) drift in power and optical sensing gain can be easily measured in real time and feedback to the DC gain of the compensation path, making it even more robust to this type of perturbations. Meanwhile, the error due to the low-pass filter's phase delay is also more than a factor of 3 below the error tolerance, and will thus not cause instabilities in the loop.

3.4   The $\mathrm{d}P/\mathrm{d}\theta$ effect

So far we have been focused on the Sidles-Sigg effect: a mirror's angular motion perturbs the spot position on the mirror, which creates a torque that may lead to either more or less angular motion depending on the phase of the feedback. This process corresponds to the first term in equation (3.9). Meanwhile, the second term in equation (3.9) indicates another potential feedback channel. If a mirror's angular
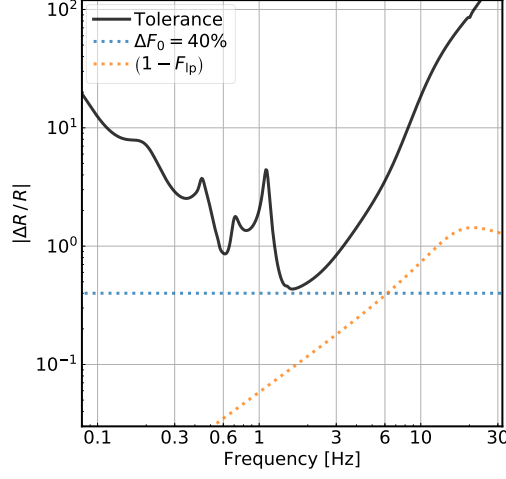
Figure 3-15: The error tolerance on $|\Delta R/R|$ in the radiation compensation path. If a perturbation is below the black trace (evaluated at $P_{\text{in}} = 40$ W), it satisfies the *sufficient* condition for stability. The controller we use currently can tolerate at least 40% error in the DC gain in the compensation path (shown in the blue trace). The phase delay due to the high-frequency cut-off filter is also well-below the error tolerance and thus affect the stability of the loop.

motion perturbs the circulating power, then the radiation force may couple with the DC spot mis-centering on the mirror to create a torque feedback as well. Moreover, in addition to the DC spot mis-centering, the radiation force can also push the mirror in length, which may also close the feedback loop via the length-to-pitch cross-coupling in the suspension. In fact, the suspension length-to-pitch coupling is much greater than that due to the spot mis-centering in aLIGO and we will consider only this path. It also means that effect is most relevant for the pitch degree of freedom as there exists no direct length-to-yaw coupling in the suspension. In this Section, we will refer to this feedback channel due to power fluctuations as the $\mathrm{d}P/\mathrm{d}\theta$ channel whose diagram is shown in Figure 3-16, and discuss its significance. As we will see, this is the main factor determines the design of the soft loops.

In principle, the feedback gain due to the $\mathrm{d}P/\mathrm{d}\theta$ is much smaller compared to that from the Sidles-Sigg effect. This is because in an ideal cavity small misalignment will only create power fluctuations in the quadratic order. However, during aLIGO's second observing run, both observatories saw growing oscillations at $0.4 - 0.6$ Hz
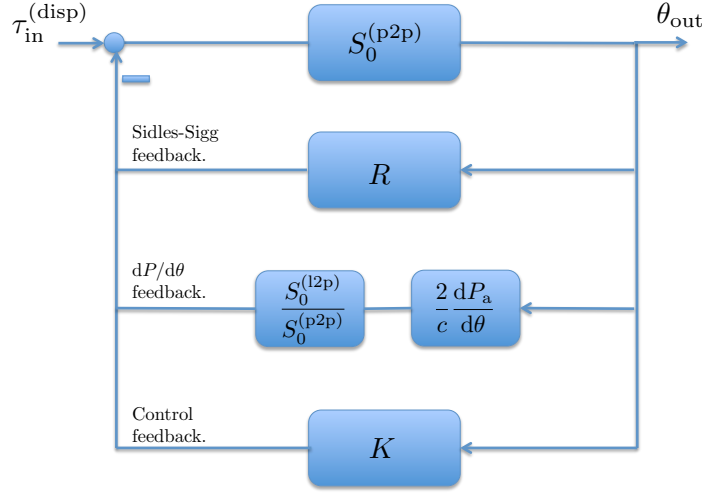
Figure 3-16: The diagram illustrating the $dP/d\theta$ radiation pressure feedback.

exclusively in pitch in the common-soft mode when the circulating power in the arms reaches $P_a \simeq 160$ kW. Here we present a model that may explain this oscillation. We can define

$$G_{\text{spot}}(f) = R_s S_0^{(\text{p2p})}(f) = \frac{2P_a}{c} \frac{dy}{d\theta}\bigg|_s S_0^{(\text{p2p})}(f), \qquad (3.35)$$

as the feedback gain due to the Sidles-Sigg effect for the soft mode. To distinguish the torque-to-angle transfer function from the length-to-pitch one, we label the former explicitly with a superscript "p2p" as $S_0 = S_0^{(\text{p2p})}$, while for the latter we define it as $S_0^{(\text{l2p})}$. At the same time, the $dP/d\theta$ effect creates a feedback gain in the soft loop as[9]

$$G_{\text{power}}(f) = \frac{2P_a(0)}{c} \frac{d\left[P_a(f)/P_a(0)\right]}{d\theta} S_0^{(\text{l2p})}(f). \qquad (3.36)$$

To have a non-vanishing $dP/d\theta$ term, we introduce small alignment offset at DC of

---

[9]Strictly speaking, the radiation force will create an angle $\propto [-1, 1]$ in the $[\delta\theta_e, \delta\theta_i]$ basis, which does not correspond exactly to the soft mode $[-\bar{g}, 1]$. Nevertheless, since $\bar{g} \simeq 0.87 \sim 1$ and other uncertainties of similar or greater level exist in the model, we will ignore this effect for simplicity.

$\mathcal{O}(1)$ nrad in the common-soft loop[10]. This leads to

$$\frac{\mathrm{d}\,[P_a/P_a(0)]}{\mathrm{d}\theta}(f) \simeq \frac{6 \times 10^3}{1 + \mathrm{i}f/f_c} \times \left(\frac{\Delta\theta_{\mathrm{cs}}}{1\ \mathrm{nrad}}\right), \qquad (3.37)$$

for aLIGO in the second observing run with a power-recycling gain of $r_{\mathrm{p}}^2 = 32$ and a CARM-cavity pole of $f_c = 0.7$ Hz. Here $\Delta\theta_{\mathrm{cs}}$ is the DC offset in the common-soft loop and it can be either positive or negative. When this effect was first observed, both sites had only low-bandwidth (~ 10 mHz) control on soft modes to control the DC spot pointing on the test masses, and therefore we ignore the control filters when considering the loop stability. Consequently, the total open-loop gain can be written as $(G_{\mathrm{spot}} + G_{\mathrm{power}})$, and the system becomes unstable if $(G_{\mathrm{spot}} + G_{\mathrm{power}}) = 1$.

(a) $\Delta\theta_{\mathrm{cs}} = -1.7$ nrad. $\qquad\qquad$ (b) $\Delta\theta_{\mathrm{cs}} = 12.5$ nrad.
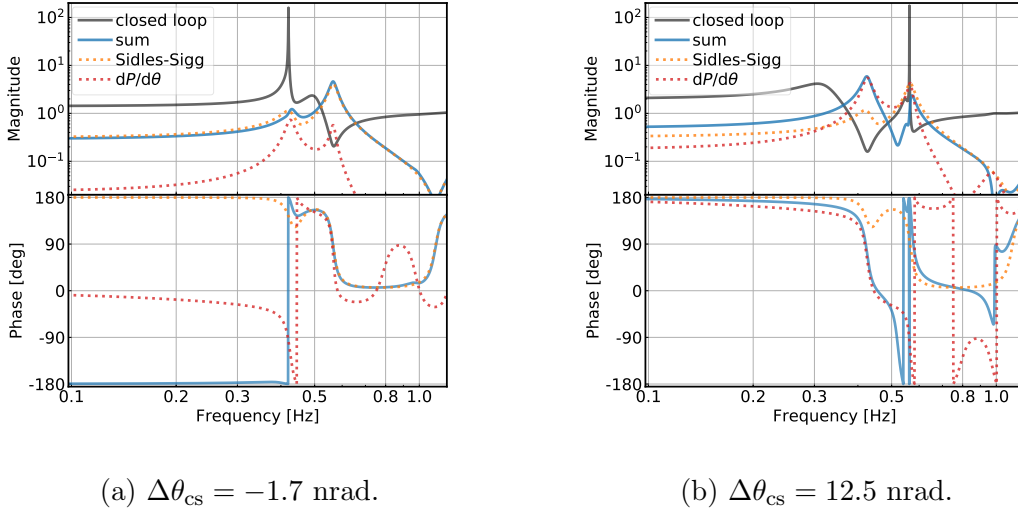
Figure 3-17: Two scenarios that the $\mathrm{d}P/\mathrm{d}\theta$ effect may lead to the observed instabilities in the $0.4 - 0.6$ Hz band. In each plot we use the blue trace to indicate the open-loop gain and the black trace the closed-loop response. The contributions from the Sidles-Sigg effect and the $\mathrm{d}P/\mathrm{d}\theta$ effect are represented respectively with the orange- and the red-dotted lines.

In Figure 3-17 we present two possibilities that the $\mathrm{d}P/\mathrm{d}\theta$ channel could produce the observed instabilities at $0.4 - 0.6$ Hz with a circulating power of $P_{\mathrm{a}} \simeq 160$ kW. In the left panel we let the DC offset in the common-soft loop to be -1.7 nrad. Without

---

[10]This is not the unique mechanism to have linear angle-to-power coupling. For example, if the scattering loss at the test masses varies with spot location, this could also lead to linear coupling.

the $\mathrm{d}P/\mathrm{d}\theta$ effect, the Sidles-Sigg feedback cross the unity gain at around 0.4 Hz with a small phase margin. This corresponds to the shift in the resonant frequency of the radiation-torque modified plant as shown in the right panel of Figure 3-8, and the resultant gain peaking is $\lesssim 10$, comparable to the quality factor of the original suspension resonance . The $\mathrm{d}P/\mathrm{d}\theta$ effect, while much smaller effect elsewhere, is comparable to the Sidles-Sigg effect at the suspension resonance ~ 0.5 Hz. This decreases the phase margin and eventually leads to an instability in the loop at 0.4 Hz. Another possibility is illustrated in the right panel of Figure 3-17. In this case we introduce a DC offset of $\Delta\theta = 12.5$ nrad. This makes the $\mathrm{d}P/\mathrm{d}\theta$ effect roughly equals to the Sidles-Sigg effect in amplitude around the suspension resonances. However, the two effects can be out of phase and thus lead to extra unity-gain crossings with fast-evolving phase. As a result, we once again see an instability develops in the system at 0.6 Hz.

Note that the instabilities in the above examples happen at a circulating power of $\simeq 160$ kW, much smaller than the critical power $\simeq 550$ kW for the soft mode to become unstable due to the Sidles-Sigg effect alone (cf. Section 3.3). This indicates the necessity of having a relatively high-bandwidth $[\mathcal{O}(1)$ Hz] external control on the soft loop even at an input power of ~ 30 W. However, before realizing this $\mathrm{d}P/\mathrm{d}\theta$ effect, the soft mode was controlled with the dithering loop that could support only mHz to 10 mHz bandwidth because of limited sensitivity (cf. Sections 2.3.2 and 2.4). To circumvent this, we utilize a signal-blending technique. At AC ($\gtrsim 0.01 Hz$) frequencies, we use a combination of DC QPDs on the transmission of ETMs to sense the soft mode motion[11]. This error signal is used for both compensating for the Sidles-Sigg effect (Section 3.3.3) and damping of the residual $\mathrm{d}P/\mathrm{d}\theta$ radiation torque and/or other unmodeled perturbations. To avoid the long-term drift of the QPDs with respect to the arm cavity at timescales of $\gtrsim 1$ hr, the damping loop is

---

[11]Note that the "soft mode" here measures the test masses with respect to the ground and it needs to be sensed as a pointing degree of freedom. There is also an "interferometric soft mode", which measures the translational shift of the arm cavity's axis with respect to the power-recycling-cavity's axis. This is the $\Delta\theta_{\mathrm{cs}}$ we need in order to have linear angle-to-power coupling. As discussed in Section 2.4, this interferometric degree of freedom is controlled with PR2 and thus cannot damp the radiation torques.

flat below 0.1 Hz. On the other hand, the dithering loop that is a simple integrator with $1/f$ slope and it takes over the control below about 10 mHz to fix the spot on the ETM at DC. The control loop is presented in the left panel of Figure 3-18.

(a) Open-loop transfer function.

(b) Error tolerance.
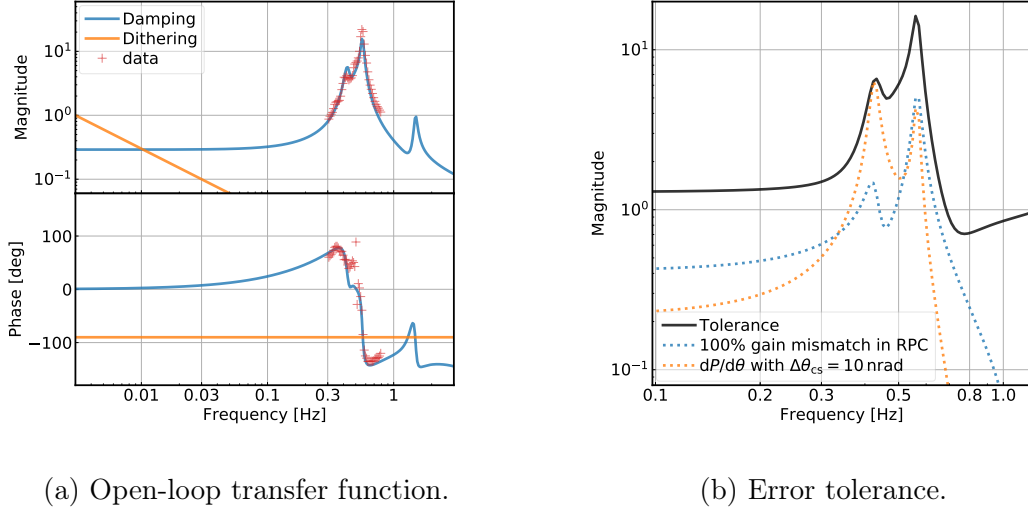
Figure 3-18: Left: the open-loop transfer function for controlling the soft-mode in pitch. The blue trace uses error signal from DC QPDs to damp the $\mathrm{d}P/\mathrm{d}\theta$ radiation torque. The same error signal is also used to compensate for the Sidles-Sigg effect, which removes the power dependence of the suspension pendulum. The orange trace indicates the dithering control that locks the DC spot position on the ETM to a fixed location. Right: error-tolerance of the soft-mode controller. If a perturbation creates feedback gain whose peak magnitude is below the black trace, it satisfies the *sufficient* condition for the system to maintain internal stability.

Once we specify the controller, we can derive its error tolerance using the small-gain theorem. This result is shown in the right panel of Figure 3-18. Note that this time we show the tolerance on the total feedback gain instead of that on a certain parameter as we have done in Figure 3-15. For example, we show the feedback gain due to 100% gain mismatch in the radiation pressure compensation path for the soft mode in the blue-dotted line, and the feedback gain due to the $\mathrm{d}P/\mathrm{d}\theta$ effect with 10 nrad offset in the ("interferometric") soft loops at DC. All the values are evaluated at an input power of 40 W, or $P_{\mathrm{a}} \simeq 0.23$ MW. With the damping loop engaged, neither of them will cause instabilities any more. The high-bandwidth soft-mode control is thus a crucial step towards aLIGO's high-power operation.

3.5 Noise reduction techniques

Having discussed the effects of radiation pressure torques extensively in the previous three Sections, we now return to the noise considerations mentioned at the beginning of this Chapter, and discuss in this Section techniques to further reduce the noise in the alignment systems.

3.5.1 Length-to-pitch feedforward

As shown in Figure 3-1 the displacement noise is dominated by the seismic motion (the blue trace). As the ground move longitudinally, it will also cause the mirror to move in the pitch direction. For a simple pendulum, this transfer function can be written as (we will ignore the damping terms for simplicity; see Ref. [18])

$$\frac{\theta}{x} \equiv H_\theta(\omega) \simeq \frac{\omega_\theta^2}{l+b} \frac{\omega^2}{\left(-\omega^2 + \omega_1^2\right)\left(-\omega^2 + \omega_2^2\right)}, \qquad (3.38)$$

where x is the longitudinal motion of the ground and θ the mirror's motion in pitch. We use l and b to represent respectively the length of the pendulum suspension, and the distance between the binding point and the mirror's center of mass. We will further write the mirror's mass and moment of inertia as m and I. The frequencies of the resonances $\omega_{1,2}$ are thus given by

$$\omega_{1,2}^2 = \frac{g}{2lI}\left[I_\theta + mb(l+b) \mp \sqrt{[I - mb(l+b)]^2 + 4mb^2I}\right], \qquad (3.39a)$$

$$\omega_1 \simeq \omega_\theta \simeq \frac{mgb}{I}, \qquad \omega_2 \simeq \omega_x = \frac{g}{l}, \qquad (3.39b)$$

where in the second line we have assumed $b \ll l$ and expanded the quantities to first order in b/l. Since the ground's motion x can be readout from seismometers [15] and its coupling to pitch is known both theoretically and can be measured in situ. at the observatories, it means that we can *predict* the angular motion of the mirrors and thus feedforward the signal to cancel the mirror's displacement [?].

While we can also stabilize the motion using feedback controls, the feedforward

subtraction has its unique advantages. This is because the feedback control is subject to loop stability requirements, which limits the high-frequency sensing noise roll-off to be at most $1/f^2$ around the unity-gain frequency. On the other hand, the feedforward subtraction is always stable (as long as the filter itself is stable) and can be cut off much faster. Such a property is especially valuable for the alignment system because currently the sub-30 Hz sensitivity of aLIGO is limited by the residual angular sensing noise from these 3-Hz-bandwidth feedback loops [21]. If we instead stabilize the mirror's motion with feedforward subtraction, the required bandwidth of the feedback loops can thus be reduced[12], thereby improving the low-frequency sensitivity of ground-based GW detectors.

This effort has been carried out at both observatories [?, ?, ?]. We first excite the suspension point of each test mass in length and measure its angular response with optical levers [?], which allows us to estimate the length-to-angle transfer function $H_\theta(\omega)$[13]. We then send the signal $-H_\theta(\omega)x$ to cancel the seismically induced motion $H_\theta(\omega)x$.

The performance of the feedforward subtraction is shown in Figure 3-19. Here we actively excite the longitudinal motion of suspension point. The blue-solid trace is the pitch motion of the test mass measured locally with optical levers, and the blue-dashed line is its cumulative rms value. As we enable the feedforward cancellation, the displacement is dramatically reduced to the orange trace. In terms of power, we reduced the motion by about 80% with the feedforward cancellation.

More importantly, we can examine the benefits of feedforward with global alignment signals. This is illustrated in Figure 3-20. In the plots the blue traces are the input displacement noises measured in the differential- and common-hard modes in pitch (corresponding to the left and right panels, respectively) without the feedfor-

---

[12]Actually, currently the bandwidth of angular feedback control is limited by the requirement of stabilizing radiation pressure effects instead of suppressing the residual seismic motion. Nonetheless, with the compensation of the Sidles-Sigg effect we have shown that we can remove the variation in the suspension transfer functions. This would make the suppression of seismic motion again the main factor determining the control bandwidth. This will also be the case for future GW detectors with more massive test masses than aLIGO as the significance of radiation torque is naturally mitigated by the increased moment of inertia.

[13]The transfer functions are fitted using `https://iirrational.readthedocs.io/en/latest/`.
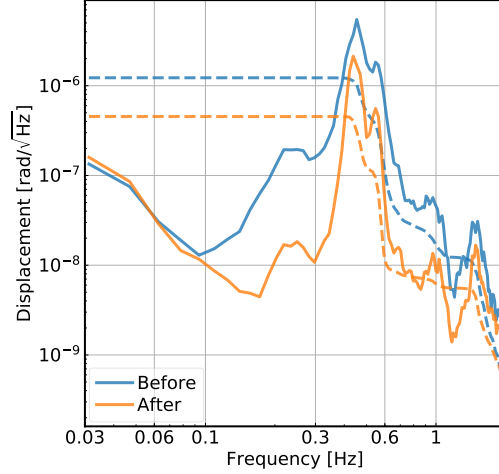
Figure 3-19: The performance of the length-to-angle feedforward subtraction measured locally with the optical levers.

ward. As a comparison, the input displacement noises when the feedforward cancellation is turned on are represented by the orange traces. We can see that for the differential-hard mode (measured with AS_A_RF45_Q), we achieve a robust subtraction of input motion in the 0.1-0.3 Hz microseismic band with approximately 60% reduction in power. This significantly reduces the rms of the input motion and opens up the possibility of reducing the feedback control's bandwidth in the future. The performance in the common hard mode, however, is limited. In part, this is due to a non-ideal inversion of the input matrix at the REFL port. At the same time, people have noticed that the common-hard mode signal exhibits large coherence with the motion of the chamber hosting the REFL port sensors. This might be further caused by thermally induced offsets creating a non-vanishing RF spot on the WFS, which cross-couples the local centering loops (which sees the chamber motion) and the interferometric WFS signals. To solve this issue in the future, a better seismic isolation system is planned for the chamber hosting the REFL sensors [?]. Meanwhile, people are actively researching the possibility of feeding forward the global longitudinal signals (i.e., measured with the interferometric sensors instead of local seismometers) to mirrors' alignment [?], which, based on the coherence between signals, might remove

93

up to 90% of input motion to the common-hard mode.

(a) Differential-hard mode.   (b) Common-hard mode.
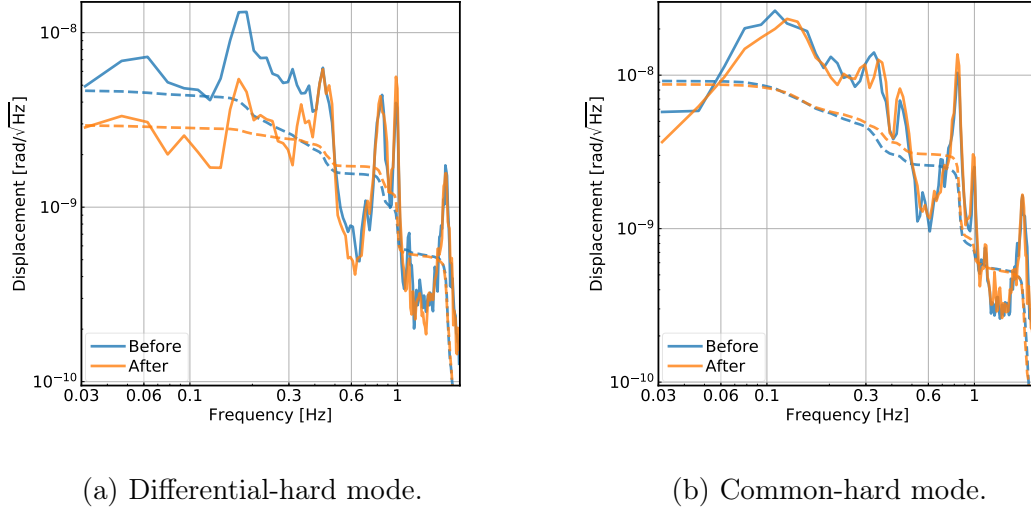
Figure 3-20: The performance of the length-to-angle feedforward subtraction measured with global alignment signals.

3.5.2   Signal blending

At the beginning of this Chapter we said that the typical sensing noise for the alignment control loops is about 10^{-14} rad/$\sqrt{\text{Hz}}$. This is the case for the differential hard modes measured with AS_A_RF45_Q as illustrated in Figure 3-21a. For the common-mode signals sensed with a combination of REFL WFSs (the red-dotted curve in Figure 3-21b), however, the sensing noise is significantly worse, at a level of as high as a few$\times 10^{-13}$ rad/$\sqrt{\text{Hz}}$. This is partially due to an intrinsically higher shot noise level at the REFL port than at the AS port [22]. Moreover, the REFL sensors are subject to the cross-couplings from chamber motions we have just discussed above. This is further suggested by the fact that in the 10-30 Hz band the spectrum of the REFL WFS error signal is not flat (which is characteristic for shot noise and dark noise). As we have discussed in Section 3.1, with a sensitivity of 10^{-14} rad/$\sqrt{\text{Hz}}$ the alignment control loop will already inject so much sensing noise that limits aLIGO's sub-30 Hz sensitivity. A higher level of sensing noise will lead to an even worse contamination to the main GW readout.

94
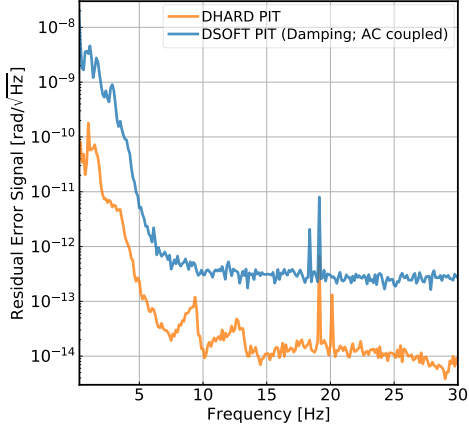
(a) Differential modes in pitch. (b) Common modes in yaw.
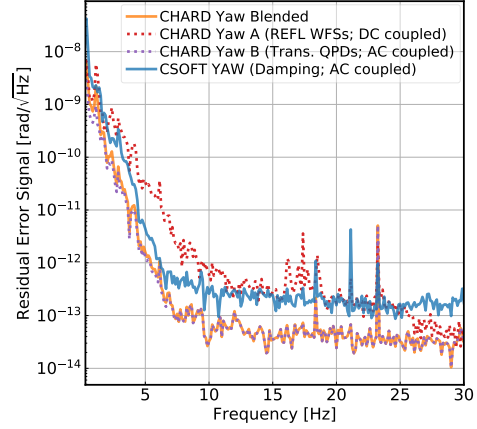
Figure 3-21: Sensing noise level of alignment loops.

To circumvent this, note that we only need an interferometric error signal (cf. Section 2.2) of the common-hard modes at DC. At AC frequencies, the motion of the recycling cavity's axis is much smaller than the motion of the arm cavity's axis [by a factor of $\sim 1/(1-r_i) \simeq g_a^2/2$] and thus we can treat the recycling cavity's axis as being essentially static at AC. Consequently, we can use non-interferometric sensors such as the QPDs on the transmissions of the test masses to control the AC hard-mode motion. These QPDs typically have sensing noise of a few$\times 10^{-14}$ rad/$\sqrt{\text{Hz}}$, much lower than the REFL WFS's noise level.

In practice, we blend the REFL WFSs' output and QPDs' output together to form the final error signal of the common-hard modes. The REFL WFSs' signals are DC-coupled and then low-passed with two poles at 0.8 Hz. The compliment of this low-pass filter is then multiplied with the QPDs' output to form the AC part of the error signal. As a result, the sensing noise of common-hard mode is reduced from the red-dotted line to the orange-solid line (which is essentially the same as the purple-dotted line above 10 Hz) in Figure 3-21b. It consequently reduces the common-hard loop's contamination to DARM by about a factor of 10.

Lastly, we also show the sensing noise for the soft modes (for the damping part; see Section 3.4) in the solid-blue traces. While their sensing noise is about a factor of

20 higher than that of the hard mode, their bandwidth is also smaller ($\simeq 1$ Hz) and thus their contribution to the DARM noise is less severe than the hard modes.

3.5.3 Optimal control design using the $\mathcal{H}_\infty$ method

We have discussed in Section 3.1 that our current controller for the alignment loop is suboptimal because it needs to maintain the loop stability as the suspension plant varies significantly over a range of different circulating powers. On the other hand, we have shown in Section 3.3.3 that the newly implemented radiation compensation techniques allows the removal of the Sidles-Sigg effect and thus keep the effective suspension plant unchanged. It thus opens up the possibility of plant inversion in our controller to optimize the overall loop performance. In this Section, we introduce the $\mathcal{H}_\infty$ optimization method (for a nice review of optimal control methods, see Ref. [?] and references therein) and show that with this approach we can improve our alignment control to simultaneously reach the requirements set on both the suppression of low-frequency rms motion and the cutoff of high-frequency sensing noise (cf. Section 3.1).

The alignment control of aLIGO can be treated as a mixed sensitivity problem [?, ?, ?], which is a special kind of $\mathcal{H}_\infty$ problem. The generic diagram for this problem is illustrated in Figure **??**, where, to be consistent with the previous sections, we have labeled the plant as S (which we know) and the controller as K (which we want to find as the solution to the problem). With noise input w and outputs $\boldsymbol{z} = [z_1, \ z_2]^{\mathrm{T}}$, the system can be described as

$$
\boldsymbol{z} = \begin{bmatrix} z_1 \\ z_2 \end{bmatrix} = \underbrace{\begin{bmatrix} W_1/(1+SK) \\ -W_2 K/(1+SK) \end{bmatrix}}_{H} w, \tag{3.40}
$$

where W_1 and W_2 are some custom weighting functions. As we shall see soon that the output z_1 weighted by W_1 corresponds to the residual displacement noise that sets the low-frequency requirements, and the z_2 weighted by W_2 corresponds to the residual sensing noise that determines the high-frequency cutoff. For future convenience, we

will also introduce $W_3 = W_2/S$. The objective of the problem can be stated as the following. Given the above system (that is, we know the plant S as well as the weights $W_{1,3}$), we want to find a controller K such that

1. it stabilizes the closed-loop system, and

2. it minimizes the ∞-norm $||H||_\infty$ of the closed-loop transfer matrix H from input w to outputs $\boldsymbol{z}$.

In the single-input-single-output case (which is appropriate for the alignment control system in aLIGO), the second point reduces to finding K such that the quantity

$$\sup_{\omega \in \mathbb{R}} \left[\left| W_1(\omega) \frac{1}{1 + S(\omega)K(\omega)} \right|^2 + \left| W_3(\omega) \frac{S(\omega)K(\omega)}{1 + S(\omega)K(\omega)} \right|^2 \right] \tag{3.41}$$

is minimized.

To proceed, let us first discuss the choice of the frequency-dependent weighting functions W_1 and $W_3 = W_2/S$. Thanks to the equalizing property, it implies that when the optimal solution is obtained, the quantity in (3.41) is often a constant [?]. Let us denote this constant as γ^2 with $\gamma \geq 0$. It then implies

$$\left| W_1(\omega) \frac{1}{1 + S(\omega)K(\omega)} \right|^2 \leq \gamma^2, \tag{3.42a}$$

$$\left| W_3(\omega) \frac{S(\omega)K(\omega)}{1 + S(\omega)K(\omega)} \right|^2 \leq \gamma^2, \tag{3.42b}$$

for $\omega \in \mathbb{R}$. At low frequencies with $\omega \ll \omega_{\mathrm{bw}}$ where ω_{bw} corresponds to the angular frequency of the control bandwidth, we want the quantity $|SK| \gg 1$ so that we have sufficient loop suppression. Consequently we want $|W_1| \gg |W_3|$ there so that the term (3.42a) dominates, with $|W_1/(1 + SK)| \simeq |W_1/SK| \simeq \gamma$. In other words, the low-frequency loop suppression is given by

$$|SK| \simeq \gamma |W_1| \text{ for } \omega \ll \omega_{\mathrm{bw}}. \tag{3.43}$$

Similarly, at high frequencies with $\omega \gg \omega_{\mathrm{bw}}$, we want $|SK| \ll 1$ to minimize the injection of the sensing noise. Therefore we want the term (3.42b) to be dominant, with $|W_3 SK/(1 + SK)| \simeq |W_3 SK| \simeq \gamma$. This leads to a high-frequency cutoff

$$|SK| \simeq \frac{\gamma}{|W_3|} \text{ for } \omega \gg \omega_{\mathrm{bw}}. \tag{3.44}$$

Pratically, we usually have some goals $|SK|^{(\mathrm{trgt})}$ that we would like the control loop to achieve. Therefore, we can turn the above equations around to set the weighting functions as

$$|W_1(\omega)| = \gamma |S(\omega)K(\omega)|^{(\mathrm{trgt})} \text{ for } \omega \ll \omega_{\mathrm{bw}}, \tag{3.45a}$$

$$|W_3(\omega)| = \frac{\gamma}{|S(\omega)K(\omega)|^{(\mathrm{trgt})}} \text{ for } \omega \gg \omega_{\mathrm{bw}}. \tag{3.45b}$$

In general, the constant $\gamma \sim 1 - 10$. The problem thus is further reduced to finding K that "optimally" satisfies the goals set by the waits $W_{1,3}$.

Actually, the optimal solution to this problem is generically challenging. Nevertheless, what is easier to find is the *suboptimal* solution. In this suboptimal problem, one can determine first if there exists a stabilizing K that achieves $||H||_\infty < \gamma$ for some given $\gamma > 0$, and if such K exists, it can be obtained explicitly based on Ref. [?]. Then a search in γ can bring us to approach the optimal controller K. This algorithm has been implemented in commercially available softwares. For instance, the results we will show for aLIGO's alignment loop design are calculated with the `hinfsyn` function [?] in `MATLAB`'s Robust Control Toolbox[14].

We are now ready to consider how we can use this $\mathcal{H}_\infty$ method to improve our aLIGO's alignment control. Let us focus here on the control of the hard modes in pitch as an example. In our case, the plant is given by $S = S_{R_{\mathrm{h}}}(10 \text{ W})$ [cf. equation (3.18)] and is unaffected by the real input power thanks to the radiation pressure compensation system. The weighting functions W_1 and W_3 we use are shown in Figure 3-22. They are determined based on the following considerations.

---

[14]https://www.mathworks.com/products/robust.html
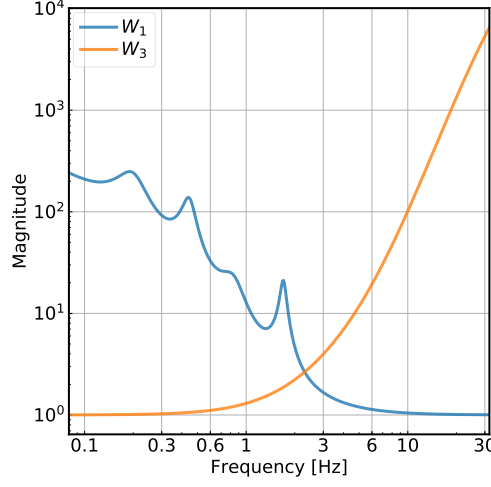
Figure 3-22: Weighting functions used for the $\mathcal{H}_\infty$ design.

The displacement noise input to the system is given by $S_{R_\mathrm{h}}(10\ \mathrm{W})\tau_\mathrm{in}^{(\mathrm{disp})}$ where $\tau_\mathrm{in}^{(\mathrm{disp})}$ is given by the right panel of Figure 3-1[15]. To suppress such a noise, we would like to have the controller rising as $1/f^2$ between the secondary and primary resonances and as $1/f$ below the primary resonance so that the spectral shape of the residual noise is essentially white below 1 Hz. At the 0.1-0.3 Hz microseismic band, we would like a factor of 20 suppression from the control loop. We thus fine tune the zeros of W_1 until it reaches $|W_1(0.2\ \mathrm{Hz})| = 100$ from the smooth part [cf. equation (3.45a); we have assumed $\gamma = 5$ in our design]. We further enhances the loop suppression by adding resonant gains at both the microseismic band and the suspension resonances (at the main length-to-pitch resonance as well as the main and the secondary pitch-to-pitch resonances).

For the sensing noise, as noted in Section 3.1, we need $|SK|^{\mathrm{trgt}} < 0.06$ in order to reach aLIGO's noise requirement at 10 Hz. Therefore we set $|W_3(10\ \mathrm{Hz})| = 100$ according to equation (3.45b). We also let $|W_3|$ rises as f^5 locally at 10 Hz so that the alignment noise decreases faster than the fundamental quantum noise ($\propto f^{-2}$) and the suspension thermal noise ($\propto f^{-5/2}$).

---

[15]Equivalently, it can be obtained by $\theta_\mathrm{in}^{(\mathrm{disp})}(10\ \mathrm{W}) = \theta_\mathrm{in}^{(\mathrm{disp})}(0)/(1 + R_\mathrm{h}S_0)$ with $\theta_\mathrm{in}^{(\mathrm{disp})}(0)$ given by the left panel of Figure 3-1.

Once the weights are specified, we can solve for the optimal controller K using MATLAB's `hinfsyn` function. The open loop transfer function SK is shown in Figure 3-23. In the figure the red trace represents the result obtained with the $\mathcal{H}_\infty$ design, and the black trace is the one we use currently (cf. Figure 3-4). The $\mathcal{H}_\infty$ design has a significantly faster roll-off at 10 Hz compared to the original design. On the hand, the stability of the loop is not compromised by the sharp cutoff, as the red trace has a phase margin of $\simeq 30°$, as large as the original design.
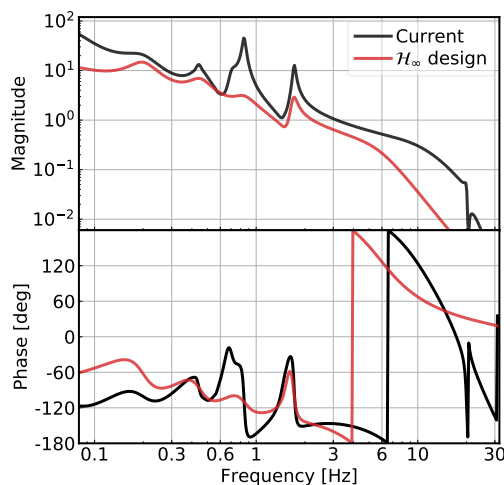
Figure 3-23: The open loop transfer function SK of the hard modes in pitch.

While the low-frequency gain is smaller for the new controller, in Figure 3-24 we show that the residual low-frequency motion is sufficiently low, with a rms of 0.8 rad/$\sqrt{\text{Hz}}$. Note that here we does not include any length-to-angle feedforward subtractions. With the feedforward on, the low frequency motion can be further reduced. Consequently, the $\mathcal{H}_\infty$ controller meets the requirements on both the cutoff of high-frequency sensing noise, and the suppression of low-frequency input motion. The $\mathcal{H}_\infty$ method is thus a promising way to improve the alignment control for both aLIGO and future generations of GW detectors.
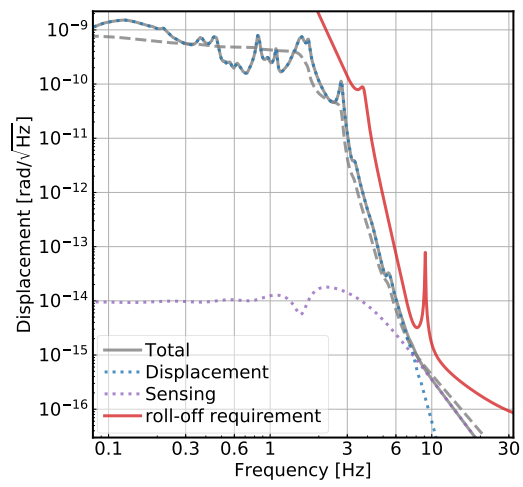
Figure 3-24: The residual motion of the hard loop using the controller designed with the $\mathcal{H}_\infty$ method.

Chapter 4

Thermal distortions in aLIGO

In addition to the radiation pressure effects, the thermal distortion is another challenge posed by aLIGO's high-power operation. The significant amount of circulating power (up to 0.7 MW) in aLIGO's arm cavities may be absorbed by the mirror coatings with a coefficient of about 0.5 ppm. The spatial Gaussian distribution of the laser beam may thus lead to a radial temperature gradient, which subsequently create both thermorefractive substrate lenses and thermoelastic surface deformation. As a result, the beams wavefront of will be distorted by the thermal lenses as the circulating power increases, degrading the mode-matching between different optical cavities. To tackle this challenge, a thermal compensation system has been developed for aLIGO [11]. However, the performance of this system is limited by the presence of point absorbers that are hardly anticipated until the circulating power reaches $\mathcal{O}(0.1)$ MW. Moreover, the current actuators for the thermal compensation system are designed for absorptions whose spatial profiles are given by the cavity 00 mode, and consequently are not capable to compensate for those due to point absorbers involving high spatial orders.

In this Chapter we will explore some phenomena induced by the thermal wavefront distortion. While in reality the residue distortion is caused mainly by point absorbers involving high spatial orders, here we will nonetheless simplify the problem by modeling it as excess thermal lens and truncate the spatial order to second order (i.e., we include only up to 02/20 modes in our calculations). Consequently, we do

not intend to reproduce the exact aLIGO interferometer in our study, but instead focus on capturing the key consequences generated by the thermal distortions.

4.1   Alignment sensing of the signal-recycling cavity

As we have briefly mentioned in Section 2.4, the signal-recycling cavity's axis was originally controlled by actuating on the SRM using an error signal derived from AS_A_RF36_I. However, at both observatories this ceased to be functional once the input power increased above ~ 20 W. To understand why this situation happened, we discuss here two major drawbacks of this signal.

Note first that here the "RF36" signal (at 36.4 MHz) is the beat note between the two RF sidebands at $f_1 = 9.1$ MHz and $f_2 = 45.5$ MHz. In an ideal interferometer without cavity offsets, the 00 modes of the RF sidebands satisfy $E(-f_i) = -E^*(f_i)$ for $i = 1, 2$ if we set the input carrier field to be real. Thus the whole-plane integrated 36.4 MHz signal can be written as

$$S(36.4 \text{ MHz}) = E^*(-f_2)E(-f_1) + E^*(f_1)E(f_2) = 2E^*(f_1)E(f_2), \qquad (4.1)$$

which does not vanish. This is in contrast to the beat note between a RF sideband and the carrier field $E(0) \in \mathbb{R}$, which is given by

$$S(f_i) = E^*(-f_i)E(0) + E(0)E(f_i) = 0. \qquad (4.2)$$

Therefore for the RF36 signal we define the I phase to be the phase at which $S(36.4 \text{ MHz})$ shows up. In other words, the RF beam spot shows up in the I phase.

In Figure 4-1 we show the simulated AS_RF36 responses to SRM misalignment as function of the detector's Gouy phase (and therefore we have dropped the "A" in the sensor name) using `FINESSE` [2]. Here we can first focus on the blue trace that assumes an ideal interferometer with perfect mode matching. From the figure, the SRM alignment signal shows up mainly in the I phase, and this is the first issue of the AS_RF36 signal. As we have discussed in Section 2.3, a real WFS derived from
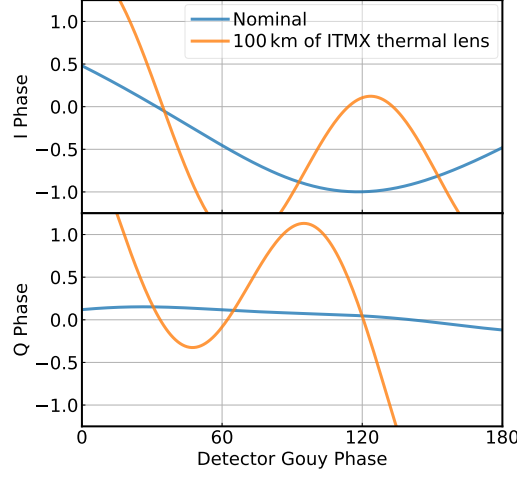
Figure 4-1: The response of the AS_RF36 signal to SRM misalignment as a function of the detector's Gouy phase. The top and bottom panels show the error signal in the I and Q phases, respectively. The blue trace corresponds to an ideally mode-matched interferometer and the orange trace represents the case with wavefront distortion induced by 100 km of thermal lens. We have normalized the signals by the maximum amplitude of the response in the ideal interferometer.

a carrier-sideband pair has the nice property that it is insensitive to spot centering thanks to the property shown in equation (4.2). This is, however, no more true for the 36.4 MHz signal due to equation (4.1) and the fact that the SRM alignment signal is mainly in the I phase. As a result, if the sensors drift in position with respect to the main interferometer, the AS_RF36 signal cannot distinguish such an effect from a real SRM misalignment. Moreover, as the interferometer powers up, the thermally induced carrier contrast defect may leak to the anti-symmetric port and contaminate the centering loops that steer the DC spot to the PD. The centering loops then drive the spot at 36.4 MHz to be off-centered, and consequently offsets the SRM's alignment via the alignment feedback [33].

The second drawback of the scheme is illustrated by the orange trace in Figure 4-1. Here we introduce an extra thermal lens in the ITMX substrate. The focal length of the lens is set to $f_{ix} = 100$ km, which creates approximately the same amount of scattering loss in the carrier 00 field as the point absorber developed at the Hanford observatory during the second observing run [34]. The thermal lens dramatically

changes the error signal's response. While in the nominal case two sensors separated by $\pi/2$ in Gouy phase would be sufficient to reconstruct error signal in the entire Gouy phase space, when 02/20 modes are present, this is no more the case. For instance, if we happen to place the two sensors at Gouy phases of 30° and 120°, the response may essentially vanish in both sensors. Moreover, the signal at about a Gouy phase of 120° (which corresponds to the peak sensitivity in the nominal case) changes sign as we include the thermal lens and destabilize the system.
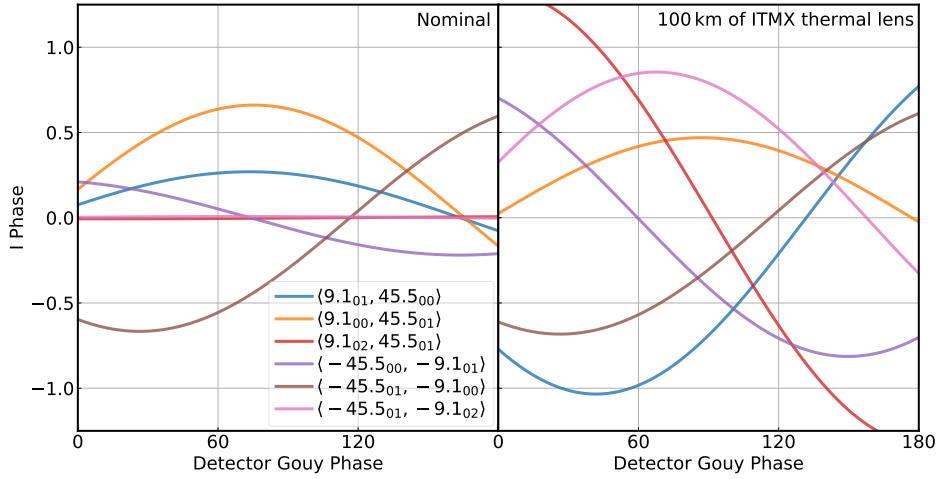
Figure 4-2: Decomposition of the AS_RF36_I signal. On the left is the ideal case with the interferometer perfectly mode-matched. On the right 100 km of extra ITMX thermal lens is introduced.

We further examine the error signal decomposition in Figure 4-2. In the legend we use $\langle f'_{m'n'}, f_{mn} \rangle$ to denote the beat note between the $m'n'$ mode of RF sideband with frequency f' and the mn mode of sideband f. The beat note is detected at a WFS (i.e., we subtract the upper- and lower-half planes to derive the signal). Here we focus on alignment in pitch so $m = m' = 0$, and parity enforces a vanishing signal if $n - n'$ is even. In the ideal interferometer, the error signal is dominated by the 9.1 MHz 00 mode beating 45.5 MHz 01 mode and their complex conjugates (note that the signals are not symmetric because of the Gouy phase, see Section **??**). When differential wavefront distortion is taken into account, however, the 02 mode of the 9.1 MHz sideband creates a beat note with the 45.5 MHz 01 mode much greater than

the 9.1 MHz 00 mode does. Furthermore, $\langle 9.1_{01}, 45.5_{00} \rangle$ also increases significantly. This is because the 01 mode can be generated not only from the 00 mode but also the 02 mode by reflection upon a misaligned mirror. As the 02 mode of the 9.1 MHz has a greater amplitude than the 00 mode in the signal-recycling cavity, it becomes the main source from which the 01 mode is generated. As a consequence of both effects, the signal content of the AS_RF36 changes dramatically when 02/20 modes are included.

Figure 4-2 indicates that the drastic modification is due to a large $|E_{02}(f_1)|/|E_{00}(f_1)|$ ratio (with $f_1 = 9.1$ MHz) at the anti-symmetric port. The question then becomes the following. What determines this ratio and why is it so large? Since both $E_{00}(f_1)$ and $E_{02}(f_1)$ are off-resonance in the low-finesse signal-recycling cavity, we can ignore the signal-recycling cavity's filtering effects. Then each mode's amplitude is determined by how much it transmits through the Michelson. For the 00 mode, the transmissivity is determined by the Schnupp asymmetry $l_{\mathrm{sch}} = 0.08$ m (cf. Section 1.2.2),

$$|E_{00}(f_1)| \propto \sin\left(\frac{2\pi f_1 l_{\mathrm{sch}}}{c}\right) \simeq \frac{2\pi f_1 l_{\mathrm{sch}}}{c} = 1.5\%. \tag{4.3}$$

For the 02 mode, on the other hand, it is due to the differential wavefront distortion,

$$|E_{02}(f_1)| \sim \frac{1/\Delta \mathrm{f}}{1/\mathrm{RoC_i}} \simeq 2\% \times \left(\frac{100 \text{ km}}{\Delta \mathrm{f}}\right), \tag{4.4}$$

where $\Delta \mathrm{f}$ is the differential thermal lens and $\mathrm{RoC_i}$ is the radius of curvature of the ITM. In the above expression we have ignored order unity corrections. Because of the small transmissivity of $E_{00}(f_1)$ through the Michelson, even a few percent of differential wavefront distortion can lead to a significant amount of high-order mode compared to the main 00 component. Note that the above equations are all for amplitudes. In terms of contrast defect defined in power, it means the $E_{00}(f_1)$ will be greater than the higher-order-mode contaminations only if the contrast defect is better than 100 ppm. Such a condition is hardly satisfied in aLIGO even without point absorbers.

Consequently, an error signal that is more robust against wavefront distortion is

in demand. This leads to the addition of a third RF sideband to the interferometer at $f_3 = 118.3$ MHz and the new AS_RF72_Q detection scheme [35]. In this scheme, the error signal will be derived from the beat note between the existing 45.5 MHz sideband and the new 118.3 MHz sideband. To see why this signal is more robust, we again consider the ratio $|E_{02}(f_3)|/|E_{00}(f_3)|$. For the 00 mode, note that the transmissivity through the Michelson is proportional to the RF frequency, meaning that the transmissivity of the $E_{02}(f_3)$ is about 13 times greater than that of $E_{00}(f_1)$. The transmissivity of the 02 mode, nonetheless, is independent of frequency and about same fractional amount of $E_{02}(f_3)$ is leaked to the anti-symmetric port as $E_{02}(f_1)$. Overall, this leads to

$$\frac{|E_{02}/E_{00}(f_3)|}{|E_{02}/E_{00}(f_1)|} \simeq \frac{f_1}{f_3} \simeq \frac{1}{13}, \tag{4.5}$$

based on our simple arguments above. After taking the signal-recycling cavity's filtering effect into account, a `FINESSE` simulation leads to a ratio of $1/8.5$. Therefore, we should expect the RF72 error signal to be about 10 times more robust than the RF36 signal against thermal distortions.

This is confirmed by the numerical simulation shown in Figure 4-3 where we consider the signal's response to SRM alignment in both the ideal case and the case with thermal distortion. The signal decomposition is shown in Figure 4-4. In the new 72.8 MHz signal, the fractional variations both in the overall response and in each individual beat note pair are significantly reduced compared to the 36.4 MHz signal. Moreover, in this scheme the SRM signal shows up equally in the I and Q phases. This means that we can use the Q phase signal to sense the signal-recycling cavity's alignment, and it is orthogonal to the spot position variation that shows up only in the I phase. Consequently, even if the carrier contrast defect contaminates the DC centering loop, the alignment of the signal-recycling cavity will not be biased with the AS_RF72_Q signal.

The new scheme has been implemented at both LIGO observatories prior the third observational run and works properly at an input power of 40 W. In contrast, the original RF36 signal could not be used once the input power increases beyond
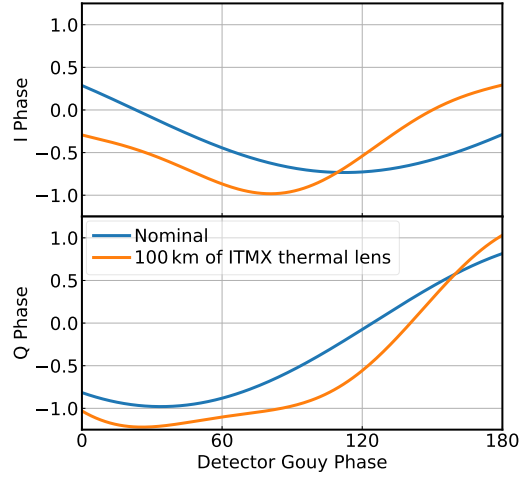
Figure 4-3: Similar to Figure 4-1 but this time it shows the AS_RF72 error signal as a function of the detector Gouy phase. Compared to the AS_RF36 signal, the AS_RF72 signal sees significantly less variations due to differential thermal lenses. Moreover, the response is largely in the Q phase, decoupling the decoupling between spot position drifts and the true signal-recycling cavity's alignment signal.
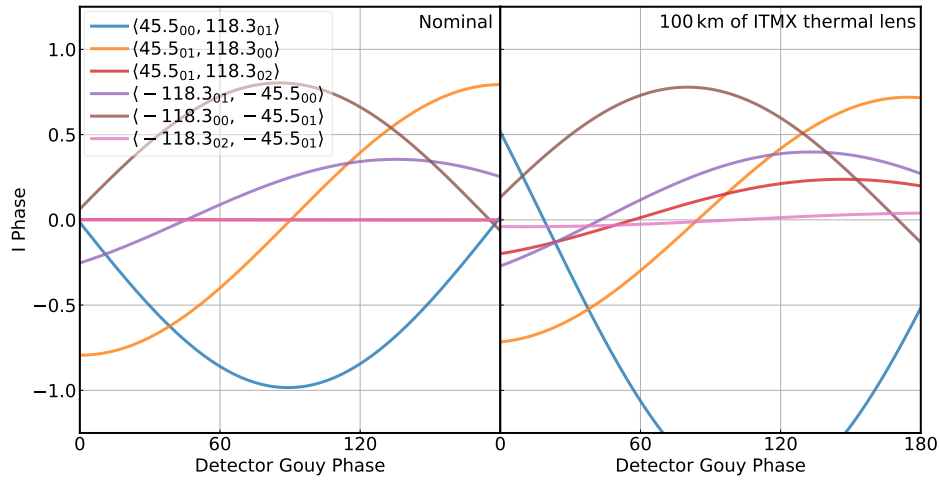
Figure 4-4: Decomposition of the AS_RF72_I signal.

20 W [36].

4.2 Detuning of the signal recycling cavity

In Section 1.3.2 we derived the DARM optical response in the resonant-sideband-extraction configuration, corresponding to a microscopic longitudinal tuning of the SRM of $\phi_s = 90°$. If ϕ_s deviates from an integer number times $\pi/2$, an optical spring will be formed [37]. In Figure 4-5 we present the DARM optical responses at $\phi_s = 90°$, $89.5°$, and $90.5°$, corresponding to the blue, the orange, and the red traces, respectively. We choose these values because in aLIGO's second observing run, the Hanford observatory experienced an unintentional detuning of the SRM of $-0.5°$ from its nominal position, or $\phi_s = 89.5°$ [6, 38][1]. The detuning reduces the DARM optical response at $\lesssim 30$ Hz and thus degrades the sensitivity in the same band. In this Section we propose a model to explain this effect [39], and show that the same extra ITMX thermal lens causing SRM alignment issues in the previous Section is also responsible for the detuning of SRM.

The physical process can be summarized as the following. The thermal lens creates a phase shift on the RF sidebands quadratic in the radius of curvature mismatch (for the carrier field this effect is at a higher order as it is resonant in the arm cavity). Such a phase shift breaks the symmetry between the upper and lower sidebands such that $-E(f_{RF}) \neq E^*(-f_{RF})$. Consequently, the PDH error signal for a degree of freedom is not zeroed anymore even there is no real detuning in that degree of freedom (as experienced by the carrier field to the quadratic order in the wavefront mismatch). However, the control loop cannot distinguish such a higher-order-mode contamination from the real error signal, and as the controller tries to zero the signal, it actually introduces an offset.

In Figure 4-6 we show the error signal[2], S_{srcl}, for the signal-recycling cavity's

---

[1]Our sign convention follows that defined in `FINESSE`, which is opposition to the one used in Ref. [6].

[2]In aLIGO, it is a linear combination of POP_9_I and POP_45_I that is insensitive to length fluctuations of the power-recycling cavity.
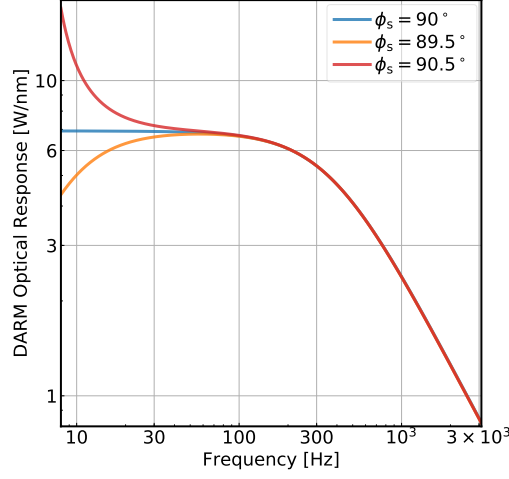
Figure 4-5: The optical response of DARM at different SRM tunings. The orange trace ($\phi_s = 89.5°$) is consistent with the measured optical response of the LIGO Hanford observatory during the second observing run.

length, or SRCL, as a function of the inverse of extra ITMX thermal lens, or $1/f_{ix}$. In the process, no physical detuning in SRCL (experienced by the carrier filed that contains the GW signal) is introduced, and the error signal deviates from zero because of the higher-order-mode contamination in the RF sidebands. As a comparison, the red-dotted line is the error signal caused by a real SRCL detuning of 0.5°, and we have normalized the response such that it corresponds $S_{srcl} = 1$. The plot indicates that for an extra ITMX thermal lens of $f_{ix} \simeq 100$ km, it may induce an error signal equivalent of 0.5°. Then as the negative feedback control is engaged, it will detune the SRM to $\phi_s = 89.5°$ to zero this signal, which further induces the anti-spring in the DARM optical response.

To further confirm the above mechanism, we utilize the `lock` command in `FINESSE` [2]. Specifically, in our numerical models we construct an error signal for SRCL as it is done in the real aLIGO interferometer, and feed it to the SRM longitudinal tuning ϕ_s iteratively to zero the error signal. Therefore, we are able to simulate the real interferometer's control loops in our numerical models, thereby study the detuning in a realistic way.

The results are illustrated in Figure 4-7. The blue trace shows the nominal DARM
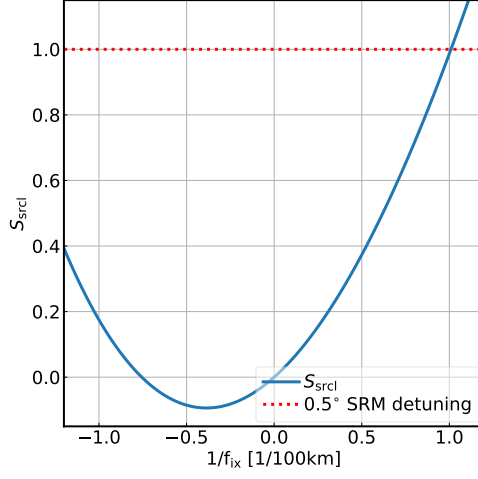
Figure 4-6: The SRCL error signal as a function of the inverse of extra ITMX thermal lens. The differential thermal lens induces an offset that is quadratic in the radius of curvature mismatch (it is not exactly symmetric about $1/f_{ix} = 0$ due to the intrinsic mode-mismatch in our numerical model). When $f_{ix} \simeq 100$ km, the higher-order mode induced offset equals to that from a real $0.5°$ detuning of SRM (indicated by the red-dotted line).

optical response with $\phi_s = 90°$ (i.e., the resonant-side-band extraction configuration). To study the effect of thermal distortion, we introduce an extra ITMX thermal lens of $f_{ix} = 100$ km to mimic the point absorber in the second observing run. Meanwhile, we use the `lock` command to keep the SRM at a position zeroing its error signal. After the lock is completed, we then compute the DARM optical response and the result is shown in the orange trace. Indeed, a loss of response at sub-30 Hz is observed, consistent with the $-0.5°$ detuning of the SRM (cf. the orange trace in Figure 4-5) measured at the Hanford observatory. To verify this is an effect due to the offset in the feedback control, we also present the DARM optical response in the purple-dashed line where we introduce the same amount of thermal lens but do not engage the SRCL feedback. It is inconsistent with the measurement (actually, a small positive optical spring is formed due to effects at higher order in radius of curvature mismatch), and thus indicates that the thermal lens by itself is unlikely to explain the observed anti-spring. Lastly, for completeness we also consider the effects due to a common thermal lens. This time we put $f_{ix} = f_{iy} = 100$ km to both the ITMX and ITMY, and then

engage the `lock` command for SRCL. The result is illustrated in the red trace, which is essentially consistent with the nominal case.
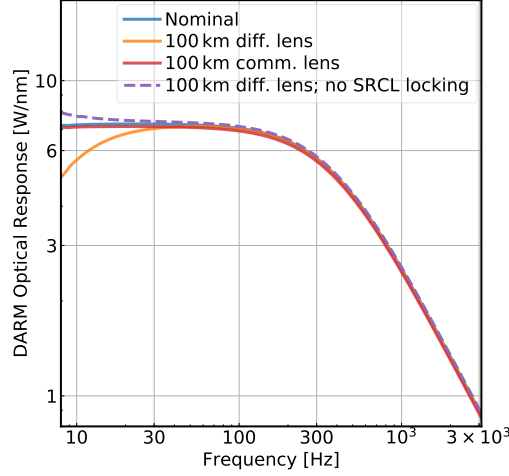
Figure 4-7: The optical response of DARM at different interferometer configurations. The thermal lens induces an offset in SRCL locking point, which detunes the SRM via the control feedback and creates an anti-spring in the DARM response (the orange trace). On the other hand, with only the thermal wavefront distortion but no control feedback it is insufficient to create the anti-spring as indicated by the dashed-purple trace.

To summarize, we have proposed a mechanism to explain the observed loss of low-frequency DARM response. That is, the thermal lens that contaminates mostly the RF sidebands induces on offset in the PDH error signal, and to zero this signal, the control loop detunes the SRM, which affects both the RF sidebands and the carrier field. The net result is thus a detuning on the carrier field that carries the GW signal.

Chapter 5

Prospects for Detecting Gravitational Waves at $5\,\mathrm{Hz}$ with Ground-Based Detectors

5.1 Introduction[1]

The detection of GWs from coalescing binary black holes (BHs) [40, 41] by aLIGO [42] and Advanced Virgo (aVirgo) [43] heralded the era of GW astrophysics. However, detecting binaries that are more massive and further away than the current BH catalog is challenging. Since the merger frequency decreases as the total mass of the binary increases, systems more massive than a few $\times 100\,M_\odot$ will no longer lie in the most sensitive band of aLIGO. Intermediate-mass black holes (IMBHs) are an example of systems likely to be missed by aLIGO [44, 45, 46, 47, 48, 49] . At the same time, a pair of $30\,M_\odot$ BHs at $z = 2$ will appear to have a total mass of $180\,M_\odot$ due to the cosmological redshift [50], illustrating the difficulties of detecting even the stellar-mass BHs at cosmological distances. Therefore, improving the low-frequency sensitivity plays a crucial role in extending both the mass and the spatial range of detectability.

---

[1]This Chapter is based-on [1].

Another scientific goal of GW detectors is to enable multimessenger astronomy, as demonstrated by the detection of a merging neutron star (NS) binary in GW and the follow-ups by electromagnetic telescopes [51, 52]. To help the subsequent observations, GW observatories need to provide the source location not only accurately but also quickly. Since the time to merger scales with frequency f as $f^{-8/3}$, if the error area can shrink small enough at a lower frequency, the location information can be sent out at a much earlier time. Consequently, improving the low-frequency sensitivity allows for more timely follow-up observations.

In this Chapter we propose an upgrade to aLIGO (and its evolution A+ [53]) that enables a significant enhancement in sensitivity in the 5-30 Hz band while maintaining high frequency performance. This new design, dubbed "LIGO-LF", can be implemented on a timescale of ~10 yr and serve as a pathfinder for later upgrades like the Voyager [54] and next-generation detectors like the Einstein Telescope [55, 56] and Cosmic Explorer [57].

5.2   LIGO-LF design.

The current aLIGO sensitivity below 30 Hz is limited by nonstationary technical noises [58, 21, 6]. Here we describe the solutions that we propose to reach the LIGO-LF sensitivity shown in Fig. 5-1.

The first element of the upgrade reduces the angular control noise. Angular motion of the optics is actively stabilized using wavefront sensors with a typical sensitivity of $5 \times 10^{-15}\,\mathrm{rad}/\sqrt{\mathrm{Hz}}$ [22, 21]. The bandwidths of the arm cavity angular loops are set to 3 Hz for aLIGO to simultaneously suppress the radiation torque [23, 24, 25] and reduce the seismically induced motion to a few nrad rms (cf. Chapter 3). However, the control noise disturbs the test masses above 5 Hz and contaminates the GW readout via beam mis-centering on the mirrors. To reach the LIGO-LF requirements, we thus need to reduce the control bandwidth to $\lesssim 1$ Hz.

Consider first the effects of radiation pressure. As we have discussed in Section 3.3,

116
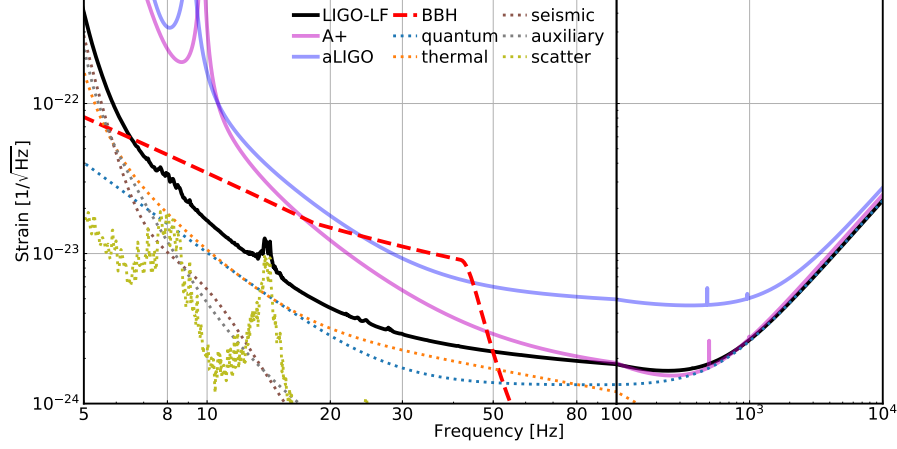
Figure 5-1: Proposed sensitivity for LIGO-LF (solid black line) and its noise budget (dashed lines). Also shown in the dotted red curve is the spectrum of a $200\,M_\odot$-$200\,M_\odot$ binary BH merger (in the detector frame) at $10\,\mathrm{Gpc}$. LIGO-LF's sensitivity to such systems is greatly enhanced relative to aLIGO (solid blue line) and A+ (solid magenta line). Throughout this Letter, we will adopt the same coloring convention when we compare different sensitivities (i.e., we use black, magenta, and blue for LIGO-LF, A+, and aLIGO, respectively).

the shift in the suspension resonant frequency due to the radiation torque is given by

$$\Delta(\omega_\pm^2) = \frac{PL}{Ic}\left[\frac{(g_e + g_i) \mp \sqrt{(g_e - g_i)^2 + 4}}{(g_e g_i - 1)}\right], \qquad (5.1)$$

where we have used $+(-)$ to represent the hard (soft) mode. To mitigate it, we propose to increase LIGO-LF's test masses from 40 to 200 kg, which also improves the fundamental noises and is a fundamental part of next-generation GW detectors. The moment of inertia of the test masses consequently increased by a factor of $5^{5/3} \simeq 15$ if we assume the mirror geometry stays the same as that of the aLIGO mirror. With further geometrical optimization, a factor of 30 increase in I would be possible. For LIGO-LF, we also slightly reduce the radius of curvature of the ITMs to $g_i = -1.21$ so that the spot size on the ETMs are increased by 50% to reduce the coating thermal noise. As a result, for LIGO-LF we have $\Delta(\omega_+^2) = (2\pi \times 1.0\ \mathrm{Hz})^2$ for the hard mode and $\Delta(\omega_-^2) = -(2\pi \times 0.11\ \mathrm{Hz})^2$ for the soft mode with 0.8 MW of power circulating

117
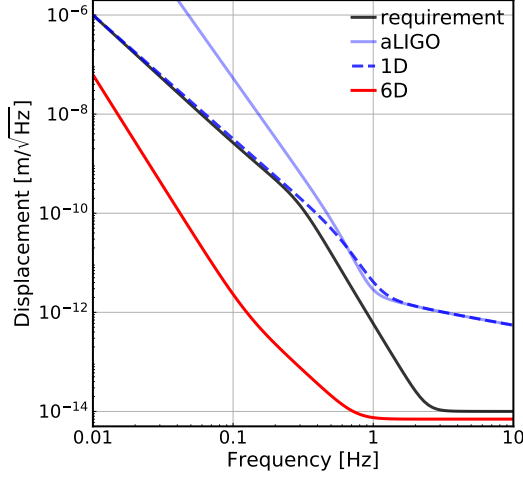
Figure 5-2: Inertial sensor noise for aLIGO (blue line) and the requirement for LIGO-LF (black line). Custom tiltmeters can be used to improve aLIGO sensor noise below 0.5 Hz (blue dashed line). A novel 6D seismometer (red line) can surpass the requirement in the entire band.

in each arm. As a comparison, for aLIGO with the same amount of circulating power the numbers are $\Delta(\omega_+^2) = (2\pi \times 3.0 \text{ Hz})^2$ and $\Delta(\omega_-^2) = -(2\pi \times 0.64 \text{ Hz})^2$, respectively. We can further remove the radiation torque with the compensation technique we have discussed in Section 3.3.3 which injects approximately the same amount of sensing noise as the 1-Hz-bandwidth feedback control.

Now the question becomes how can we reduce the residual angular motion to $\lesssim 1$ nrad with a control bandwidth of only 1 Hz. We propose to achieve this by further suppress the motion of the optical benches.

Despite the sophistication of LIGO's seismic isolation [15, 16, 17], it does not significantly reduce the microseismic motion at $\sim$0.2 Hz. This is due to tilt-to-horizontal coupling [59, 60, 61], which causes the noise of the aLIGO inertial sensors to grow as $1/f^4$ at low frequencies as shown in Fig. 5-2. To reduce the bandwidth of the angular controls to 1 Hz, the tilt motion needs to be suppressed to 10^{-10} rad/$\sqrt{\text{Hz}}$ in the 0.01-0.5 Hz band. The corresponding horizontal sensitivity is shown in Fig. 5-2. Above 1 Hz we require an improved sensitivity to reduce the direct coupling of the ground motion.

There are two approaches to reach the required sensitivity of the inertial seismic sensors. The first one is to actively stabilize the tilt motion using custom-built tilt-meters [62, 63], which can achieve the requirement below 0.5 Hz. The second approach uses a novel 6D seismometer [64]. In the core of this instrument is a quasimonolithically suspended [65] mass whose position is monitored using an interferometric readout. Figure 5-2 shows that the design performance of the 6D seismometer satisfies the requirement in the entire band.

In Figure 5-3 we compare the residual pitch motion for aLIGO and LIGO-LF after the alignment control is engaged; the yaw motion is similar at high frequencies and is significantly less than pitch below 1 Hz, so the low frequency rms requirement for yaw is less critical. The control bandwidth is set to be 3 Hz and 1 Hz for LIGO-LF[2]. In the calculation for aLIGO, we use the measured ground motion and shadow sensor noise to represent the contributions due to seismic and due to suspension damping, respectively. For LIGO-LF, we adopt the required sensor noise (the black trace in Figure 5-2) for the residual seismic motion, and scale the shadow sensor noise of aLIGO down by a factor of 100 for the damping noise. Therefore our results here should be interpreted as the requirement set for the future seismic and damping sensors. The sensing noise from the wave-front sensors is assumed to be 5×10^{-15} rad/$\sqrt{\text{Hz}}$ for both aLIGO and LIGO-LF. For LIGO-LF we also include the contribution to the sensing noise from the radiation pressure compensation path. Also shown in the red curve as a comparison is the equivalent quantum noise: with 1 mm of spot mis-centering, an angular fluctuation per test mass given by the red curve will be converted to a length noise equal to the LIGO-LF's quantum limit.

The coupling of the longitudinal motion of the signal recycling cavity contaminates aLIGO's sensitivity in the 10-50 Hz band [21]. This coupling is proportional to the arm detuning [4] introduced to enable the dc readout of the GW signal [3]. For LIGO-LF, we assume balanced-homodyne readout [8] will be implemented instead, which

---

[2]Here we have assumed a controller with $1/f$ shape around the unity-gain frequency. We then add high-frequency cutoff filters while keeping the phase margin to be at least 30°. The optimal control design is not used here. Therefore Figure 5-3 serve as a conservative estimation of the alignment noise.
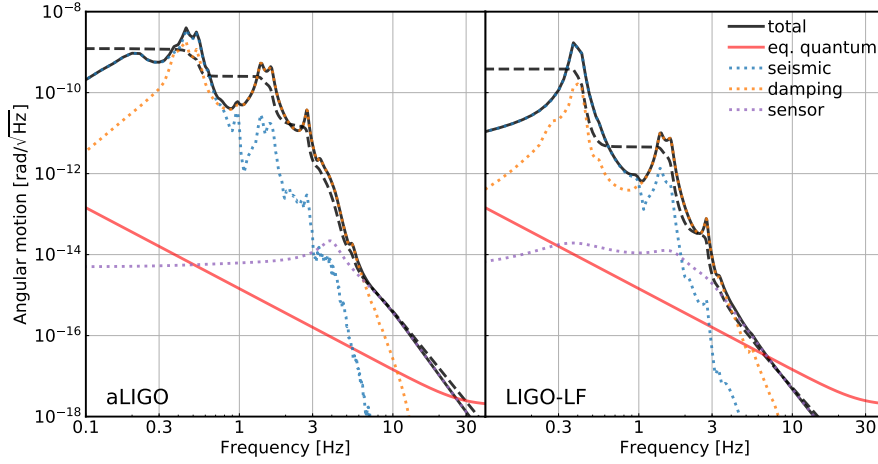
Figure 5-3: The residual pitch motion of aLIGO (left panel) and LIGO-LF (right panel). The black-solid curves are the total angular motion and the black-dashed ones are the corresponding cumulative rms values. The dotted curves are the noise contributions due to seismic (blue), suspension damping (orange), and wave-front sensing (purple), respectively. The red-solid curve is shown for comparison; it corresponds to a noise level equivalent to the LIGO-LF's quantum noise if the spot mis-centering is 1 mm.

essentially eliminates the coupling.

In aLIGO, high-quality-factor suspension resonances are damped using shadow sensors [19] with a sensitivity of 2×10^{-10} m/$\sqrt{\text{Hz}}$. A global control scheme has been proposed [66] to reduce its direct coupling to the GW output. However, this noise still enters the auxiliary loops and couples to the GW output indirectly. This calls for an improvement of the sensor noise by a factor of 100. Interferometric sensors [67] are promising candidates and are used in the LIGO-LF design.

Once technical noises are suppressed, LIGO-LF sensitivity will be limited by quantum and thermal noises. Our strategy to improve the fundamental limits is similar to the Strawman Team Red design [68].

Quantum noise [69, 70, 7] manifests both as sensor shot noise and as displacement noise by exerting quantum radiation pressure (QRP) forces on the test masses. LIGO-LF will operate under "resonant-sideband extraction" [5] with the same amount of power circulating in the arms as aLIGO. A signal recycling mirror transmissivity of

0.25 is chosen to optimize the broadband sensitivity.

The quantum noise can be further reduced with squeezed light [71, 72, 73]. Here we assume a frequency-dependent squeezing [74, 75, 76, 77] that provides 3 dB reduction of the QRP and 6 dB of the shot noise. Relative to aLIGO, QRP is further suppressed by the heavier test masses mentioned above.

Thermal noise [78] from the suspension [79, 65] and the optical coatings [80, 81, 82, 83, 7] dominates the sensitivity from 5 to 100 Hz. Suspension thermal noise can be lowered by doubling the length of the last suspension stage to $1.2\,\text{m}$ [84, 85] and by applying more sophisticated surface treatments [86]. LIGO-LF's penultimate masses will also need to be suspended with fused silica fibers to avoid excess noise. Furthermore, the vertical suspension resonance can be shifted down to $4.3\,\text{Hz}$ by increasing the fiber tension to 1.7 GPa. Overall, a factor of 5 improvement over aLIGO suspension thermal noise is possible (details of the LIGO-LF suspension are available in Appendix A.1).

The larger test masses and better seismic isolation open up the possibility of increasing spot sizes on the test masses by 50%, with a corresponding reduction in the coating thermal noise. Furthermore, a factor of 2 improvement in the coating loss angle is expected by the time of LIGO-LF [87].

Further sensitivity improvement below 30 Hz is limited by gravity gradient noise [88, 89, 90, 91, 92]. It can be mitigated with offline regression [93], and in our calculation we assume a factor of 10 cancellation [57]. The residual is combined with the residual seismic motion in Figure 5-1 under the label "seismic".

Scattering is another critical noise source below 30 Hz [94, 95, 58]. A small amount of light can scatter off the test masses due to surface imperfections, hit the baffles along the beam tubes, and finally recombine with the main beam. These stray photons induce differential power fluctuations which perturb the test masses via radiation pressure. In Figure 5-1, we present a scattering noise curve estimated from the typical ground motion at the LIGO sites with an anticipated 50% improvement in the mirror surface quality relative to aLIGO. As the relative displacement between the test mass and the tube is comparable to the laser wavelength (1 μm), the coupling can become

nonlinear, up-converting the baffle motion below 0.4 Hz up to 5 Hz [96, 21] . For rare cases where the ground motion is severe, an up-conversion shelf can form [58] and limit the low-frequency sensitivity. The antireflection surfaces along the optical path also create scattering noise. To suppress it, baffles should be constructed to block 99.9% of the stray light (details available in Appendix A.2).

In summary, the key LIGO-LF advancements consist of low-noise, interferometric sensors for seismic isolation and suspension damping, and heavy test masses with large spot sizes for improving the fundamental limits. The LIGO-LF suspension system is also redesigned. Combined with the squeezed light, balanced-homodyne readout, and low-loss coating that are planned for A+, the upgrades lead to the final LIGO-LF sensitivity.

5.3   Astrophysical applications.

LIGO-LF can deliver a rich array of science in astrophysics. Here we consider three examples: (i) binary BHs, including the expected range of detectability and detection rate, and parameter estimation of events, (ii) binary NSs, focusing on the source localization and the detectability of the tidal excitation of NS r-modes, and (iii) the GW memory effect. The searches for the stochastic GW background [97] and the continuous GW [98] rely mostly on the instrument's high-frequency performance, and are not enhanced by LIGO-LF.

5.3.1   Binary BHs.

Detectability.

With the LIGO-LF upgrade, both the maximum detectable distance and mass and the number of detections are larger than with aLIGO and A+, as illustrated in Figure 5-4. In the left, we plot the single-detector horizon and range [99] (in both redshift z and luminosity distance D_L) for binaries with different total masses M_{tot}. The systems are assumed to be nonspinning and to have equal masses. A single LIGO-LF
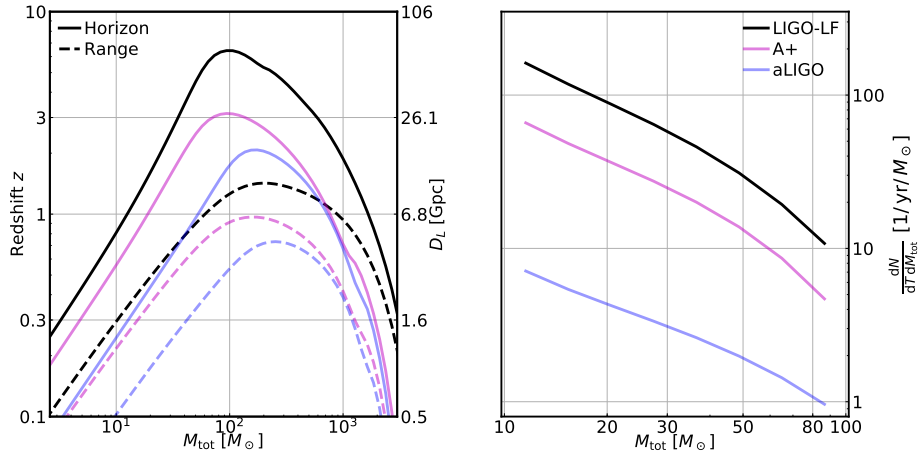
Figure 5-4: Left: The horizon (solid line) and range (dashed line) for binaries with different (source-frame) total masses. A single LIGO-LF may reach a cosmological redshift of $z \simeq 6$. Right: Expected detections rate of coalescing stellar-mass BH binaries as a function of the total mass. We marginalize over the mass ratio in the plot. LIGO-LF can detect ~ 3600 events per year, 18 times more than the expected number for aLIGO. All the numbers are calculated assuming a single detector.

could detect binary BHs to cosmological distances ($z \simeq 6$), whereas a network of four detectors would observe to $z \sim 10$, potentially accessing the first generation of stellar BHs [100].

The detection range allows us to estimate the detection rate. To proceed, we adopt the standard power-law mass distribution used in LIGO event rate estimation [40]. The probability densities of the primary mass M_1 and the secondary mass M_2 are respectively given by

$$\mathcal{P}_1(M_1) = \mathcal{A}_{M_1} M_1^{-\alpha} \Theta\left(M_1 - M_{\text{gap}}\right) \exp\left(-\frac{M_1}{M_{\text{cap}}}\right), \qquad (5.2)$$

$$\mathcal{P}_2(M_2) = \mathcal{A}_{M_2} \Theta\left(M_2 - M_{\text{gap}}\right) \Theta\left(M_1 - M_2\right), \qquad (5.3)$$

where $\mathcal{A}_{M_1}$ and $\mathcal{A}_{M_2}$ are overall normalizations, and Θ denotes the Heaviside step function. Following the convention we use a slope of $\alpha = 2.35$ and a lower limit of the mass distribution $M_{\text{gap}} = 5\ M_\odot$. As in Ref. [101], we have an exponential cutoff on M_1 which is set to $M_{\text{cap}} = 60\ M_\odot$. Additionally we require $M_1 + M_2 \leq 100\ M_\odot$. We

123

do not consider the IMBHs in our rate calculation because of the large uncertainty in their formation; they are sufficiently rare and are thus unlikely to affect the total number of detections. For the merging rate, we adopt a simple, mass-independent approximation [101]

$$\mathcal{R}(z) = 97(1+z)^2 \text{ Gpc}^{-3} \text{yr}^{-1}. \tag{5.4}$$

The expected number of detection per unit time dT in the mass interval $[M_{\text{tot}}, M_{\text{tot}} + dM_{\text{tot}}]$ is given by

$$
\begin{aligned}
\frac{dN\,(M_{\text{tot}})}{dTdM_{\text{tot}}} &= 4\pi \int_{M_{\text{tot}}/2}^{M_{\text{tot}}} dM_1 \mathcal{P}_1\,(M_1)\,\mathcal{P}_2\,(M_{\text{tot}} - M_1) \\
&\times \int_0^{z_{\text{ran}}(M_1, M_{\text{tot}} - M_1)} \frac{c\chi(z)^2 \mathcal{R}(z)}{(1+z)H(z)} dz,
\end{aligned}
\tag{5.5}
$$

where $z_{\text{ran}}(M_1, M_2)$ is the detection range for a binary system with M_1 and M_2, $\chi(z)$ the radial comoving distance, and $H(z)$ the Hubble parameter. In the calculation we have assumed a flat universe with Hubble constant $H_0 = 67 \text{ km s}^{-1} \text{Mpc}^{-1}$ and matter (dark energy) fraction of $\Omega_m = 0.32$ ($\Omega_\Lambda = 0.68$), consistent with the Planck result [102]. The $z_{\text{ran}}(M_1, M_2)$ is calculated with a single detector when we do the rate estimation. This is because we would like to focus on the improvements due to better sensitivity, instead of due to more detectors or more optimized network configuration.

The result is shown in the right panel of Figure 5-4. If we integrate over M_{tot}, we find a single LIGO-LF instrument will enable the detection of ~ 3600 stellar mass BH binaries per year. As a comparison, a single aLIGO (A+) can detect only about $\sim 200(1600)$ mergers in the same observational length. Note that the number of detections N yields a Poisson distribution, with a statistical uncertainty of $\sqrt{N}$. Therefore the statistical SNR grows as $\sqrt{N}$, illustrating LIGO-LF's greatly enhanced ability to constrain the population properties of binary BHs relative to aLIGO. Consider a simple case where the merging rate $\mathcal{R}$ is the only unknown, then with LIGO-LF we would be able to constrain it to within $\pm 0.5 \text{ Gpc}^{-3} \text{yr}^{-1}$ for a total observational period of 10-year, 4 times better than what aLIGO can achieve. As $\mathcal{R}$ is sensitive to, e.g., the metallicity at the time of binary formation [103], an accurate measurement

of $\mathcal{R}$ thus constrains the metal enrichment history of the Universe. Furthermore, the event rate per mass interval can also be used to place constraints on the fraction of dark matter in the Universe that is in the form of primordial BHs [104, 101].

Parameter estimation.

Moreover, LIGO-LF enables a more accurate parameter estimation than aLIGO. To emphasize the improved low-frequency sensitivity, we consider binaries with detector-frame total mass $M_{\mathrm{tot}}^{(\mathrm{d})} \geq 100 \ M_\odot$. Since the sensitivity of A+ and aLIGO is similar below 20 Hz, we consider the comparison between LIGO-LF and aLIGO. Qualitatively, the improvements are due to two facts: A more total SNR is accumulated in LIGO-LF than in aLIGO, and the SNR starts to accumulate at lower frequencies. Thus, if aLIGO can measure only the merger-ringdown phase of a coalescence, with LIGO-LF we could access the inspiral phase as well, allowing for a more precise estimation of the component masses and spins.

To quantify these improvements, we simulate GW signals with the `IMRphenomPv2` waveform [105] and inject them to mock detector noise. We consider five total mass bins from 100 $M_\odot$ to 2000 $M_\odot$, each with three spin configurations: $(\chi_{\mathrm{eff}} = \chi_{\mathrm{p}} = 0)$, $(\chi_{\mathrm{eff}} = 0.5, \chi_{\mathrm{p}} = 0.6)$, and $(\chi_{\mathrm{eff}} = -0.5, \chi_{\mathrm{p}} = 0.6)$. Here χ_{eff} is the mass-weighted sum of component spins along the orbital angular momentum [106, 107], and χ_{p} captures the precessing components [108]. The effect of the mass ratio has been studied in Refs. [47, 48], so we focus on the equal mass case.

We consider a four-detector network formed by the Hanford (H) and the Livingston (L) sites, LIGO-India (I), and aVirgo (V). For HLI, we consider both the LIGO-LF and aLIGO sensitivities; for V, we fix it at its design sensitivity [43]. KAGRA [109] is not included as it is less sensitive to IMBHs. For each source, the inclination is fixed to 30° and the distance is chosen such that the network SNR is 16 with aLIGO's sensitivity. We then use the `LALInference` [110] to get posterior distributions of source parameters. The parameter estimation results refer to the detector frame and we denote them with a superscript 'd'.

In Figure 5-5, we plot the 90% credible intervals of the chirp mass $\mathcal{M}_c^{(\mathrm{d})}$, total
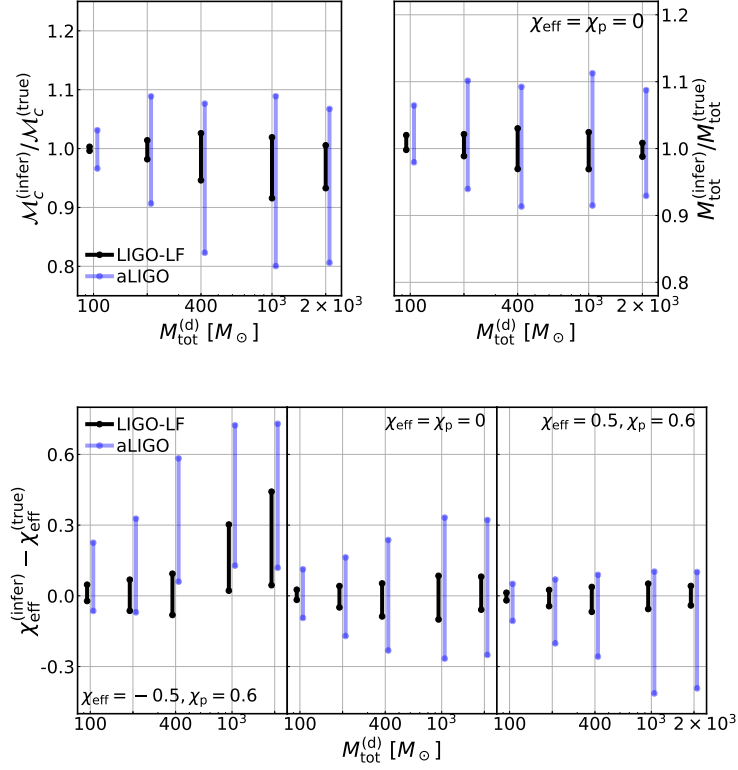
Figure 5-5: The 90% credible intervals of the detector-frame chirp mass $\mathcal{M}_c^{(\mathrm{d})}$ (top left), total mass $M_{\mathrm{tot}}^{(\mathrm{d})}$ (top right), and effective spin χ_{eff} (bottom) are all significantly smaller for LIGO-LF than for aLIGO. LIGO-LF also reduces biases, especially for $\mathcal{M}_c^{(d)}$ and χ_{eff} when the spin is antialigned (bottom left).
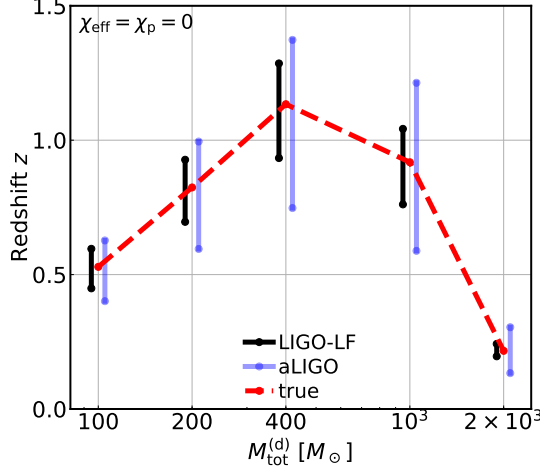
Figure 5-6: Mock sources for each total mass were placed at the redshifts indicated by the red-dashed line. The redshifts were chosen to give a network SNR of 16 in aLIGO. The black (blue) bars indicate the 90% credible interval for the inferred redshift with LIGO-LF (aLIGO) sensitivity. LIGO-LF typically improves the constrain in z by a factor of 2.

mass $M_{\mathrm{tot}}^{(\mathrm{d})}$, and χ_{eff}. For the masses, we present the results for the nonspinning case. When spins are included, an aligned (antialigned) spin tends to improve (degrade) the inference accuracy [111]. Similar effects can also be seen in the posterior distributions of χ_{eff}, as illustrated in the bottom panels. The precession term χ_{p} cannot be well constrained even with LIGO-LF.

To obtain the source-frame masses, the value of inferred redshift is required [50]. The conversion is

$$\mathcal{M}_c = \frac{\mathcal{M}_c^{(\mathrm{d})}}{1+z} \tag{5.6}$$

for the chirp mass $\mathcal{M}_c$, and similarly for the total mass M_{tot}.

In Figure 5-6 we present the 90% credible intervals of the redshift z. To yield a network SNR of 16 with aLIGO design sensitivity, the redshifts are $z = (0.53, \ 0.82, \ 1.1, \ 0.92, \ 0.22)$ for the 5 injections we have with $M_{\mathrm{tot}}^{(\mathrm{d})} = (100, \ 200, \ 400, \ 1000, \ 2000) \ M_\odot$, respectively. LIGO-LF typically improves the accuracy in the redshift inference by a factor of 2 relative to aLIGO.

We show the 90% credible intervals of the source-frame masses in Figure 5-7. The
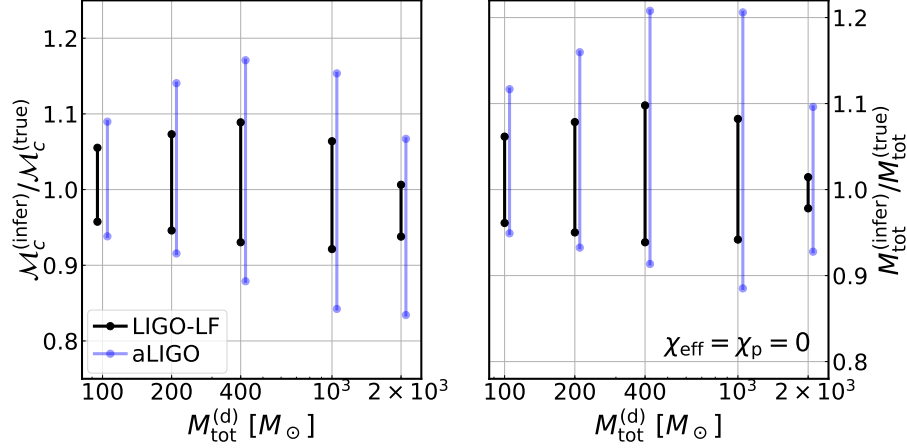
Figure 5-7: The 90% credible interval of the source-frame chirp mass $\mathcal{M}_c$ (left panel) and total mass M_{tot} (right panel). The uncertainty is about a factor of 2 smaller for LIGO-LF compared to aLIGO, and is dominated by the uncertainty in inferring the redshift.

injected source-frame total masses are $M_{\text{tot}} = (65, 109, 187, 521, 1644)$ $M_\odot$, and chirp masses $\mathcal{M}_c = (28, 48, 82, 227, 716)$ $M_\odot$. Due to the statistical error in measuring the redshift, LIGO-LF only constrains the source-frame values 2 times better than aLIGO.

The effective spin, nonetheless, is unaffected by the redshift and thus LIGO-LF can achieve 3-5 times better accuracy than aLIGO, which will be essential for discriminating between different formation scenarios that predict different spin configurations [112, 113].

5.3.2 Binary NSs.

Localization.

We use the Fisher matrix to examine LIGO-LF's ability to localize a binary NS including effects of Earth's rotation. We consider the same HLIV network as in the PE section. The coordinates of HLV can be found in Ref. [114], and we use the same location for I as in Ref. [115].

The data seen in the ith detector in the network can be written as [116, 117]

$$d_i(f) = \left[F_i^+(f)h_+(f) + F_i^\times(f)h_\times(f) \right] \exp\left[-\mathrm{i}2\pi f\tau_i(f) \right], \tag{5.7}$$

where $h_{+(\times)}$ is the GW signal in the plus (cross) polarization, $F_{+(\times)}$ the antenna response whose functional form is provided in [114], and τ_i the traveling time from the coordinate origin to the ith detector. The frequency dependences of $F_{+(\times)}$ and τ_i originate from the rotation of the Earth, and with the stationary-phase approximation they can be written as,

$$F_{+(\times)}(f) = F_{+(\times)}\left[t_f(f) \right], \tag{5.8}$$

$$\tau_i(f) = \tau_i\left[t_f(f) \right], \tag{5.9}$$

$$t_f = t_c - \frac{5}{256}\left(\frac{G\mathcal{M}_c}{c^3} \right)^{-5/3} (\pi f)^{-8/3}. \tag{5.10}$$

Here t_c is the time of the coalescence. We compute the signal $h(f)$ using the post-Newtonian (PN) expansion, including phase corrections to the 1.5 PN order.

We parameterize the signal in terms of 9 parameters: $\boldsymbol{p} = (\mathcal{M}_c,\ q,\ t_c,\ \phi_c,\ \iota,\ \theta_s,\ \phi_s,\ \psi_s,\ d_\mathrm{L})$, corresponding to the chirp mass, mass ratio (≤ 1), time and phase at the merger, the source's inclination, declination, right ascension, polarization, and luminosity distance. The spin is not included since the NS is expected to be slow spinning [51, 118]. The statistical error of each parameter can be estimated using the Fisher matrix with element

$$\Gamma_{jk} = \left\langle \frac{\partial \boldsymbol{d}}{\partial p_j}, \frac{\partial \boldsymbol{d}}{\partial p_k} \right\rangle, \tag{5.11}$$

where the inner product for data from the network, $\boldsymbol{a}$ and $\boldsymbol{b}$, is defined as

$$\langle \boldsymbol{a}, \boldsymbol{b} \rangle (f_\mathrm{up}) = 2 \sum_i^\mathrm{HLIV} \int_0^{f_\mathrm{up}} \mathrm{d}f \left[\frac{a_i^*(f)b_i(f) + a_i(f)b_i^*(f)}{S_i(f)} \right]. \tag{5.12}$$

Here $S_i(f)$ is the noise power spectra density of the ith detector, $f_\mathrm{up} \leq 2f_\mathrm{ISCO}$ is the upper limit of the integration, and f_ISCO is the orbital frequency at the system's inner-most stable circular orbit (ISCO). We have treated f_up as a free parameter so

that we can consider the cumulative accuracy using only data with $f < f_{\rm up}$,

The full covariance matrix $\boldsymbol{\Sigma}$ can be obtained by inverting $\boldsymbol{\Gamma}$,

$$\boldsymbol{\Sigma} = \boldsymbol{\Gamma}^{-1}, \tag{5.13}$$

and the statistical error for the jth parameter p_j is given by

$$\Delta p_j = \sqrt{\Sigma_{jj}}. \tag{5.14}$$

We are especially interested in the uncertainty solid angle covering the source's location, which is given by

$$\Delta\Omega_s = 2\pi |\sin\theta_s| \sqrt{\langle\Delta\theta_s^2\rangle\,\langle\Delta\phi_s^2\rangle - \langle\Delta\theta_s\Delta\phi_s\rangle^2}. \tag{5.15}$$

In order to demonstrate the improvement made by LIGO-LF over aLIGO and A+, we focus on 1.4 $M_\odot$-1.4 $M_\odot$ NS binaries, and fix the source location to the Coma cluster. We consider two inclination angles, a face-on one with $\iota = 30°$, and a more edge-on one with $\iota = 75°$. The arriving time and polarization of the sources are marginalized over. The result is shown in Figure 5-8. Here we plot the cumulative localization error, $\Delta\Omega_s(f_{\rm up})$ as a function of $f_{\rm up}$. In other words, instead of integrating equation (5.12) over the entire signal band, we integrate it only up to $f_{\rm up}$. We can thus know the localization accuracy at each instant of the inspiral. As shown in the figure, LIFO-LF localize the source 5 (10) times better than A+ (aLIGO) at 30 Hz, and 10 (15) times better at 20 Hz. Note that the time prior the final merger increases sharply as the frequency decreases, as

$$t_c - t_f = 54 \left(\frac{\mathcal{M}_c}{1.2\,M_\odot}\right)^{-5/3} \left(\frac{f}{30\,{\rm Hz}}\right)^{-8/3}\,{\rm s}. \tag{5.16}$$

Despite that the final uncertainties are similar for A+ and for LIGO-LF, LIGO-LF would be able to send out the source location minutes before the final merger, while for A+ similar accuracy cannot be achieved until seconds before the merger.
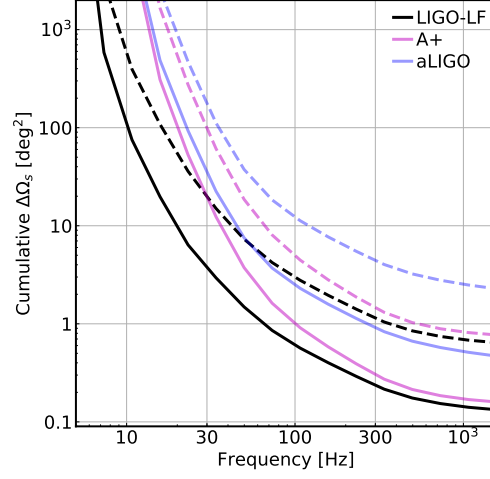
Figure 5-8: The cumulative uncertainty in localization, $\Delta\Omega_s$, for the HLIV network. We consider NS binaries at the Coma cluster with two inclinations, 30° (solid line) and 75° (dashed line), and marginalize over the polarization and time of arrival. LIGO-LF improves the localization accuracy by a factor of 5 over A+ using only the sub-30 Hz data.

This illustrates LIGO-LF's ability to achieve a more timely localization than A+ and aLIGO.

NS r-modes.

The (linear) tidal response of the NS can be decomposed into an equilibrium tide and a dynamical tide. The equilibrium tide accounts for the quasi-static, large-scale distortion of the star and the dynamical tide [119, 120] accounts for the internal modes of oscillation which can be resonantly excited as the orbit decays and sweeps up in frequency. Here we consider the excitation of the NS's rotational modes (i.e. the r-modes) due to its companion's gravitomagnetic tidal field [121]. We focuse on the detectability of the $l = 2$, $m = 1$ r-mode which does not require misalignment between the NS spin and the orbital angular momentum. The GW frequency of mode resonance f_r is related to the NS's spin frequency f_{spin} as

$$f_r = \frac{4}{3} f_{\text{spin}}. \tag{5.17}$$

131

Since the NSs in binary NS systems are expected to be slow-spinning (with a rate less than a few×10 Hz), the r-mode is naturally an interesting science case for the LIGO-LF upgrade.

The tidal interaction induces a phase shift, $\delta\Phi_r$, relative to the point-particle (pp) GW waveform. As the duration of the mode resonance is typically $\sim 1\%$ of the total GW decay timescale [121], the resonance can thus be treated as an instantaneous process. In this limit, the phase of the frequency-domain waveform $\Psi(f)$ can be written as [122]

$$\Psi(f) = \Psi_{\rm pp}(f) - \left(1 - \frac{f}{f_r}\right) \delta\Phi_r \Theta\left(f_r - f\right), \tag{5.18}$$

where $\Psi_{\rm pp}$ is the phase of the point particle waveform (calculated to the 1.5 PN order in our study). In the expression above we have aligned the tidal waveform to the pp one at the merger.

While in the case of equilibrium tides the orbital energy is absorbed by the star and thus the inspiral is accelerated, in the case of the r-mode interaction the direction of energy transfer is reversed. The orbit extracts the NS spin energy which decelerates the inspiral. This unique feature of the r-mode corresponds to a *negative* $\delta\Phi_r$ in the expression above. While large theoretical uncertainties exist, previous work suggests that [121]

$$\delta\Phi_r \sim -0.1 \left(\frac{f_{\rm spin}}{100\,{\rm Hz}}\right)^{2/3}. \tag{5.19}$$

To estimate the detectability of this effect, we once again use the Fisher matrix method. A fully Bayesian analysis is deferred to future studies. For simplicity, we focus on the single-detector case and fix the sources at 50 Mpc with optimal orientation. This allows us to write the waveform in terms of 9 parameters, $(\mathcal{M}_c,\ q,\ \chi_1,\ \chi_2,\ t_c,\ \phi_c,\ d_{\rm L},\ f_r,\ \delta\Phi_r)$, corresponding to the chirp mass, mass ratio, dimensionless spin of mass 1 and 2, time and phase at the coalescence, luminosity distance, and the resonant frequency and the phase shift of the r-mode. The equilibrium tidal deformation is not included here because it is only relevant at $f \gtrsim 600\,{\rm Hz}$ [123]. We consider here binaries with $M_1 = 1.4\,M_\odot$ and $M_2 = 1.35\,M_\odot$. The mass ratio is slightly off 1 because otherwise χ_1 and χ_2 will be completely degenerate. The relation

between the spin frequency f_{spin} and the dimensionless spin parameter χ depends on the NS equation of state. Here we pick the SLy equation of state [124] as a typical representation; this equation of state is consistent with the GW170817 event [51]. It leads to

$$\chi \simeq 0.06 \left(\frac{f_{\mathrm{spin}}}{100\,\mathrm{Hz}} \right), \tag{5.20}$$

for a typical 1.4 $M_\odot$ NS. A softer equation of state yields a larger χ for a NS with fixed mass. We then vary the spins of the two masses simultaneously (i.e., $f_{\mathrm{spin1}} = f_{\mathrm{spin2}} = f_{\mathrm{spin}}$), and evaluate the Fisher matrix at different values of f_{spin} to obtain the uncertainty on the phase shift, $\Delta\left(\delta\Phi_r\right)$.

The results are shown in Figure 5-9. The r-mode is detectable if the statistical error is smaller than the real phase shift calculated from equation (5.19), i.e., we set $\Delta\left(\delta\Phi_r\right) \leq |\delta\Phi_r|$ as the detectability threshold[3]. We find that if the NS spins at a rate greater than 35 Hz (which is approximately the rate of the fastest rotating pulsar in a binary NS system known today [118] when it enters the sensitivity band of a ground-based GW detector), a single LIGO-LF may detect the r-mode resonance up to a distance of 50 Mpc. Since the phase shift of the $l = 2$, $m=1$ r-mode depends on the NS stratification, which is sensitive to the internal composition and the state of matter [125, 122], a detection may thus place constraints on the NS equation of state from physics beyond the star's bulk properties [126]. Furthermore, the r-mode resonance provides an independent measurement of the NS spin, which may help break the spin-mass ratio degeneracy [50] and improve the accuracy in measuring the (equilibrium) tidal deformability [123, 51].

---

[3]Note that we included only a single set of $(f_r, \delta\Phi_r)$ in equation 5.19, whereas in a merging binary NS system each NS should contribute individually a r-mode phase shift. Nevertheless, the typical uncertainty of the resonant frequency is $\Delta f_r \simeq 50$ Hz, corresponding to a resolution in the spin frequency of $\Delta f_{\mathrm{spin}} \simeq 40$ Hz $> f_{\mathrm{spin}}$. We are thus unlikely to resolve the individual resonance but only the combined effect of the two NSs. Therefore we included an extra factor of 2 when computing the theoretical prediction (the red-dashed curve in Figure 5-9) according to equation (5.19).
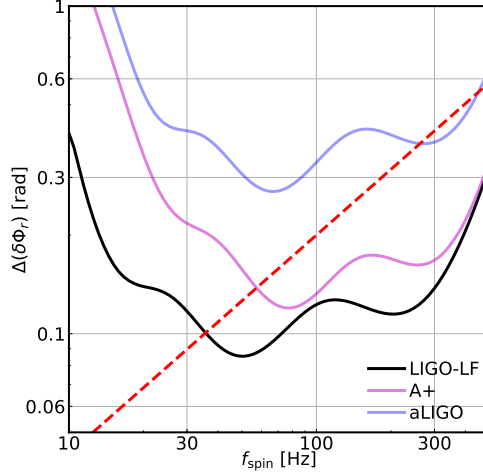
Figure 5-9: The uncertainty (solid lines) in measuring the phase shift due to resonant excitation of the NS r-mode $\delta\Phi_r$ as a function of the NS spin frequency f_{spin}. We consider the single detector case and fix the sources at $50\,\mathrm{Mpc}$ with optimal orientation. Also shown in the red dashed line is the expected magnitude of the real r-mode phase shift $|\delta\Phi_r|$. The effect is detectable when the real phase shift is greater than the statistical error.

5.3.3   The GW memory.

The GW memory causes a DC displacement of the test masses that persists after the GW has passed [127]. As the effect builds up over a finite amount of time, it can thus be detected by a LIGO-like GW detector which effectively high-passes the signal. The detection of this effect may provide a strong-field test of the general theory of relativity. Therefore we consider it as one of the science cases for LIGO-LF.

Here we adopt the minimal-waveform model proposed in Ref. [128],

$$h_+^{(\mathrm{mem})}(f) = \frac{G\eta M_{\mathrm{tot}}/c^2}{384\pi D_{\mathrm{L}}} \sin^2\iota \left(17 + \cos^2\iota\right) h^{(\mathrm{mem})}(f), \qquad (5.21)$$

where $\eta = M_1 M_2/M_{\mathrm{tot}}^2$ is the symmetric mass ratio, and $h_\times^{(\mathrm{mem})}(f) = 0$. The term

$h^{(\mathrm{mem})}(f)$ is further given by

$$h^{(\mathrm{mem})}(f) = \frac{\mathrm{i}}{2\pi f} \left\{ \frac{8\pi G M_{\mathrm{tot}}}{c^2 r_{\mathrm{m}}} \left[1 - 2\pi \mathrm{i} f \tau_{\mathrm{rr}} U(1, 7/4, 2\pi \mathrm{i} f \tau_{\mathrm{rr}}) \right] \right.$$
$$\left. - \frac{c^3}{G\eta M_{\mathrm{tot}}} \sum_{n,n'}^{n_{\max}} \frac{\sigma_{22n} \sigma_{22n'}^* A_{22n} A_{22n'}^*}{2\pi \mathrm{i} f - (\sigma_{22n} + \sigma_{22n'}^*)} \right\}. \tag{5.22}$$

The value of $\tau_{\mathrm{rr}} = (5/256)\,(GM_{\mathrm{tot}}/c^3\eta)\,(c^2 r_m/GM_{\mathrm{tot}})^4$ is the characteristic orbital decay time scale at r, and U is Kummer's confluent hypergeometric function of the second kind. The σ_{lmn} are angular frequencies of the final BH's quasi-normal modes, whose value are given in Ref. [129]. The coefficients of A_{lmn} can be solved by matching the leading order quadrupole moments in the inspiral phase to the sum of the ringdown normal modes at r_{m}. Here we choose r_{m} to correspond to the orbital separation at the ISCO.

In our calculation we consider a simple case where we fix the source distance to $z = 0.1$ ($D_{\mathrm{L}} = 0.48$ Gpc) and inclination to $\iota = 30°$. We further assume that the signal is purely in the "+" polarization. We then vary the source-frame total mass (while keeping the mass ratio to 1) and compute the single-detector matched-filter SNR for each source with different detector sensitivities.

The result is shown in Figure 5-10. LIGO-LF increases the peak SNR by a factor of 4 relative to aLIGO. While it may still be challenging to detect the effect from a single event, LIGO-LF nonetheless has a promising future in detecting this event via event-stacking. As suggest in Ref. [130], aLIGO will need ~ 90 GW150914-like [131] events to be able to achieve a SNR of 5 detection of the memory effect. Accumulating these many events will require aLIGO to operate at full sensitivity for ~ 10 years (note that the detection rate calculations in Section 5.3.1 assumes an SNR lower limit of 8 or a range of $z \simeq 0.4$ for a 30 $M_\odot$-30 $M_\odot$ system; restricting to a range of within $z \lesssim 0.1$ will lower the detection rate by a factor of $\simeq 64$). For LIGO-LF, however, only ~ 25 events will be sufficient to reach a similar level of detection. As the detection rate of LIGO-LF also increased by a factor of almost 20 relative to aLIGO, it means within a few months of observation with LIGO-LF will be sufficient to achieve a high
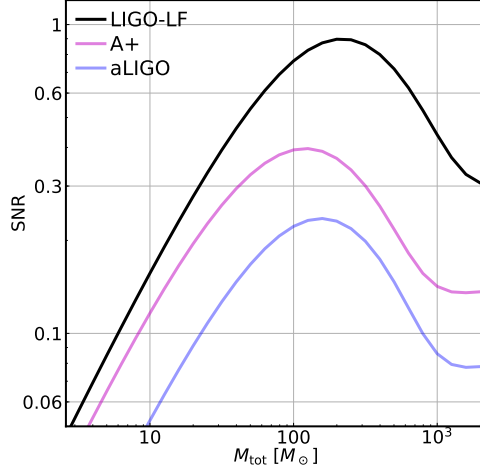
Figure 5-10: SNR from the GW memory effect as a function of the source-frame total mass. The sources are fixed at $z = 0.1$ and an inclination of 30°. The peak SNR seen in LIGO-LF is 4 (2) times greater than that seen in aLIGO (A+).

SNR (≥ 5) detection of the memory effect.

5.4   Conclusions.

In this Chapter we proposed LIGO-LF, an upgrade improving aLIGO's low-frequency performance. With technologies currently under development, such as suspension systems with 200 kg test masses, interferometrically sensed seismometers, and balanced-homodyne readout, LIGO-LF can reach the fundamental limits set by quantum and thermal noises down to 5 Hz. These technologies are also directly applicable to the future generation of detectors. We went on to consider this upgrade's implications for the astrophysical output of an aLIGO-like detector. Comparing LIGO-LF to aLIGO, we found that the mass and spatial range of binary BHs detectable would be greatly enhanced, and the localization of NS binaries would be achieved at a much earlier time, enabling more timely follow-up.

Appendix A

Supplemental Materials for the LIGO-LF Design

A.1 LIGO-LF Suspension Design

LIGO-LF adopts a 4-stage suspension system similar to that of aLIGO [28]. The suspension chain consists of a top mass (TOP), an upper-intermediate mass (UIM), a penultimate mass (PUM), and a main test mass (TST), with the parameters for each stage summarized in Table A.1. The blade design used for LIGO-LF vertical support is similar to that of aLIGO. Two requirements are set for the system above 5 Hz: the suspension needs to provide sufficient filtering of the residual ground motion (cf. Figure 5-2), and its total thermal noise should be dominated by the pendulum mode from the TST stage.

To achieve the seismic isolation requirement, the mass ratio between the TOP and the TST stages should be similar to that of aLIGO. Decreasing the TOP mass

Table A.1: Summary of the LIGO-LF suspension parameters

Stage	mass [kg]	length [m]	Wire diameter [mm]	Material
TOP	80	0.32	1.8	C70 steel
UIM	80	0.32	1.2	C70 steel
PUM	200	0.36	1.2	Silica
TST	200	1.2	0.6 (thin); 1.8 (thick)	Silica
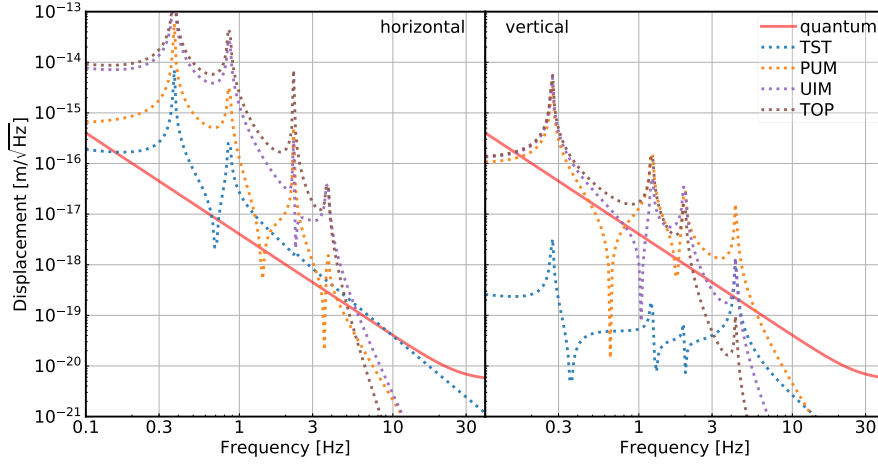
Figure A-1: The LIGO-LF suspension thermal noise from different stages (represented by dotted lines with different colors). The quantum noise is also plotted in the red-solid line as a reference. In the left we plot the direct horizontal (along the beam line) displacement noises. The dominant contribution above 5 Hz is from the last stage and it is similar to the quantum noise in the $5 - 20$ Hz band. In the right are the noises due to the vertical-to-horizontal coupling. The bounce mode is at 4.3 Hz, making the vertical contributions subdominant above 5 Hz.

shifts the highest suspension resonance to higher frequencies, making the pendulum filtering less efficient at 5 Hz. Consequently we choose $m_{\text{TOP}} = m_{\text{UIM}} = 80\,\text{kg}$, and the resultant seismic noise is shown in the dotted-brown curve of Figure 5-1.

In addition to the direct length coupling, the longitudinal ground motion can also couple to the pitch motion of the test mass. The main pitch resonance frequency can be controlled by tuning the distance between the fiber binding point and the mirror's center of mass. Similarly, the ground rotation can couple to the yaw motion of the test mass, and the resonance frequency can be controlled as well [18]. For LIGO-LF, the main pitch and yaw resonances are set to $0.42\,\text{Hz}$ and 0.35 Hz, respectively, to balance the requirements for more filtering at high frequency (> 5 Hz) and for less rms angular motions at low frequency (< 1 Hz).

We present the suspension thermal noise for LIGO-LF in Figure A-1. In the sensitivity band above 5 Hz, the dominant contribution comes from the pendulum mode of the test mass stage. In the calculation we have assumed an effective loss

angle of 5×10^{-10} [85] and the resultant suspension thermal noise is similar to the quantum noise from 5 to 20 Hz. In order to reduce the contamination from other stages, we replace the suspension for the PUM stage from C70 steel wire to silica fiber. Meanwhile, the wire stress in the TOP and UIM stages is increased by 30% relative to aLIGO for better dilution of the losses.

Besides the thermal motion along the beam line, the vertical vibration of the test masses also couples to the GW channel due to the Earth's radius of curvature. A conservative estimation of the vertical-to-horizontal cross coupling is 0.1% [65]. The eigenfrequency $f_{\rm v}$ of the last stage's vertical mode (also known as the "bounce mode") scales as [132]

$$2\pi f_{\rm v} \approx \sqrt{\frac{gY}{l\sigma} \frac{m_{\rm TST} + m_{\rm PUM}}{m_{\rm PUM}}}, \tag{A.1}$$

where g, Y, l, σ, $m_{\rm TST}$, and $m_{\rm PUM}$ are the local gravitational acceleration, the Young's modulus of the material, the length of the suspension, the stress inside the fiber, the mass of the test mass, and the mass of the penultimate mass, respectively. To make $f_{\rm v}$ low, we maintain the mass ratio between the PUM and the test mass to 1 as aLIGO, and double l to 1.2 m. Meanwhile, the fibers suspending the test mass have a tapered geometry: for the thick part where most of the bending energy is stored, it has a diameter of $1.8\,\mu$m to cancel the thermal-elastic noise, while the thin part has a diameter of 0.6 μm to increase the stress σ to 1.7 GPa. Consequently, the bounce mode has an eigenfrequency of $f_{\rm v} = 4.3$ Hz, which provides sufficient filtering of the vertical motion in the sensitivity band.

A.2 Calculation of the scattering noise

For the scattering noise calculation, we introduce the effective displacement $\bar{x}_{\rm scatter}$ defined as

$$\bar{x}_{\rm scatter}(t) = \frac{\lambda}{4\pi} \sin\left[\frac{4\pi}{\lambda} x_{\rm scatter}(t)\right], \tag{A.2}$$

where $x_{\rm scatter}(t)$ is the (physical) relative displacement between a mirror and a scattering surface at time t, and $\lambda = 1064\,$nm the laser wavelength. The corresponding
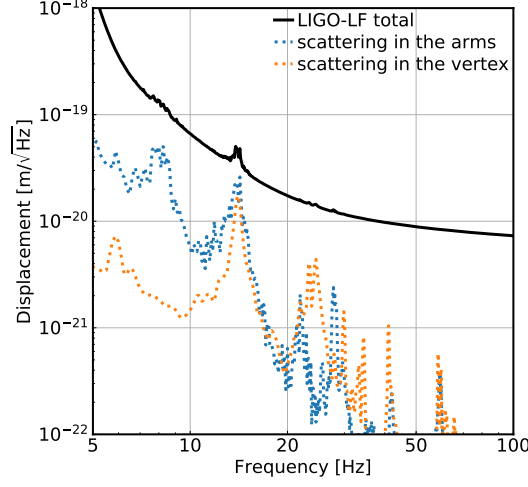
Figure A-2: The noises due to scattering in the arm tubes (dotted-blue) and in the vertex (dotted-orange). The total LIGO-LF noise is shown in the solid-black as a reference.

frequency-domain displacement is thus given by

$$\hat{\tilde{x}}_{\text{scatter}}(f) = \frac{\lambda}{4\pi} \int \sin\left[\frac{4\pi}{\lambda} x_{\text{scatter}}(t)\right] \exp\left(-2\pi \mathrm{i} f t\right) \mathrm{d}t. \tag{A.3}$$

Notice that when $x_{\text{scatter}} \sim \lambda$, the effective displacement no more varies linearly with the physical displacement. Consequently, the large ground motion below 1 Hz can be up-converted to the sensitivity band, making scattering a significant noise source when the ground motion is severe.

The olive trace in Figure 5-1 of the main Letter is calculated including two effects: scattering in the arm tubes, and scattering in the vertex of the interferometer, with each one's contribution individually shown in Figure A-2.

For the former, the calculation follows from Ref. [95]. There are two coupling channels need to be considered. The phase quadrature of the scattered light directly enters the GW readout, with a flat transfer function from $\hat{\tilde{x}}_{\text{scatter}}(f)$ to the differential arm displacement given by

$$Z_{\text{tube}}^{(\text{Im})}(f) \simeq 2.5 \times 10^{-12} \left(\frac{A_{\text{scat}}}{5.0 \times 10^{-12}}\right) \frac{\mathrm{m}}{\mathrm{m}}. \tag{A.4}$$

In the equation above A_{scat} is the amplitude scattering coefficient that is further defined as

$$A^2 = \left(\frac{\lambda}{L_{\text{mb}}}\right) \text{BRDF}_{\text{m}}^2 \text{BRDF}_{\text{b}} \Delta\Omega_{\text{b}}, \tag{A.5}$$

where L_{mb} is the distance between the mirror and baffle, $\Delta\Omega_{\text{b}}$ the solid angle subtended by the baffle, and $\text{BRDF}_{\text{m(b)}}$ the Bi-directional Reflectivity Distribution [94] of the mirror (baffle).

Meanwhile, the amplitude quadrature of the scattered light can beat with the static optical field inside each arm to cause a differential power fluctuation, which further induces differential arm motions due to the radiation pressure force. The transfer function for this mechanism is given by

$$Z_{\text{tube}}^{(\text{Re})}(f) \simeq 8.2 \times 10^{-12} \left(\frac{10\,\text{Hz}}{f}\right)^2 \left(\frac{A_{\text{scat}}}{5.0 \times 10^{-12}}\right)$$
$$\times \left(\frac{200\,\text{kg}}{m_{\text{TST}}}\right) \left(\frac{P_{\text{a}}}{0.8\,\text{MW}}\right) \left(\frac{T_{\text{s}}}{0.25}\right) \frac{\text{m}}{\text{m}}, \tag{A.6}$$

where P_{a} is the power circulating in each arm and T_{s} is the power transmissivity of the signal recycling mirror. Below $20\,\text{Hz}$, the amplitude quadrature dominates the coupling.

The scattering in the vertex is caused by the anti-reflecting (AR) surfaces along the optical path. If not properly baffled, the stray light may hit the chamber wall and be reflected back to the optical path. The coupling coefficient per stray beam is [133]

$$Z_{\text{vertex}}(f) \simeq 1.0 \times 10^{-12} \left(\frac{T_{\text{baffle}}}{0.001}\right)^{1/2} \left(\frac{R_{\text{AR}}}{250\,\text{ppm}}\right) \left(\frac{2\,\text{mm}}{w_{\text{wall}}}\right) \frac{\text{m}}{\text{m}}, \tag{A.7}$$

where R_{AR} is the power reflectivity of the AR surface creating the beam, w_{wall} is the stray light's spot size on the chamber wall, and T_{baffle} is the fraction (in power) of the stray light that leaks through the baffle. There are 10 AR surfaces that can contribute to this noise, 2 from the input test masses ($R_{\text{AR}} \simeq 250\,\text{ppm}$), 4 from the beam splitter ($R_{\text{AR}} \simeq 50\,\text{ppm}$), and 4 from the compensation plates ($R_{\text{AR}} \simeq 20\,\text{ppm}$). To achieve the proposed LIGO-LF sensitivity, the baffles need to reduce the power of

the stray light by

$$T_{\text{baffle}}^{\text{(LIGO--LF req.)}} < 0.1\%. \tag{A.8}$$

Bibliography

[1] H. Yu and et al., "Prospects for Detecting Gravitational Waves at 5 Hz with Ground-Based Detectors," *Physical Review Letters*, vol. 120, p. 141102, Apr. 2018.

[2] D. D. Brown and A. Freise, "Finesse," May 2014. You can download the binaries and source code at urlhttp://www.gwoptics.org/finesse.

[3] T. T. Fricke and et al., "DC readout experiment in Enhanced LIGO," *Classical and Quantum Gravity*, vol. 29, p. 065005, Mar. 2012.

[4] K. Izumi and D. Sigg, "Advanced ligo: length sensing and control in a dual recycled interferometric gravitational wave antenna," *Classical and Quantum Gravity*, vol. 34, no. 1, p. 015001, 2017.

[5] J. Mizuno, K. A. Strain, P. G. Nelson, J. M. Chen, R. Schilling, A. Rüdiger, W. Winkler, and K. Danzmann, "Resonant sideband extraction: a new configuration for interferometric gravitational wave detectors," Phys. Rev. A, vol. 175, pp. 273–276, Apr. 1993.

[6] E. D. Hall, *Long-Baseline Laser Interferometry for the Detection of Binary Black-Hole Mergers*. PhD thesis, California Institute of Technology, 2017.

[7] D. V. Martynov and et al., "Quantum correlation measurements in interferometric gravitational-wave detectors," Phys. Rev. A, vol. 95, p. 043831, Apr. 2017.

[8] P. Fritschel, M. Evans, and V. Frolov, "Balanced homodyne readout for quantum limited gravitational wave detectors," *Optics Express*, vol. 22, p. 4224, Feb. 2014.

[9] A. E. Siegman, *Lasers*. University Science Books, 1986.

[10] Y. Hefetz, N. Mavalvala, and D. Sigg, "Principles of calculating alignment signals in complex resonant optical interferometers," *J. Opt. Soc. Am. B*, vol. 14, pp. 1597–1606, Jul 1997.

[11] A. F. Brooks and et al., "Overview of advanced ligo adaptive optics," *Appl. Opt.*, vol. 55, pp. 8256–8265, Oct 2016.

[12] R. W. P. Drever, J. L. Hall, F. V. Kowalski, J. Hough, G. M. Ford, A. J. Munley, and H. Ward, "Laser phase and frequency stabilization using an optical resonator," *Applied Physics B*, vol. 31, pp. 97–105, Jun 1983.

[13] https://alog.ligo-wa.caltech.edu/aLOG/index.php?callRep=43574.

[14] K. Izumi, D. Sigg, and K. Kawabe, *Frequency Response of the aLIGO Interferometer: part3*. LIGO, 2015. LIGO Document T1500559-v3.

[15] F. Matichard and et al., "Seismic isolation of advanced ligo: Review of strategy, instrumentation and performance," *Classical and Quantum Gravity*, vol. 32, no. 18, p. 185003, 2015.

[16] F. Matichard and et al., "Advanced LIGO two-stage twelve-axis vibration isolation and positioning platform. part 1: Design and production overview," *Precision Engineering*, vol. 40, pp. 273 – 286, 2015.

[17] F. Matichard and et al., "Advanced LIGO two-stage twelve-axis vibration isolation and positioning platform. part 2: Experimental investigation and tests results," *Precision Engineering*, vol. 40, pp. 287 – 297, 2015.

[18] M. Rakhmanov, *Dynamics of laser interferometric gravitational wave detectors*. PhD thesis, CALIFORNIA INSTITUTE OF TECHNOLOGY, 2000.

[19] L. Carbone and et al., "Sensors and actuators for the advanced ligo mirror suspensions," *Classical and Quantum Gravity*, vol. 29, no. 11, p. 115005, 2012.

[20] https://alog.ligo-wa.caltech.edu/aLOG/index.php?callRep=46178.

[21] D. V. Martynov and et al., "Sensitivity of the Advanced LIGO detectors at the beginning of gravitational wave astronomy," Phys. Rev. D, vol. 93, p. 112004, June 2016.

[22] L. Barsotti, M. Evans, and P. Fritschel, "Alignment sensing and control in advanced LIGO," *Classical and Quantum Gravity*, vol. 27, p. 084026, Apr. 2010.

[23] J. A. Sidles and D. Sigg, "Optical torques in suspended fabryâĂŞperot interferometers," *Physics Letters A*, vol. 354, no. 3, pp. 167 – 172, 2006.

[24] E. Hirose, K. Kawabe, D. Sigg, R. Adhikari, and P. R. Saulson, "Angular instability due to radiation pressure in the LIGO gravitational-wave detector," Appl. Opt., vol. 49, p. 3474, June 2010.

[25] K. L. Dooley and et al., "Angular control of optical cavities in a radiation-pressure-dominated regime: the Enhanced LIGO case," *Journal of the Optical Society of America A*, vol. 30, p. 2618, Dec. 2013.

[26] https://alog.ligo-wa.caltech.edu/aLOG/index.php?callRep=26367.

[27] https://alog.ligo-la.caltech.edu/aLOG/index.php?callRep=37576.

[28] S. M. Aston and et al., "Update on quadruple suspension design for Advanced LIGO," *Classical and Quantum Gravity*, vol. 29, p. 235004, Dec. 2012.

[29] `https://alog.ligo-la.caltech.edu/aLOG/index.php?callRep=41815`.

[30] `https://alog.ligo-wa.caltech.edu/aLOG/index.php?callRep=45750`.

[31] `https://alog.ligo-la.caltech.edu/aLOG/index.php?callRep=41855`.

[32] `https://alog.ligo-wa.caltech.edu/aLOG/index.php?callRep=46469`.

[33] P. Fulda and D. Brown, *AS36 WFS simulations for H1*. LIGO, 2015. LIGO Document G1501251-v1.

[34] H. Yamamoto, *Study of the point absorption on ITMX at LHO*. LIGO, 2017. LIGO Document G1700588-v3.

[35] H. Yu and D. Sigg, *Alignment sensing in the signal recycling cavity using a new 118.3 MHz sideband scheme*. LIGO, 2017. LIGO Document T1700215-v3.

[36] `https://alog.ligo-la.caltech.edu/aLOG/index.php?callRep=41784`.

[37] A. Buonanno and Y. Chen, "Signal recycled laser-interferometer gravitational-wave detectors as optical springs," Phys. Rev. D, vol. 65, p. 042001, Feb 2002.

[38] C. Cahillane and et al., "Calibration uncertainty for Advanced LIGO's first and second observing runs," Phys. Rev. D, vol. 96, p. 102001, Nov 2017.

[39] H. Yu, *SRC detuning induced by differential ITM thermal lens*. LIGO, 2017. LIGO Document T1700246-v2.

[40] B. P. Abbott and et al., "Binary Black Hole Mergers in the First Advanced LIGO Observing Run," *Physical Review X*, vol. 6, p. 041015, Oct. 2016.

[41] The LIGO Scientific Collaboration and the Virgo Collaboration, "GWTC-1: A Gravitational-Wave Transient Catalog of Compact Binary Mergers Observed by LIGO and Virgo during the First and Second Observing Runs," *arXiv e-prints*, p. arXiv:1811.12907, Nov 2018.

[42] LIGO Scientific Collaboration and et al., "Advanced LIGO," *Classical and Quantum Gravity*, vol. 32, p. 074001, Apr. 2015.

[43] F. Acernese and et al., "Advanced Virgo: a second-generation interferometric gravitational wave detector," *Classical and Quantum Gravity*, vol. 32, p. 024001, Jan. 2015.

[44] M. Coleman Miller and E. J. M. Colbert, "Intermediate-Mass Black Holes," *International Journal of Modern Physics D*, vol. 13, pp. 1–64, 2004.

[45] I. Mandel, D. A. Brown, J. R. Gair, and M. C. Miller, "Rates and Characteristics of Intermediate Mass Ratio Inspirals Detectable by Advanced LIGO," ApJ, vol. 681, pp. 1431–1447, July 2008.

[46] P. B. Graff, A. Buonanno, and B. S. Sathyaprakash, "Missing Link: Bayesian detection and measurement of intermediate-mass black-hole binaries," Phys. Rev. D, vol. 92, p. 022002, July 2015.

[47] J. Veitch, M. Pürrer, and I. Mandel, "Measuring Intermediate-Mass Black-Hole Binaries with Advanced Gravitational Wave Detectors," *Physical Review Letters*, vol. 115, p. 141101, Oct. 2015.

[48] C.-J. Haster, Z. Wang, C. P. L. Berry, S. Stevenson, J. Veitch, and I. Mandel, "Inference on gravitational waves from coalescences of stellar-mass compact objects and intermediate-mass black holes," *Mon. Not. R. Astron Soc.*, vol. 457, pp. 4499–4506, Apr. 2016.

[49] B. P. Abbott and et al., "Search for intermediate mass black hole binaries in the first observing run of Advanced LIGO," Phys. Rev. D, vol. 96, p. 022001, July 2017.

[50] C. Cutler and É. E. Flanagan, "Gravitational waves from merging compact binaries: How accurately can one extract the binary's parameters from the inspiral waveform\?," Phys. Rev. D, vol. 49, pp. 2658–2697, Mar. 1994.

[51] B. P. Abbott and et al., "Gw170817: Observation of gravitational waves from a binary neutron star inspiral," *Phys. Rev. Lett.*, vol. 119, p. 161101, Oct 2017.

[52] B. P. Abbott and et al., "Multi-messenger Observations of a Binary Neutron Star Merger," *Astrophys. J. Lett.*, vol. 848, p. L12, Oct. 2017.

[53] A. Lazzarini, D. Reitze, B. Berger, L. Cadonati, G. Gonzalez, and M. Cavaglia, *What Comes Next for LIGO? Planning for the post-detection era in gravitational-wave detectors and astrophysics.* LIGO, 2016. LIGO Document P1600350.

[54] R. Adhikari and et al., *LIGO Voyager Upgrade Concept.* LIGO, 2017. LIGO Document T1400226.

[55] S. Hild, S. Chelkowski, A. Freise, J. Franc, N. Morgado, R. Flaminio, and R. DeSalvo, "A xylophone configuration for a third-generation gravitational wave detector," *Classical and Quantum Gravity*, vol. 27, p. 015003, Jan. 2010.

[56] B. Sathyaprakash and et al., "Scientific objectives of Einstein Telescope," *Classical and Quantum Gravity*, vol. 29, p. 124013, June 2012.

[57] B. P. Abbott and et al., "Exploring the sensitivity of next generation gravitational wave detectors," *Classical and Quantum Gravity*, vol. 34, p. 044001, Feb. 2017.

[58] D. V. Martynov, *Lock Acquisition and Sensitivity Analysis of Advanced LIGO Interferometers.* PhD thesis, California Institute of Technology, 2015.

[59] B. Lantz, R. Schofield, B. O. Reilly, D. E. Clark, and D. DeBra, "Review: Requirements for a ground rotation sensor to improve advanced ligo," *Bull. Seismol. Soc. Am.*, vol. 99, p. 980, 2009.

[60] F. Matichard and M. Evans, "Review: Tilt-Free Low-Noise Seismometry," *The Bulletin of the Seismological Society of America*, vol. 105, pp. 497–510, Apr. 2015.

[61] F. Matichard and et al., "Modeling and experiment of the suspended seismometer concept for attenuating the contribution of tilt motion in horizontal measurements," *Review of Scientific Instruments*, vol. 87, no. 6, p. 065002, 2016.

[62] K. Venkateswara, C. A. Hagedorn, M. D. Turner, T. Arp, and J. H. Gundlach, "A high-precision mechanical absolute-rotation sensor," *Rev. Sci. Instrum.*, vol. 85, p. 015005, 2014.

[63] K. Venkateswara and et al., "Subtracting tilt from a horizontal seismometer using a ground?rotation sensor," *Bulletin of the Seismological Society of America*, vol. 107, no. 2, p. 709, 2017.

[64] C. M. Mow-Lowry and D. Martynov, "A 6D interferometric inertial isolation system," *ArXiv e-prints*, Jan. 2018.

[65] A. V. Cumming and et al., "Design and development of the advanced LIGO monolithic fused silica suspension," *Classical and Quantum Gravity*, vol. 29, p. 035003, Feb. 2012.

[66] B. N. Shapiro, R. Adhikari, J. Driggers, J. Kissel, B. Lantz, J. Rollins, and K. Youcef-Toumi, "Noise and control decoupling of advanced ligo suspensions," *Classical and Quantum Gravity*, vol. 32, no. 1, p. 015004, 2015.

[67] S. Aston, *Optical Read-out Techniques for the Control of Test-masses in Gravitational Wave Observatories.* PhD thesis, University of Birmingham, 2011.

[68] S. Hild and et al., *LIGO 3 Strawman Design, Team Red.* LIGO, 2012. LIGO Document T1200046.

[69] A. Buonanno and Y. Chen, "Quantum noise in second generation, signal-recycled laser interferometric gravitational-wave detectors," *Phys. Rev. D*, vol. 64, p. 042006, Jul 2001.

[70] H. Miao, *Exploring Macroscopic Quantum Mechanics in Optomechanical Devices.* Springer Theses, Springer Berlin Heidelberg, 2012.

[71] D. McClelland, N. Mavalvala, Y. Chen, and R. Schnabel, "Advanced interferometry, quantum optics and optomechanics in gravitational wave detectors," *Laser and Photonics Reviews*, vol. 5, no. 5, pp. 677–696, 2011.

[72] Ligo Scientific Collaboration, "A gravitational wave observatory operating beyond the quantum shot-noise limit," *Nature Physics*, vol. 7, pp. 962–965, Dec. 2011.

[73] J. Aasi and et al., "Enhanced sensitivity of the LIGO gravitational wave detector by using squeezed states of light," *Nature Photonics*, vol. 7, pp. 613–619, Aug. 2013.

[74] H. J. Kimble, Y. Levin, A. B. Matsko, K. S. Thorne, and S. P. Vyatchanin, "Conversion of conventional gravitational-wave interferometers into quantum nondemolition interferometers by modifying their input and/or output optics," *Phys. Rev. D*, vol. 65, p. 022002, Dec 2001.

[75] J. Harms, Y. Chen, S. Chelkowski, A. Franzen, H. Vahlbruch, K. Danzmann, and R. Schnabel, "Squeezed-input, optical-spring, signal-recycled gravitational-wave detectors," *Phys. Rev. D*, vol. 68, p. 042001, Aug 2003.

[76] P. Kwee, J. Miller, T. Isogai, L. Barsotti, and M. Evans, "Decoherence and degradation of squeezed states in quantum filter cavities," *Phys. Rev. D*, vol. 90, p. 062006, Sep 2014.

[77] E. Oelker, T. Isogai, J. Miller, M. Tse, L. Barsotti, N. Mavalvala, and M. Evans, "Audio-Band Frequency-Dependent Squeezing for Gravitational-Wave Detectors," *Physical Review Letters*, vol. 116, p. 041102, Jan. 2016.

[78] P. R. Saulson, "Thermal noise in mechanical experiments," *Phys. Rev. D*, vol. 42, pp. 2437–2445, Oct 1990.

[79] G. González, "Suspensions thermal noise in the LIGO gravitational wave detector," *Classical and Quantum Gravity*, vol. 17, pp. 4409–4435, Nov. 2000.

[80] Y. Levin, "Internal thermal noise in the LIGO test masses: A direct approach," Phys. Rev. D, vol. 57, pp. 659–663, Jan. 1998.

[81] T. Hong, H. Yang, E. K. Gustafson, R. X. Adhikari, and Y. Chen, "Brownian thermal noise in multilayer coated mirrors," *Phys. Rev. D*, vol. 87, p. 082001, Apr 2013.

[82] W. Yam, S. Gras, and M. Evans, "Multimaterial coatings with reduced thermal noise," *Phys. Rev. D*, vol. 91, p. 042002, Feb 2015.

[83] S. Gras, H. Yu, W. Yam, D. Martynov, and M. Evans, "Audio-band coating thermal noise measurement for Advanced LIGO with a multimode optical resonator," Phys. Rev. D, vol. 95, p. 022001, Jan. 2017.

[84] W. C. Young and R. G. Budynas, *Roark's formulas for stress and strain*, vol. 7. McGraw-Hill New York, 2002.

[85] G. D. Hammond, A. V. Cumming, J. Hough, R. Kumar, K. Tokmakov, S. Reid, and S. Rowan, "Reducing the suspension thermal noise of advanced gravitational wave detectors," *Classical and Quantum Gravity*, vol. 29, p. 124009, June 2012.

[86] V. Mitrofanov and K. Tokmakov, "Effect of heating on dissipation of mechanical energy in fused silica fibers," *Physics Letters A*, vol. 308, no. 2, pp. 212 – 218, 2003.

[87] J. Steinlechner and et al., "Optical absorption of ion-beam sputtered amorphous silicon coatings," *Phys. Rev. D*, vol. 93, p. 062005, Mar 2016.

[88] P. R. Saulson, "Terrestrial gravitational noise on a gravitational wave antenna," *Phys. Rev. D*, vol. 30, pp. 732–736, Aug 1984.

[89] S. A. Hughes and K. S. Thorne, "Seismic gravity-gradient noise in interferometric gravitational-wave detectors," Phys. Rev. D, vol. 58, p. 122002, Dec. 1998.

[90] J. C. Driggers, J. Harms, and R. X. Adhikari, "Subtraction of newtonian noise using optimized sensor arrays," *Phys. Rev. D*, vol. 86, p. 102001, Nov 2012.

[91] T. Creighton, "Tumbleweeds and airborne gravitational noise sources for LIGO," *Classical and Quantum Gravity*, vol. 25, p. 125011, June 2008.

[92] J. Harms, "Terrestrial Gravity Fluctuations," *Living Reviews in Relativity*, vol. 18, p. 3, Dec. 2015.

[93] M. Coughlin, N. Mukund, J. Harms, J. Driggers, R. Adhikari, and S. Mitra, "Towards a first design of a Newtonian-noise cancellation system for Advanced LIGO," *Classical and Quantum Gravity*, vol. 33, p. 244001, Dec. 2016.

[94] E. Flanagan and K. Thorne, *Noise Due to Backscatter Off Baffles, the Nearby Wall, and Objects at the Fare End of the Beam Tube; and Recommended Actions*. LIGO, 1994. LIGO Document T940063-x0.

[95] D. J. Ottaway, P. Fritschel, and S. J. Waldman, "Impact of upconverted scattered light on advanced interferometric gravitational wave detectors," *Opt. Express*, vol. 20, pp. 8329–8336, Apr 2012.

[96] B. Canuel, E. Genin, G. Vajente, and J. Marque, "Displacement noise from back scattering and specular reflection of input optics in advanced gravitational wave detectors," *Opt. Express*, vol. 21, pp. 10546–10562, May 2013.

[97] B. Allen, "The Stochastic Gravity-Wave Background: Sources and Detection," in *Relativistic Gravitation and Gravitational Radiation* (J.-A. Marck and J.-P. Lasota, eds.), (Cambridge, UK), p. 373, Cambridge University Press, 1997.

[98] M. Bejger, "Status of the continuous gravitational wave searches in the Advanced Detector Era," *ArXiv e-prints*, Oct. 2017.

[99] H.-Y. Chen, D. E. Holz, J. Miller, M. Evans, S. Vitale, and J. Creighton, "Distance measures in gravitational-wave astrophysics and cosmology," *ArXiv e-prints*, Sept. 2017.

[100] A. Sesana, J. Gair, I. Mandel, and A. Vecchio, "Observing Gravitational Waves from the First Generation of Black Holes," *Astrophys. J. Lett.*, vol. 698, pp. L129–L132, June 2009.

[101] E. D. Kovetz, "Probing primordial black hole dark matter with gravitational waves," *Phys. Rev. Lett.*, vol. 119, p. 131301, Sep 2017.

[102] Planck Collaboration, "Planck 2015 results. XIII. Cosmological parameters," *Astronomy and Astrophysics*, vol. 594, p. A13, Sept. 2016.

[103] B. Abbott and et al., "Astrophysical Implications of the Binary Black-hole Merger GW150914," *Astrophys. J. Lett.*, vol. 818, p. L22, Feb. 2016.

[104] S. Bird, I. Cholis, J. B. Muñoz, Y. Ali-Haïmoud, M. Kamionkowski, E. D. Kovetz, A. Raccanelli, and A. G. Riess, "Did ligo detect dark matter?," *Phys. Rev. Lett.*, vol. 116, p. 201301, May 2016.

[105] M. Hannam, P. Schmidt, A. Bohé, L. Haegel, S. Husa, F. Ohme, G. Pratten, and M. Pürrer, "Simple model of complete precessing black-hole-binary gravitational waveforms," *Phys. Rev. Lett.*, vol. 113, p. 151101, Oct 2014.

[106] P. Ajith and et al., "Inspiral-merger-ringdown waveforms for black-hole binaries with nonprecessing spins," *Phys. Rev. Lett.*, vol. 106, p. 241101, Jun 2011.

[107] L. Santamaría and et al., "Matching post-Newtonian and numerical relativity waveforms: Systematic errors and a new phenomenological model for nonprecessing black hole binaries," Phys. Rev. D, vol. 82, p. 064016, Sept. 2010.

[108] P. Schmidt, F. Ohme, and M. Hannam, "Towards models of gravitational waveforms from generic binaries: II. Modelling precession effects with a single effective precession parameter," Phys. Rev. D, vol. 91, p. 024043, Jan. 2015.

[109] K. Somiya, "Detector configuration of KAGRA-the Japanese cryogenic gravitational-wave detector," *Classical and Quantum Gravity*, vol. 29, p. 124007, June 2012.

[110] J. Veitch and et al., "Parameter estimation for compact binaries with ground-based gravitational-wave observations using the LALInference software library," Phys. Rev. D, vol. 91, p. 042003, Feb. 2015.

[111] K. K. Y. Ng, S. Vitale, A. Zimmerman, K. Chatziioannou, D. Gerosa, and C.-J. Haster, "Gravitational-wave astrophysics with effective-spin measurements: Asymmetries and selection biases," Phys. Rev. D, vol. 98, p. 083007, Oct 2018.

[112] C. L. Rodriguez, M. Zevin, C. Pankow, V. Kalogera, and F. A. Rasio, "Illuminating Black Hole Binary Formation Channels with Spins in Advanced LIGO," *Astrophys. J. Lett.*, vol. 832, p. L2, Nov. 2016.

[113] B. Farr, D. E. Holz, and W. M. Farr, "Using Spin to Understand the Formation of LIGO and Virgo's Black Holes," *Astrophys. J. Lett.*, vol. 854, p. L9, Feb. 2018.

[114] P. Jaranowski, A. Królak, and B. F. Schutz, "Data analysis of gravitational-wave signals from spinning neutron stars: The signal and its detection," *Phys. Rev. D*, vol. 58, p. 063001, Aug 1998.

[115] S. Vitale and M. Evans, "Parameter estimation for binary black holes with networks of third-generation gravitational-wave detectors," Phys. Rev. D, vol. 95, p. 064052, Mar. 2017.

[116] W. Zhao and L. Wen, "Localization accuracy of compact binary coalescences detected by the third-generation gravitational-wave detectors and implication for cosmology," *ArXiv e-prints*, Oct. 2017.

[117] L. Wen and Y. Chen, "Geometrical expression for the angular resolution of a network of gravitational-wave detectors," Phys. Rev. D, vol. 81, p. 082001, Apr. 2010.

[118] M. Burgay and et al., "An increased estimate of the merger rate of double neutron stars from observations of a highly relativistic system," Nature, vol. 426, pp. 531–533, Dec. 2003.

[119] D. Lai, "Resonant Oscillations and Tidal Heating in Coalescing Binary Neutron Stars," *Mon. Not. R. Astron Soc.*, vol. 270, p. 611, Oct. 1994.

[120] A. Reisenegger and P. Goldreich, "Excitation of neutron star normal modes during binary inspiral," *Astrophys. J.*, vol. 426, pp. 688–691, May 1994.

[121] É. É. Flanagan and É. Racine, "Gravitomagnetic resonant excitation of Rossby modes in coalescing neutron star binaries," Phys. Rev. D, vol. 75, p. 044001, Feb. 2007.

[122] H. Yu and N. N. Weinberg, "Dynamical tides in coalescing superfluid neutron star binaries with hyperon cores and their detectability with third-generation gravitational-wave detectors," *Mon. Not. R. Astron Soc.*, vol. 470, pp. 350–360, Sept. 2017.

[123] T. Hinderer, B. D. Lackey, R. N. Lang, and J. S. Read, "Tidal deformability of neutron stars with realistic equations of state and their gravitational wave signatures in binary inspiral," *Phys. Rev. D*, vol. 81, p. 123016, Jun 2010.

[124] Douchin, F. and Haensel, P., "A unified equation of state of dense matter and neutron star structure," *Astron. Astrophys.*, vol. 380, no. 1, pp. 151–167, 2001.

[125] H. Yu and N. N. Weinberg, "Resonant tidal excitation of superfluid neutron stars in coalescing binaries," MNRAS, vol. 464, pp. 2622–2637, Jan. 2017.

[126] N. Andersson and W. C. G. Ho, "Using gravitational-wave data to constrain dynamical tides in neutron star binaries," Phys. Rev. D, vol. 97, p. 023016, Jan. 2018.

[127] D. Christodoulou, "Nonlinear nature of gravitation and gravitational-wave experiments," *Phys. Rev. Lett.*, vol. 67, pp. 1486–1489, Sep 1991.

[128] M. Favata, "Nonlinear Gravitational-Wave Memory from Binary Black Hole Mergers," *Astrophys. J. Lett.*, vol. 696, pp. L159–L162, May 2009.

[129] E. Berti, V. Cardoso, and M. Casals, "Eigenvalues and eigenfunctions of spin-weighted spheroidal harmonics in four and higher dimensions," Phys. Rev. D, vol. 73, p. 024013, Jan. 2006.

[130] P. D. Lasky, E. Thrane, Y. Levin, J. Blackman, and Y. Chen, "Detecting Gravitational-Wave Memory with LIGO: Implications of GW150914," *Physical Review Letters*, vol. 117, p. 061102, Aug. 2016.

[131] B. P. Abbott and et al., "Observation of Gravitational Waves from a Binary Black Hole Merger," *Physical Review Letters*, vol. 116, p. 061102, Feb. 2016.

[132] P. Fritschel, D. Shoemaker, and D. Coyne, *Low-frequency Cutoff for Advanced LIGO.* LIGO, 2002. LIGO Document T020034.

[133] `https://alog.ligo-la.caltech.edu/aLOG/index.php?callRep=29665`.